uOttawa

L'Université canadienne
Canada's university

FACULTÉ DES ÉTUDES SUPÉRIEURES ET POSTOCTORALES

uOttawa

L'Université canadienne
Canada's university

FACULTY OF GRADUATE AND POSDOCTORAL STUDIES

Wenhao Zhu
AUTEUR DE LA THÈSE / AUTHOR OF THESIS

Ph.D. (Electrical Engineering)
GRADE / DEGREE

School of Information Technology and Engineering
FACULTÉ, ÉCOLE, DÉPARTEMENT / FACULTY, SCHOOL, DEPARTMENT

Artificial Microwave Volume Holograms Based on Printed Dielectrics : Theory, Performance Analysis & Potential Application in Antenna Systems

TITRE DE LA THÈSE / TITLE OF THESIS

Derek McNamara
DIRECTEUR (DIRECTRICE) DE LA THÈSE / THESIS SUPERVISOR

CO-DIRECTEUR (CO-DIRECTRICE) DE LA THÈSE / THESIS CO-SUPERVISOR

EXAMINATEURS (EXAMINATRICES) DE LA THÈSE / THESIS EXAMINERS

Emad Gad

Aldo Petosa

Michael Potter

Mustapha Yagoub

Gary W. Slater
LE DOYEN DE LA FACULTÉ DES ÉTUDES SUPÉRIEURES ET POSTDOCTORALES /
DEAN OF THE FACULTY OF GRADUATE AND POSTDOCORAL STUDIES

Artificial Microwave Volume Holograms Based on Printed Dielectrics: Theory, Performance Analysis & Potential Application in Antenna Systems

by

Wenhao Zhu

A thesis submitted to the Faculty of Graduate and Postdoctoral studies
in partial fulfillment of the requirements for the degree of
Doctor of Philosophy

Ottawa-Carleton Institute for Electrical and Computer Engineering
School of Information Technology and Engineering
University of Ottawa

Your file Votre référence
ISBN: 978-0-494-15154-9
Our file Notre référence
ISBN: 978-0-494-15154-9

Artificial Microwave Volume Holograms Based on Printed Dielectrics: Theory, Performance Analysis & Potential Application in Antenna Systems

Wenhao Zhu

School of Information Technology and Engineering
University of Ottawa
Degree of Doctor of Philosophy
2005

Abstract

A new type of complex electromagnetic structure, the artificial microwave volume hologram (AMVH), has been studied systematically. The structure consists of cascaded planar lattices of metallic circular patches with varying size and can be designed to have an effective dielectric modulation that follows a holographic interference pattern. Under the illumination of certain electromagnetic waves, an AMVH can reproduce a required wave field pattern based on its design, just like a traditional volume hologram in optical holography. A theoretical model, namely the self-consistent dynamic-dipole interaction theory (DDIT), has been developed to characterize AMVHs for wave scattering and beam form conversion. It can also be used for designing AMVHs as well as for optimization. Multiplex AMVHs have been proposed and simulated, in which more than two wave beams interact with the structure, which results in wave beam conversion, splitting or combining. Their flexibility and application potential are illustrated through a number of examples such as multi-beam antennas, shared apertures, and beam splitting and combining. Experimental validation of the theory has been carried out on several fabricated AMVHs, which has confirmed the theory. An alternative patch geometry, namely a square patch, has been proposed and analyzed for application in AMVHs, which can provide significant higher electric polarizability. Finally, a full-wave FEM simulation has been done to verify the accuracy of the theoretical model.

Acknowledgements

First, I would like to thank my thesis advisor Dr. Derek McNamara for his academic advice and guidance, insights, and financial support. He has always been accessible and helpful.

I would also like to thank Mr. Michel Cuhaci, the manager of Advanced Antenna Technology, at the Communications Research Center (CRC) for providing me the opportunity to collaborate with the CRC on my thesis project.

My special thanks goes to Dr. Jafar Shaker from the Communications Research Center for suggesting this topic, and his advice and help during the course of my thesis research. Also my thanks to Dr. Apisak Ittipiboon from the Communications Research Center for advice and discussions.

I would also like to express my gratitude to my thesis committee, Dr. Mustapha Yagoub (University of Ottawa), and Dr. Aldo Petosa (Carleton University) for their time and valuable suggestions.

I'm also thankful to many graduate students in the RF & Microwave Lab at the University of Ottawa, in particular to Paul Salem, Igor Acimovic & Tan Quach for their help with the simulation software.

I also wish to acknowledge the Ontario Graduate Scholarship (OGS) and the University of Ottawa for their financial support during my Ph.D. work.

Finally, I am indebted to my family, my wife, Xue, for her endless support and care, and my two sons, Eric and David, for their understanding.

TABLE OF CONTENTS

List of Figures

List of Tables

List of Symbols

$\boldsymbol{A}$	magnetic vector potential
a	lattice constant in x-direction
b	lattice constant in y-direction
c	lattice constant in z-direction
d	diameter of a disk patch or width of a square patch
D	electric displacement at a given direction
$\boldsymbol{E}$	electric field vector
$E^{y,e}, E^{x,e}$	y-, x-component of electric field caused by electric dipoles
$E^{y,m}, E^{x,m}$	y-, x-component of electric field caused by magnetic dipoles
$E^{y,tot}, E^{x,tot}$	y-, x-component of total electric field
E_i^y, E_i^x	y-, x-component of incident electric field
E_0	magnitude of incident electric field
E^{ap}	external applied electric field at a given direction
E^{eff}	effective electric field at a given direction
E^i	interaction electric field at a given direction
E_o	electric field of object beam at a given direction
E_r	electric field of reference beam at a given direction
f	frequency
$f_i()$	ith mode function in coupled-wave theory
$\boldsymbol{H}$	magnetic field vector
$H^{z,e}, H^{x,e}$	z-, x-component of magnetic field caused by electric dipoles
$H^{z,m}, H^{x,m}$	z-, x-component of magnetic field caused by magnetic dipoles
$H^{z,tot}, H^{x,tot}$	z-, x-component of total magnetic field
H_i^z, H_i^x	z-, x-component of incident magnetic field
H_0	magnitude of incident magnetic field
i	patch index in x-direction

j	unit imaginary number
k	wave number
k_x	wave number in x-direction
k_z	wave number in z-direction
$\boldsymbol{k}$	propagation vector
$K_0()$	modified Bessel function of second kind
m_i	induced magnetic dipole on ith patch
M	total magnetic dipole moment per unit volume
m	mode order
n	patch index in z-direction
N	number of total planar lattice layers
p_i	induced electric dipole on ith patch
P	total electric dipole moment per unit volume
r	spatial distance
R	reflection coefficient
S_{ik}	components of S-Matrix
t	total thickness of hologram slab
T	transmission coefficient
u_m	wave number in x-direction of the mth space harmonic
v_m	wave number in z-direction of the mth space harmonic
V	potential
x	rectangular coordinate
y	rectangular coordinate
z	rectangular coordinate
$\hat{\boldsymbol{x}}$	unit vector of rectangular coordinate
$\hat{\boldsymbol{y}}$	unit vector of rectangular coordinate
$\hat{\boldsymbol{z}}$	unit vector of rectangular coordinate
Z	normalized wave impedance
α_e	electric polarizability
α_m	magnetic polarizability
δ	displacement in x-direction between successive planar lattices

δ_{ik} Kronecker symbol

$\delta()$ unit impulse function

Δ_e element area

ε_0 permittivity of free-space

ε_H dielectric constant of host dielectric medium

ε_r^{eff} effective dielectric constant or effective relative permittivity

ε_a average dielectric constant

ε_d magnitude of dielectric constant modulation

γ Euler's constant, 0.577

η characteristic impedance of host dielectric medium

φ angle of recording beams with respect to the normal

λ wavelength

Λ spatial period of dielectric modulation

μ permeability

Π Hertzian vector potential

θ_i angle of incidence

ρ charge density

ω angular frequency

Ω conducting patch area

ξ, η transformed coordinates

Chapter 1

Introduction

1.1 Motivation

Optical holography was first demonstrated by Gabor [1] in 1948. It was shown that with a coherent reference wave, both the amplitude and phase of a scattered (diffracted) light wave can be recorded and then its wavefront can be reconstructed, despite the fact that recording media respond only to the light intensity. During the 1960's, optical holography obtained tremendous improvements in both the concept and technology, and generated a great impact in optical engineering [2], especially in the imaging process area.

The success of optical holography stimulated the studies of applying the holography concept to the microwave regime. In the 1970's, the holographic antenna concept was proposed [3-5], in which the binary holographic pattern was formed artificially by using a printed microstrip board and the horn-fed surface wave (served as the reference beam) is diffracted by the strip pattern to yield the broadside radiation (the reproduced object beam). Except for its low profile feature, this type of antenna received little interest in its early days due to its low power and efficiency. Recently, a new interest in this type of antenna has been rekindled by the fact that it has the potential of being reconfigurable [6,7] with micro-fabrication technique. Other applications, including visualization of radiation pattern [8], non-destructive testing [9], far-field to near-field conversion [10], etc, were also explored in the period and the following years. However, the application of holography concept has been quite limited so far in the microwave and antenna area, because of the lack of recording media that can work in microwave frequency band.

On the other hand, computer generation of holograms [11] provides another way of obtaining the holograms of complex objects without actually involving the physical recording process. Though this technique is only suitable for producing thin holograms on transparencies, it does deliver a hint that to achieve microwave holograms one may not have

to rely on the microwave counterpart of the optical recording media, like emulsions. In fact, for volume or thick holograms, what is essential is the interference patterns or refractive index gratings, which, in optics, are physically formed inside the emulsions by the interference fields of object and reference waves. While in microwave regime, the respective dielectric gratings can be, at least, calculated from the given object and reference waves, and then the question becomes can we realize the required dielectric distributions in a physical material? A recent preliminary study [12] has shown experimentally that by use of the printed artificial dielectric technique it is possible to implement a microwave volume hologram with a simple permittivity modulation. To give a complete, positive answer to the question, as well as to such follow-up questions as how efficient and what the performance of this type of holograms will be, what we can do with this technique for microwave and antenna applications, etc, a systematic research on this topic is essentially necessary. It should be noted that such a procedure of implementing microwave holograms would not apply to the situations where the object waves are unknown (e.g., detection problems). Nevertheless, in many microwave applications, particularly in antenna applications, the reference and object waves are usually known (e.g., the given input wave and the desired output wave of a lens antenna).

This thesis will carry out, as the first time, a systematic study on artificial microwave volume holograms (AMVHs) implemented using the printed circuit board (PCB) technique. It will include both the theoretical and experimental investigations, and will address the performance and design optimization issues. It will also explore different hologram structures and their potential applications in antenna systems.

1.2 Outline of the thesis

This thesis treats a new type of artificial complex material, i.e., microwave volume holograms. The thesis is organized in ten chapters, and the outline of each chapter is presented here.

- Chapter 2 briefly reviews the technologies of artificial dielectrics, frequency selective surfaces, reflectarrays, and electromagnetic band-gap structures. Their relation to

microwave volume holograms is addressed. The advantages of microwave volume holograms over the existing techniques are also discussed.

- Chapter 3 presents the theoretical model for AMVHs, i.e. the self-consistent dynamic-dipole-interaction theory. The theory directly works on the disk lattice array without involving the effective continuous medium model, and predicts the scattered fields including transmitted and reflected waves. Both TE and TM incidence are considered.

- Chapter 4 describes a theoretical model (static-dipole-interaction) for calculating the effective permittivity modulation for AMVHs. Based on the calculated effective continuous medium model, the rigorous coupled-wave-theory is used to analyze the scattering characteristics of the equivalent continuous hologram and to verify the theory presented in Chap.3.

- Chapter 5 carries out a parametric study to examine the effects of the lattice constants (c/a, b/a, number of layers, etc) on AMVHs' properties. The application potential of single-grating AMVHs is also addressed. As opposed to circular disks, a new patch shape, namely a square patch, is proposed to increase the dielectric modulation strength without adding more layers.

- Chapter 6 considers the multiplex volume holograms and their analysis with the theory described in Chapter 3. This corresponds to multiple wave (more than two) interference at the recording step. Application of multiplex holograms for beam splitting and combining is studied systematically.

- Chapter 7 describes the fabrication and experimental procedure for AMVHs. Measured results on several single and multiplex holograms are presented, and comparisons are made with the predicted results.

- Chapter 8 extends the theory described in Chapter 3 to include the effects of air-dielectric interfaces for AMVHs made in finite-thickness dielectric slabs. The classical wave matrix method is generalized to handle the multi-mode propagations in AMVH structures.

- Chapter 9 carries out a 3D FEM simulation of some simplified AMVHs using a commercial code (HFSS) to verify the self-consistent dynamic-dipole interaction theory.

The basic assumption (small-obstacle) is examined and quantified as a guideline for using the theory.

- Chapter 10 gives a summary and suggestions for future research.
- Appendices present the mathematical details used in the thesis

1.3 Original contributions

A number of problems associated with the development of the artificial microwave volume hologram (AMVH) technique, using cascaded sheets of conducting patches of varying size, have been dealt with. These involve various aspects of AMVHs including the static and dynamic electromagnetic field analysis, different polarizations, holograms with slanted and multiple holographic gratings, design procedures and optimizations. Some existing design procedures have been reinforced. The original contributions which have been presented in this thesis are:

1. The development of a systematic theory of AMVHs consisting of cascaded sheets of conducting patches of varying size, i.e. the self-consistent dynamic-dipole-interaction theory. This method models the discs or patches, which are electrically small, as time-harmonic electric and magnetic equivalent dipoles. The theory can be used to predict the reproduced wave fields under given input (read-out) waves and the related efficiencies and to analyze the general scattering characteristics of AMVHs. It also provides a powerful tool for parameter optimization of microwave holograms. The self-consistency arises from the fact that the moments of the equivalent dipoles are not prescribed but are determined from their interaction field together with the applied field, and the constitutional relation.
2. Experimental validation of the self-consistent dynamic-dipole-interaction theory. The predicted behavior and performance of AMVHs using the theory are compared with those from measurements performed on several fabricated AMVHs. A procedure of measuring each individual mode instead of total field is presented.
3. Multiplex AMVHs are proposed, analyzed, and designed to achieve more complex functions such as (i) spatial beam splitting and combining, (ii) multi-beam antennas,

and (iii) shared apertures. Multiplex AMVHs are obtained by integrating more than one holographic grating in one dielectric slab.

4. In contrast to the previous works on artificial dielectrics, it is found that AMVHs can be best realized by using square patches instead of circular disk patches. This new patch shape results in a higher equivalent electric dipole moment than circular patch does, and therefore can reduce the number of printed PCB layers needed to form the AMVHs.

5. AMVH design is done by determining the form of continuous permittivity modulation and by properly quantizing this modulation. The rigorous coupled-wave theory has been applied to validate such designs on the continuous medium models, and the results are compared with those from the dynamic dipole-interaction-theory analysis on the actual AMVHs. Good agreements have been obtained for the presented designs.

6. Since in the real world, AMVHs can only be made in finite-thickness dielectric slabs, a generalized wave matrix method has been derived to analyze finite-slab AMVHs. The effect of air-dielectric interfaces can be predicted quantitatively using the method, and the results are validated by the previous study as well as the measurements.

7. Finite element analysis has been used to validate the analysis method for a few sheets of conducting disk lattice of constant size (i.e. without spatial modulation of the disc size). This has also been used to determine the range of disk sizes for which the equivalent dipole model is valid. It is not feasible to use such a numerical technique to analyze a complete volume hologram.

In addition, a number of results, which could not be located in the open literature, have been presented. These include: (i) the role of the thickness of each printed PCB layer in AMVHs' performance; (2) the effects of high order (Bloch-Floquet) modes, their uses and suppression.

Chapter 2

Background and rationale

Nowadays, wireless communication is undergoing a rapid expansion worldwide in all the consumer, business, and national security and defense levels. The increasing demand for large capacities, fast data rates, and high quality services is leading to continuous development of new and advanced antenna technologies, including both devices and systems. The type of artificial microwave volume holograms (AMVHs) to be explored in this thesis work belongs to the passive components category in its nature and functions, more precisely, the part between antenna's feeds (EM wave sources) and radiated beams (free-space wave fields), as shown in Fig.2.1. The roles of AMVHs in antenna applications can be perceived from their optic counterparts. Presently, we are considering here the following potential applications.

(1) Beam routing. An AMVH can behave as a transparent slab to plane waves with incidence angle of any value but its Bragg angle. Near the Bragg angle the incident beam is re-routed to another direction based on how the AMVH designed. This angular-discrimination feature could be useful for angle-diversity antennas.

(2) Beam splitting and combining. With the superposition of multiple holographic gratings, an AMVH can split a single plane wave beam into several plane wave beams at different propagation directions, and *vice versa*. This feature can be used in spatial-power-combining antennas.

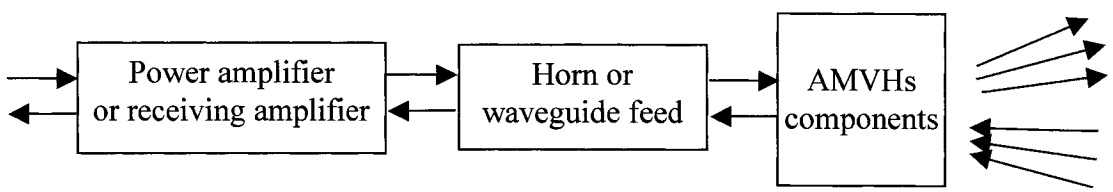

Fig.2.1 The position of AMVH components in antenna systems.

(3) Beam focusing and beam pattern shaping. With a proper design, an AMVH can act as a lens that causes incident plane waves focusing.

The microwave volume holograms considered are implemented based on the artificial dielectric technology. Because of small patch features, one can anticipate a very low resistive loss in AMVHs, which make them suitable for high frequency (millimeter wave) systems.

2.1 Artificial dielectrics (ADs)

The topic of artificial materials is a widespread research area that crosses many scientific and engineering regimes. As far as electrical engineering is concerned, artificial materials is about electromagnetic mixing of different composite media to create various "effective media" with novel and exclusive properties which natural materials do not posses [13]. Photonic band-gap materials (PBG) [14] and metamaterials with negative permeability and permittivity [15], for example, can be considered as artificial materials. Artificial dielectric (AD) is a subset of the general artificial materials, which consist of a large number of identical obstacles (inclusions) periodically distributed in a uniform host medium. A simple cubic lattice configuration is shown in Fig.2.2. These obstacles can be conductors (metals), or dielectrics (dissimilar to the host medium), or simply air/vacuum, and they play the role of modifying the dielectric property of the host media.

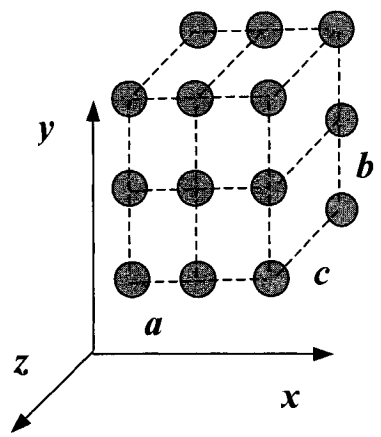

Fig.2.2 Artificial dielectric using cubic lattice configuration.

The concept originated from Kock's work [16] about metallic delay lens and then was studied by many researchers under the name "artificial dielectrics" [17-19]. It is based on the Lorentz theory, which considers the static dipole interaction of the obstacles [20]. When an external EM field is applied, each obstacle exhibits an electric dipole and a magnetic dipole, and the combined effects of all the obstacles in the lattice is to produce a net average dipole polarization field per unit volume, and thus a change in the effective permittivity. The formulism is given as below [20] (for simplicity, the magnetic dipole effect has been neglected)

$$\begin{aligned} D &= \varepsilon_0 \varepsilon_H E^{ap} + P = \varepsilon_0 \varepsilon_r^{eff} E^{ap}, \\ P &= Np = N\alpha_e \varepsilon_0 \varepsilon_H E^{eff}, \\ E^{eff} &= E^{ap} + E^{i} = E^{ap} + \frac{Cp}{\varepsilon_0 \varepsilon_H}, \end{aligned} \tag{2-1a,b,c}$$

where E^{ap}, E^{eff}, and E^{i} are the external applied, the effective, and the interaction electric fields, respectively, with the interaction field being produced by all the obstacles except the one under consideration in the infinite array, ε_H, the dielectric constant of the host medium, α_e the electric polarizability, p and P are the induced dipole on a single obstacle and the total moments per unit volume, respectively, $N=(abc)^{-1}$, the numbers of obstacles per unit volume, and C is called the interaction constant. The effective dielectric constant ε_r^{eff} can be readily found from the above relations

$$\begin{aligned} p &= \frac{\alpha_e \varepsilon_0 \varepsilon_H E^{ap}}{1 - \alpha_e C}, \\ \varepsilon_r^{eff} &= \varepsilon_H \left(1 + \frac{N\alpha_e}{1 - \alpha_e C}\right), \end{aligned} \tag{2-2a,b}$$

Since the Lorentz theory considers only static dipole interaction, the results will be valid only for obstacles whose sizes are small compared to their spacing, and both the sizes and spacing are small compared with the wavelength of interest. Therefore, artificial dielectrics are such periodic structures whose unit cells are electrically small and whose uses are only made of their constant average features. When thin flat conducting patches are used as obstacles, artificial dielectrics can be fabricated with the well-developed, low cost printed circuit board (PCB) technique in two steps. The first step is the fabrication of planar lattices

of conducting patches on natural dielectric layers, and then those layers are cascaded to form a 3D lattice structure, as shown in Fig.2.3. We may call such ADs printed artificial dielectrics (PADs).

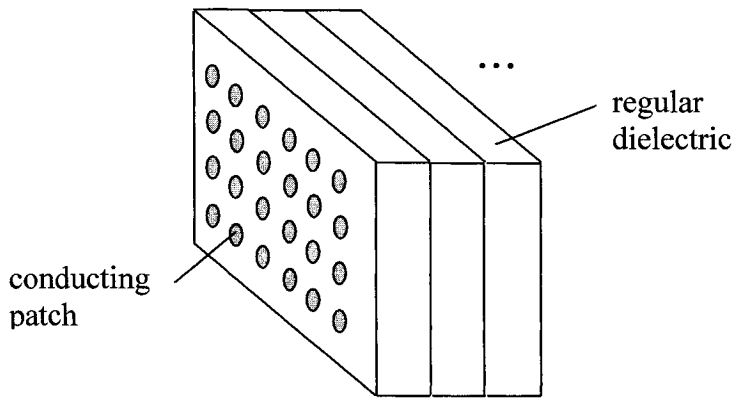

Fig.2.3 Printed artificial dielectric.

2.2 Artificial microwave volume holograms (AMVHs)

As mentioned above, normal artificial dielectrics contain identical obstacles, which result in a constant effective permittivity ε_r^{eff} in the structures. To achieve a distributed (spatial-varying) effective ε_r^{eff}, a natural way is to alter the sizes of obstacles following a certain rule. Although the choice of effective permittivity variation in a material can be arbitrary, depending on the specific application, the variations in ε_r^{eff} that follow some interference patterns of two or more wave beams will be of particular interest. This is because such variations in ε_r^{eff} actually represent the recorded interference patterns of multiple beams in microwave, and in this way many techniques used in optical holography can be carried over directly to the microwave regime. We call such an artificial dielectric with holographic modulation of effective permittivity an "artificial microwave volume hologram", or in short, "AMVH". By analogy to the beam reconstruction process in optical holography [21], illuminating an AMVH with one of its two recording beams will reproduce

the other recording beam. For example, consider a microwave volume hologram fabricated with following distributed effective permittivity

$$\varepsilon_r^{eff}(x) = \varepsilon_a + \varepsilon_1 \cos(\frac{2\pi}{\Lambda} x). \tag{2-3}$$

where Λ is the modulation period. This variation in ε_r^{eff} can be considered proportional to the intensity of the sum of the following two plane waves

$$E_o + E_r = e^{-j\pi(\xi z - x)/\Lambda} + e^{-j\pi(\xi z + x)/\Lambda}, \quad \therefore |E_o + E_r|^2 \propto 1 + \cos(\frac{2\pi}{\Lambda} x) \tag{2-4}$$

where ξ is determined from the given frequency. Then, if we use one of the two plane waves (say, E_r) as a read-out beam impinging on one side of the AMVH, the reconstructed wave (E_o, in this case) will emit from the other side of the AMVH (Fig.2.4). From the wave propagation point of view, this reconstructed beam corresponds to a diffraction wave, since it is not in the direction of the transmission (as it would happen with a homogeneous dielectric slab in place of the hologram). More sophisticated cases may be implemented following the same idea, and some of them will be discussed in the later chapters of this thesis.

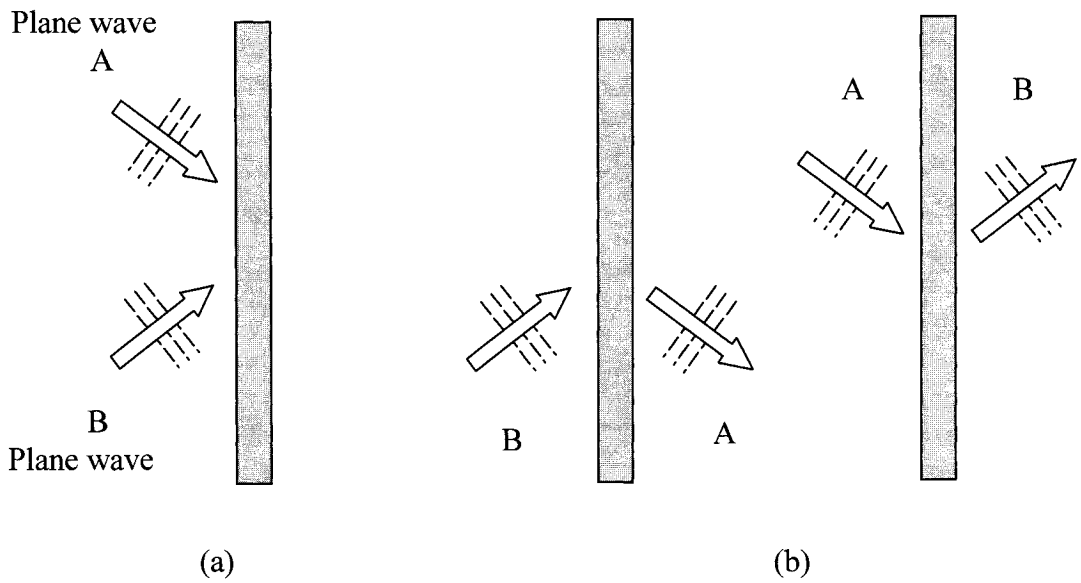

Fig.2.4 Recording and reproducing object beam.

For ADs with varying-size obstacles, the traditional static-dipole-interaction theory has to be modified and new relationships between spatial distributions of effective dielectrics and the modulations of obstacle sizes and shapes need to be established. In this thesis work, for ease of fabrication, only the PAD type of AMVHs is considered. A new formulism for calculating effective permittivity as a function of spatial coordinates will be derived for AMVHs with metallic discs of periodically varying size in one or two directions. Those effective permittivity functions represent the refractive index gratings of AMVHs and will be needed in analyzing the scattering process of the structures.

It should be noted that the optical holographic principles provide only qualitative guidelines as to how the microwave counterparts should be implemented. The actual performances of AMVHs thus designed and the scattered wave fields (transmitted/reflected) by the structures still remain unknown and need to be addressed. This is one of the major tasks this thesis work will try to achieve.

2.3 Relations with frequency selective surfaces (FSSs), reflectarrays, and electromagnetic band gap structures (EBGs)

Periodic structures have many applications in antenna and microwave engineering, in addition to ADs and AMVHs as mentioned above. Frequency selective surfaces (FSSs) are typical periodic structures that have been widely studied over decades [22-24]. Those structures consist of one or a number of cascaded planar periodic arrays of conducting patches or apertures on conducting surfaces. As the name manifests itself, FSSs act as EM wave frequency filters, and have been used in antenna systems as, e.g., subreflectors or part of Radome. In FSSs, the resonance of array elements determines the pass-band and stop-band features. In contrast, in AMVHs and ADs the elements are operated far away from resonance and the collective effect of the elements plays the dominant role. Therefore, FSS design is more concentrated in the representing element (shape and dimension), whereas AMVH design relies more on the element relations and the resulting effective behaviors of the structures.

Another important application of periodic structures is reflectarrays (or planar reflectors), which also comprise arrays of varying-size conducting patches [25-27]. Rigorously saying, reflectarrays are not periodic structures. But since conducting patches in reflectarrays are usually located at the nodes of planar lattices, which are indeed periodic structures, they are often treated as periodical structures. Reflectarray combine the advantages of reflectors and phased arrays, and perform wave front transforming or beam pattern shaping in the reflected fields (e.g. from plane wave to spherical wave or *vice versa*,) with the phase shifts generated by its varying-size patches. In comparison, AMVHs perform wave front transforming or beam pattern shaping in either transmitted or reflected fields, depending on how the holographic gratings be formed. Though both structures use varying-size patches, the former's elements operate around resonant condition, whereas, the latter's elements have much smaller dimensions compared to wavelength of interest, and the phase shifts required for wave front shaping is generated by the effective dielectric modulations. Finally, for FSSs and reflectarrays people usually deal with one beam, whereas in AMVHs multiple beams will be the standard feature.

Recently, significant research attention in microwave regime has focused on photonic and electromagnetic band-gap materials (PBG and EBG) [28-32]. EBGs are made of three-dimensional solids or structures, whose electromagnetic properties show periodicity in one, or two, or three dimensions. EM wave propagation inside EBGs will be limited in certain frequency bands (band-gap). As 2-D cases of general EBGs, periodic gratings had a long research history [33] well before the EBG concept emerged. A common foundation for periodic materials and structures, including ADs, AMVHs, FSSs, reflectarrays, and PBGs/EBGs, is the Floquet's theorem [34]. EM wave propagation and scattering in and from periodic structures can be expressed as Floquet modes. The main difference among these periodic structures lies in their relative element sizes, element spacing, and element modulation period with respect to the wavelength used. For example, increasing the element spacing up to more than half wavelength used will turn an AD structure into an EBG structure. Even though the patch spacing in AMVHs is much smaller than the wavelength used, the modulation period of its patch size is comparable to the wavelength, which gives this structure some EBGs' features such as stop-bands.

Chapter 3

Self-consistent dynamic-dipole-interaction theory of artificial microwave volume holograms (AMVHs)

3.1 Single hologram scheme and basic assumptions of the theory

An artificial microwave volume hologram (AMVH) representing a single holographic grating is shown in Fig.3.1a. It consists of N identical cascaded rectangular lattices of conducting patches embedded in an infinite host dielectric medium with dielectric constant of ε_H, each lattice's geometry and parameters are shown in Fig.3.1b. A typical and commonly used patch is circular disk of perfect conductor, which is considered first in this chapter. Other patch geometries will be treated in a later chapter. The disk size modulation along the x-direction is designed to simulate a modulated refractive index (dielectric) caused by an interference pattern of two recording plane waves being symmetrical about the normal of the hologram, as shown in Fig.3.1c. The modulation has a period Λ, which, for a given frequency, determines the incidence angle of the recording beams (often called "reference beam" and "object beam"), or *vice versa*. When the two recording beams are not symmetrical about the normal of the hologram, the formed interference pattern and therefore the resulting dielectric grating will be slanted at a certain angle with respect to the normal. This more general case will be treated at the end of this chapter.

The self-consistent dynamic-dipole-interaction theory (DDIT) developed is based on the following assumptions:

(1) the patch sizes are much smaller than the wavelength of interest;

(2) the patch spacing or the lattice constants a and b are much smaller than the wavelength of interest;

(3) the patch sizes are quite smaller compared to the patch spacing or the lattice constants a and b.

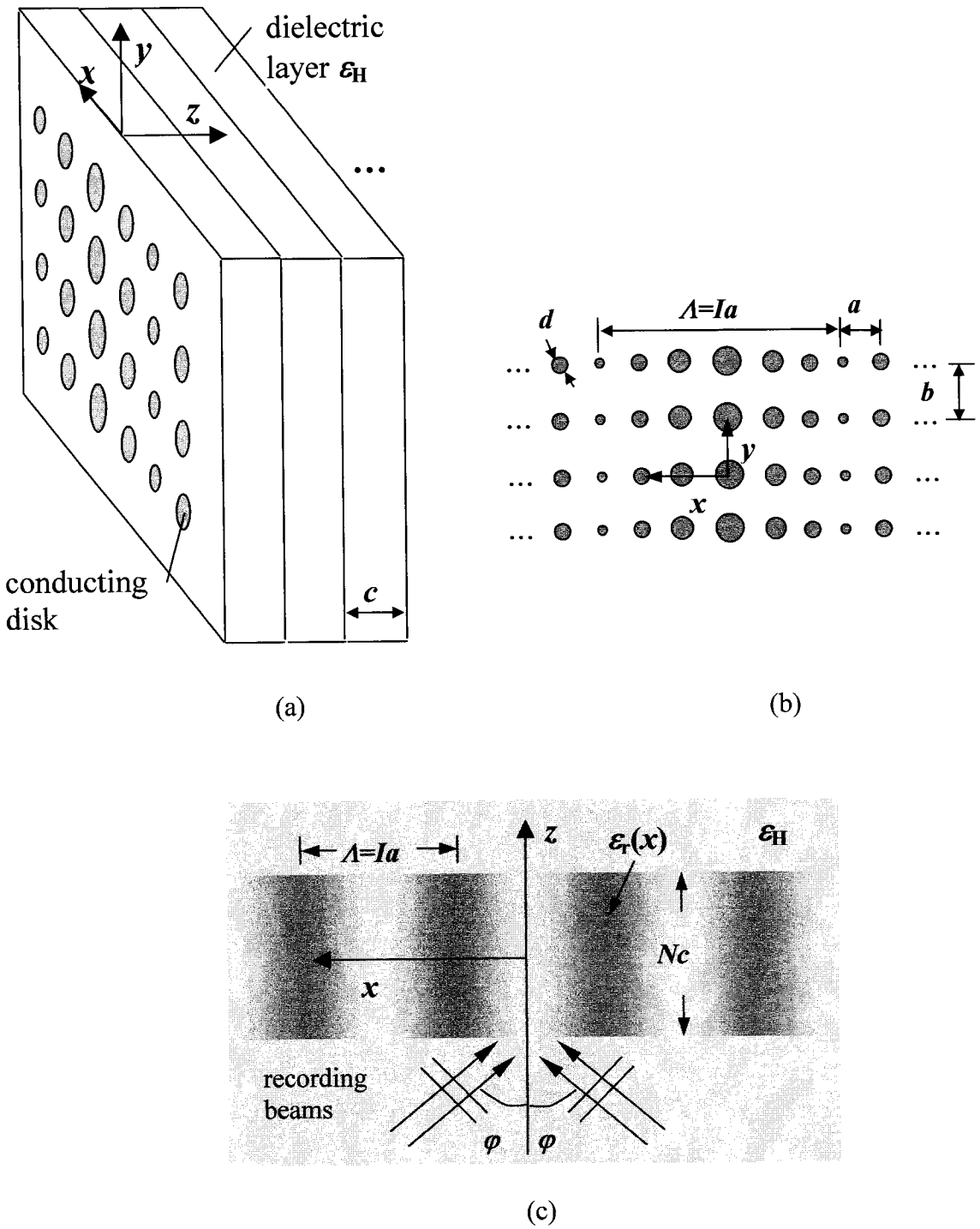

Fig. 3.1 (a) an artificial microwave volume hologram composed of finite layers of conducting disk lattices; (b) front view: the 2-D infinite planar conducting disk lattice with varying disk size (I is the number of patches in one period), (c) the equivalent continuous volume hologram formed by two symmetrical recording plane waves.

Depending on the forms of the applied external fields, the theory will be derived for the transverse electric wave incidence (TE) and the transverse magnetic wave incidence (TM), respectively. Also, to limit our focus to the main issue of the problem, i.e., the interaction of the 3D-arrayed conducting patches and applied fields, the ideal case with an infinite host dielectric medium instead of finite-thickness dielectric slab is considered here to exclude the air-dielectric interface effects. The case of finite-thickness hologram slabs will be addressed in chapter 8.

3.2 Transverse electric waves incidence (TE)

For TE excitation, the applied electric field is perpendicular to the plane of incidence, i.e. in the y-direction as shown in Fig.3.2. (It is also refereed to as perpendicular-polarization or E-polarization.) A TE plane wave with an incident angle of θ_i (Fig.3.2) has a form of

$$\begin{aligned} &E_i^y = E_0 e^{-j(k_x x + k_z z)},\ (H_i^x, H_i^z) = (-\cos\theta_i, \sin\theta_i) H_0 e^{-j(k_x x + k_z z)}, \\ &\text{with}\quad k_x = k\sin\theta_i,\ k_z = k\cos\theta_i,\ k^2 = \omega^2 \mu_0 \varepsilon_0 \varepsilon_{\mathrm{H}},\ H_0 = \eta^{-1} E_0. \end{aligned} \tag{3-1}$$

Here ε_{H}, k and η are the relative permittivity, propagation constant and characteristic impedance of the host medium, respectively.

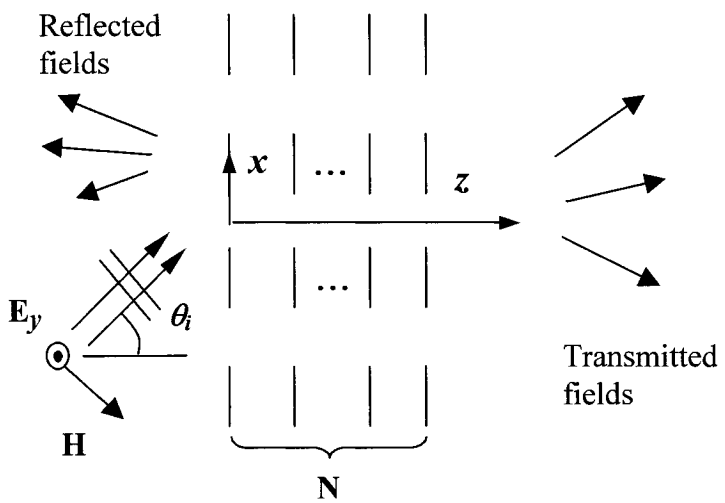

Fig.3.2 Transverse electric wave incidence (TE case).

Obviously, the scattering process by such a finite array of planar conducting disk lattices with varying disk size is quite complicated. To the author's knowledge, neither theoretical nor numerical analysis results have been reported in the literature. However, when the conditions of the above assumptions are met, the equivalent dipole concept used in the earlier work on artificial dielectrics [20,35] can also be applied to AMVHs with varying-size disks, except that the equivalent dipole moments for disks of different sizes will be different.

For small disks, the incident wave will induce a y-directed electric dipole (due to E_i^y) and z-directed magnetic dipole (due to H_i^z) at each disk, with moments being proportional to the total field at the disk center. The total field is the sum of the incident field and the interaction field due to the radiation from all of the neighboring disks. The radiated fields (interaction fields) are, in turn, proportional to the dipole moments. Then, equations that describe such relationships can be formulated, from which the dipole moments can be determined. It is, therefore, a self-consistent procedure where once the induced electric/magnetic dipole moments are determined, the interaction fields as well as the total scattered fields can be calculated. Considering the disk sizes are quite small compared to the disk spacing and the wavelengths used (assumption (iii)), the induced x-directed electric dipole at a disk due to the dissimilar sizes of its neighboring disks can be neglected, compared to the y-directed dipole that is parallel to the applied E-field.

Since the interaction between the applied field and the 3D disk arrays can be represented by the radiations of induced dipoles, the problem is converted to determine the dipole moments of a 3D y-directed electric dipole array and a 3D z-directed magnetic dipole array. Use of the symmetry of the problem in the y-direction allows perfect electric conducting (PEC) planes be inserted into both arrays at $y = \pm b/2$, and one needs only to consider the region bounded by any two consecutive PEC planes, as shown in Figs.3.3a and 3.3b, which includes a 2D array. In view of the periodicity of the lattice structure in the x-direction and the nature of the incident field, it can be seen that an induced dipole along a disk row parallel to the x-axis repeats itself at every Ith disk except for a phase difference (I is the number of patches in one period). Therefore, there are only total $I \times N$ unknown dipole moments in each 2D array in Fig.3.3.

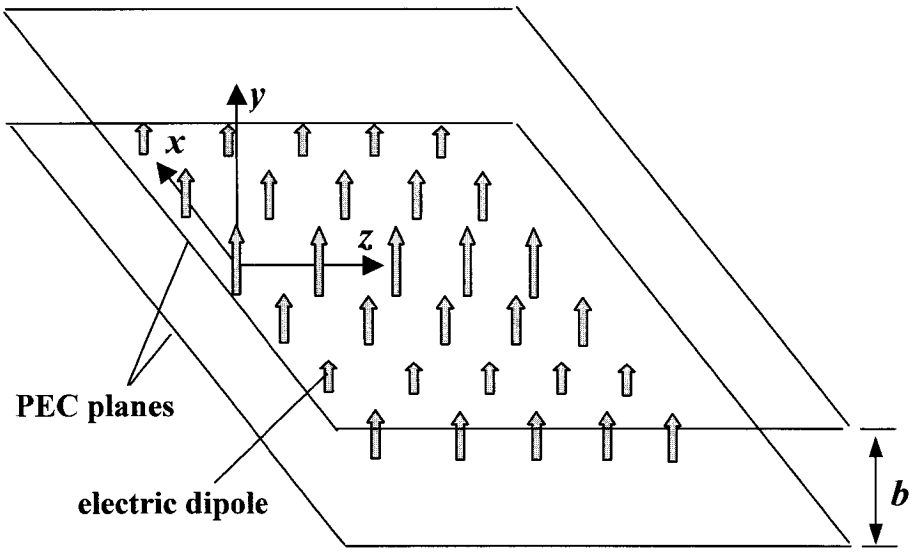

(a)

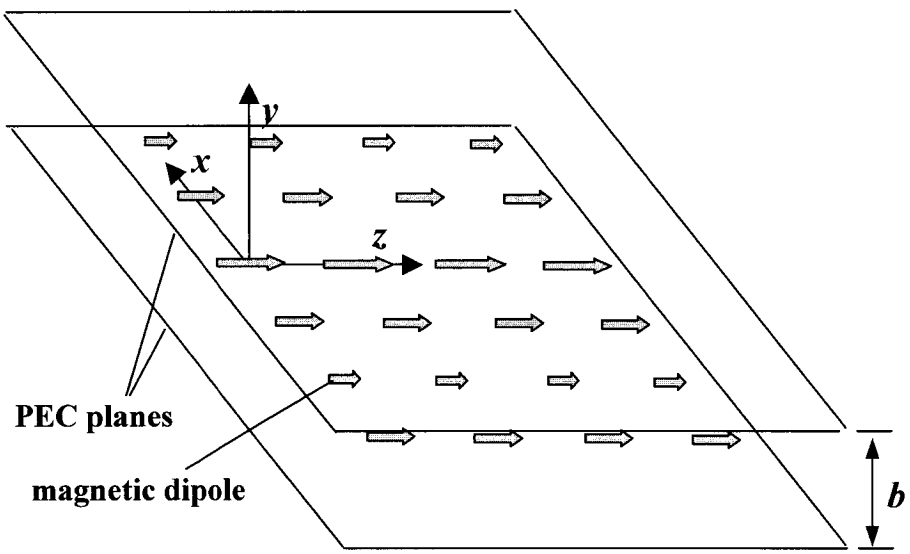

(b)

Fig.3.3 The equivalent problem: a 2D *y*-directed electric dipole array (a) plus a 2D *z*-directed magnetic dipole array (b), both located between two PEC planes and with the unknown dipole moments.

3.2.1 The dynamic interaction fields (TE)

First, consider a single electric/magnetic dipole at the origin bounded by two parallel PEC planes at $y = \pm b/2$, as shown in Fig.3.4a,b. The results for the dipole arrays in Fig.3.3 can be obtained by using the superposition principle. Considering the dipole directions, we use a vector potential $\boldsymbol{A} = A_y \hat{\boldsymbol{y}}$ for the electric dipole field

$$\boldsymbol{H} = \mu_0^{-1} \nabla \times \boldsymbol{A}, \quad \boldsymbol{E} = (j\omega\mu_0\varepsilon)^{-1}(\nabla\nabla \bullet \boldsymbol{A} + k^2 \boldsymbol{A}), \tag{3-2}$$

and a Hertzian vector potential $\boldsymbol{\Pi} = \Pi_z \hat{\boldsymbol{z}}$ for the magnetic dipole field

$$\boldsymbol{H} = k^2 \boldsymbol{\Pi} + \nabla\nabla \bullet \boldsymbol{\Pi}, \quad \boldsymbol{E} = -j\omega\mu_0 \nabla \times \boldsymbol{\Pi}, \tag{3-3}$$

where $\hat{\boldsymbol{y}}$ and $\hat{\boldsymbol{z}}$ are the unit vectors along the y- and z-direction respectively, and $\varepsilon = \varepsilon_0 \varepsilon_H$. The control equations for the potential functions then become

$$\begin{aligned} \nabla^2 A_y + k^2 A_y &= -(j\omega\mu_0) p\delta(x)\delta(y)\delta(z), \\ \nabla^2 \Pi_z + k^2 \Pi_z &= -m\delta(x)\delta(y)\delta(z), \end{aligned} \tag{3-4a,b}$$

where $\delta()$ is the unit impulse function, p and m are respectively the induced electric and magnetic dipole moments on the disk at the origin.

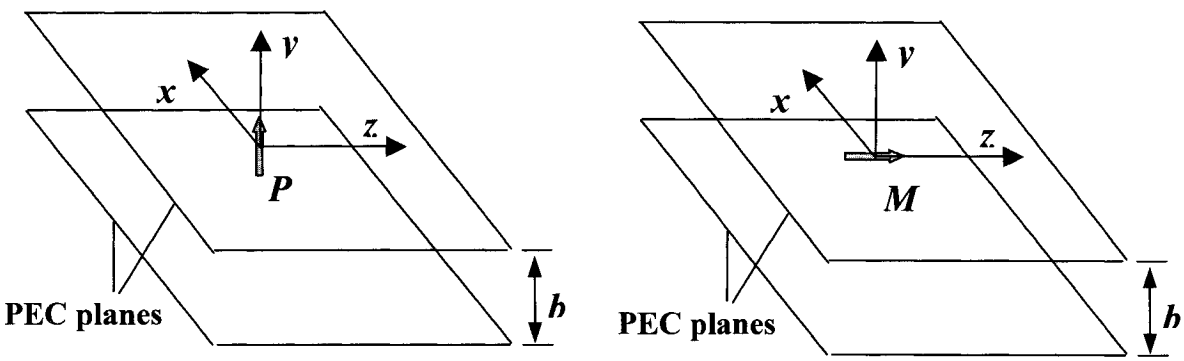

(a) electric dipole (b) magnetic dipole

Fig.3.4 Single dipole between two parallel perfect electric conducting planes.

The solutions of (3-4), which have their tangential electric field vanishing at the upper and lower PEC boundaries, can be expressed as follows

$$A_y = \frac{j\omega\mu_0}{2\pi b} p[K_0(jkr) + 2\sum_{n=1}^{\infty} \cos(2\pi ny/b) K_0(\gamma_n r)],$$
$$\Pi_z = \frac{m}{2\pi b}[K_0(jkr) + 2\sum_{n=1}^{\infty} \cos(2\pi ny/b) K_0(\gamma_n r)], \qquad \text{(3-5a,b,c)}$$
$$\gamma_n = \sqrt{(2\pi n/b)^2 - k^2},\ r = \sqrt{x^2 + z^2},$$

where K_0, the modified Bessel function of second kind, which will be proportional to the Hankel function $H_0^2()$ if the argument is imaginary, and will decay exponentially if the argument is real and large. Therefore, the first term in (3-5) represents a out-going cylindrical wave, and the series represents a localized field, since γ_n is real for $n>0$ (as $b << \lambda$). Considering $K_0(\gamma_n r)$ decays rapidly for large n, we only keep the $n=1$ term in the series.

Next, the potential for the entire dipole array (Fig.3.3) can be obtained by adding together each dipole's contribution (3-5) multiplied by a relative phase $\exp(-jk_x mla)$, and the results are given as follows for the electric and magnetic dipole arrays, respectively,

$$A_y = \frac{j\omega\mu_0}{2\pi b} \sum_{n=0}^{N-1} \sum_{i=0}^{I-1} \sum_{m=-\infty}^{\infty} p_{ni} e^{-jk_x mla} [K_0(jkr_{mi}^n) + 2\cos\frac{2\pi y}{b} K_0(\gamma_1 r_{mi}^n)],$$
$$\Pi_z = \frac{1}{2\pi b} \sum_{n=0}^{N-1} \sum_{i=0}^{I-1} \sum_{m=-\infty}^{\infty} m_{ni} e^{-jk_x mla} [K_0(jkr_{mi}^n) + 2\cos\frac{2\pi y}{b} K_0(\gamma_1 r_{mi}^n)], \qquad \text{(3-6a,b)}$$
$$\text{with } r_{mi}^n = \sqrt{(z - nc)^2 + (x - mla - ia)^2},$$

where p_{ni} (m_{ni}), the induced electric (magnetic) dipole moment at the ith disk within the mth period in a disk row located in nth lattice plane. It should be noted that if the spatial point where the potential is calculated is on a node of the lattice, the contribution from that dipole has to be removed from the summation. From the Poisson's summation formula [36], the following identity holds

$$\sum_{m=-\infty}^{\infty} e^{-jk_x mla} K_0(jk\sqrt{z^2 + (x - mla)^2}) = e^{-jk_x x} \frac{\pi}{a} \sum_{m=-\infty}^{\infty} \frac{e^{-v_m|z| - j2\pi mx/la}}{v_m}, \qquad \text{(3-7a,b)}$$
$$v_m = \sqrt{u_m^2 - k^2},\ v_0 = jk_z,\ u_m = 2\pi m/la + k_x$$

Applying (3-7a) to the infinite series in (3-6), and then from (3-2) and (3-3), the fields E^y, H^z due to the electric dipole array can be written as

$$E^{y,e} = \frac{1}{2\pi\varepsilon b}\{\frac{\pi k^2}{Ia}\sum_{n=0}^{N-1}\sum_{i=0}^{I-1} p_{ni} e^{jk_x ia} \sum_{m=-\infty}^{\infty} \frac{1}{v_m} e^{j2\pi mi/I} e^{-v_m|z-nc|-ju_m x}$$
$$-2\gamma_1^2 \cos(\frac{2\pi y}{b})\sum_{n=0}^{N-1}\sum_{i=0}^{I-1} p_{ni} \sum_{m=-\infty}^{\infty} e^{-jk_x mIa} K_0(\gamma_1 r_{mi}^n)\},$$
$$H^{z,e} = \frac{j\omega}{2\pi b}\{\frac{\pi}{Ia}\sum_{n=0}^{N-1}\sum_{i=0}^{I-1} p_{ni} e^{jk_x ia} \sum_{m=-\infty}^{\infty} \frac{u_m}{jv_m} e^{j2\pi mi/I} e^{-v_m|z-nc|-ju_m x} \qquad (3\text{-}8a,b)$$
$$-2\cos(\frac{2\pi y}{b})\sum_{n=0}^{N-1}\sum_{i=0}^{I-1} p_{ni} \sum_{m=-\infty}^{\infty} e^{-jk_x mIa} K_1(\gamma_1 r_{mi}^n) \frac{x-mIa-ia}{r_{mi}^n}\gamma_1\},$$

Similarly, the fields E^y, H^z due to the magnetic dipole array can be written as

$$E^{y,m} = \frac{j\omega\mu_0}{2\pi b}\{\frac{\pi}{Ia}\sum_{n=0}^{N-1}\sum_{i=0}^{I-1} m_{ni} e^{jk_x ia} \sum_{m=-\infty}^{\infty} \frac{u_m}{jv_m} e^{j2\pi mi/I} e^{-v_m|z-nc|-ju_m x}$$
$$-2\cos(\frac{2\pi y}{b})\sum_{n=0}^{N-1}\sum_{i=0}^{I-1} m_{ni} \sum_{m=-\infty}^{\infty} e^{-jk_x mIa} K_1(\gamma_1 r_{mi}^n) \frac{x-mIa-ia}{r_{mi}^n}\gamma_1\},$$
$$H^{z,m} = \frac{1}{2\pi b}\{\frac{\pi}{Ia}\sum_{n=0}^{N-1}\sum_{i=0}^{I-1} m_{ni} e^{jk_x ia} \sum_{m=-\infty}^{\infty} \frac{u_m^2}{v_m} e^{j2\pi mi/I} e^{-v_m|z-nc|-ju_m x} \qquad (3\text{-}9a,b)$$
$$+2\cos(\frac{2\pi y}{b})\sum_{n=0}^{N-1}\sum_{i=0}^{I-1} m_{ni} \sum_{m=-\infty}^{\infty} e^{-jk_x mIa}[(k^2+\gamma_1^2\frac{(z-nc)^2}{(r_{mi}^n)^2})K_0(\gamma_1 r_{mi}^n)$$
$$+\gamma_1\frac{(z-nc)^2-(x-mIa-ia)^2}{(r_{mi}^n)^3}K_1(\gamma_1 r_{mi}^n)]\},$$

The other components of the fields may also be derived from (3-2) and (3-3), but they can be shown to vanish at the y=0 plane, where the disk centers are located, except for H^x.

3.2.2 Determination of the induced dipole moments (TE)

With the interaction field given by (3-8) and (3-9), the total field at any disk center (lattice node) with indices (n', i') can be expressed as

$$E_{n'i'}^{y,tot} = E_i^y + E_{n'i'}^{y,e} + E_{n'i'}^{y,m}, \quad H_{n'i'}^{z,tot} = H_i^z + H_{n'i'}^{z,e} + H_{n'i'}^{z,m} \qquad (3\text{-}10)$$

where the interaction fields at the lattice node are defined as the limits $E^{y,e}_{n'i'} = E^{y,e}(x \to i'a, y = 0, z \to n'c)$, etc. The limit operation includes (i) subtracting the contribution of the dipole at $x=i'a$, $z=n'c$, $y=0$ from the interaction fields (3-8) and (3-9); (ii) calculating the singular asymptotic value of the modified Bessel function as its argument tends to zero; (iii) separating the divergent part in the infinite series as $n \to n'$ and $i \to i'$. The details of the procedure are given in Appendix A, and it shows that the two singular parts from (ii) and (iii) respectively will cancel each other.

The total fields act to polarize each disk, and thus the electric and magnetic dipole moments induced on a disk will be proportional to the total fields,

$$p_{n'i'} = \alpha^e_{i'}\varepsilon(E^y_i + E^{y,e}_{n'i'} + E^{y,m}_{n'i'}), \quad m_{n'i'} = \alpha^m_{i'}(H^z_i + H^{z,e}_{n'i'} + H^{z,m}_{n'i'}) \tag{3-11}$$

where $\alpha^e_{i'}$ and $\alpha^m_{i'}$ are the electric and magnetic polarizabilities of the i'th disk [20], respectively. They are independent of the index n since all the planar disk lattices are identical. It should be noted that the polarizability could be different at different lattice planes, then, $\alpha^e_{i'}$ and $\alpha^m_{i'}$ will be replaced by $\alpha^e_{n'i'}$ and $\alpha^m_{n'i'}$ and the following derivation is still valid. From (3-8) and (3-9), the interaction fields are linear functions of the dipole moments, and thus equations (3-11) are linear equations of the unknown dipole moments. To simplify the formulation, we introduce the "normalized" dipole moments and dimensionless parameters

$$\bar{p}^y_{n'i'} \equiv \frac{p^y_{n'i'}}{b^3\varepsilon E_0}, \quad \bar{m}^z_{n'i'} \equiv \frac{m^z_{n'i'}}{b^3 H_0}, \quad (\bar{b}, \bar{c}) = (\frac{b}{a}, \frac{c}{a}), \quad (\bar{k}, \bar{k}_x, \bar{k}_z, \bar{u}_m, \bar{v}_m) = a(k, k_x, k_z, u_m, v_m) \tag{3-12}$$

After carrying out the limit operation, the linear equations (3-11) can be expressed explicitly as

$$\begin{aligned}
\frac{b^3}{\alpha^e_{i'}}\bar{p}^y_{n'i'} &= e^{-j(\bar{k}_x i' + \bar{k}_z \bar{c} n')} + \sum_{n=0}^{N-1}\sum_{i=0}^{I-1}(A^{ee}\delta_{n'n}\delta_{i'i} + B^{ee}_{n'i'ni})\bar{p}^y_{ni} + \sum_{n=0}^{N-1}\sum_{i=0}^{I-1} B^{em}_{n'i'ni}\bar{m}^z_{ni}, \\
\frac{b^3}{\alpha^m_{i'}}\bar{m}^z_{n'i'} &= \sin\theta_i e^{-j(\bar{k}_x i' + \bar{k}_z \bar{c} n')} + \sum_{n=0}^{N-1}\sum_{i=0}^{I-1} B^{me}_{n'i'ni}\bar{p}^y_{ni} + \sum_{n=0}^{N-1}\sum_{i=0}^{I-1}(A^{mm}\delta_{n'n}\delta_{i'i} + B^{mm}_{n'i'ni})\bar{m}^z_{ni}, \\
& i' = 0,1,\ldots I-1, \quad n' = 0,1,\ldots, N-1,
\end{aligned} \tag{3-13}$$

where

$$A^{ee} = \frac{1}{\pi}\{1.202 + \frac{(\overline{kb})^2}{2}[\gamma + \frac{1}{2} + \ln\frac{I}{4\pi\overline{b}}] + \frac{(\overline{kb})^4}{96} + j\frac{(\overline{kb})^3}{6}\},$$

$$A^{mm} = \frac{1}{2\pi}\{1.202 + \frac{1}{3}(\frac{\pi b}{Ia})^2 + \frac{(\overline{kb})^2}{2}[1 - \gamma + \ln(\frac{16\pi}{\overline{k}^2 I\overline{b}}\sin^2\frac{\overline{kb}}{2})] + \frac{(\overline{kb})^4}{96} - j\frac{(\overline{kb})^3}{6}\}, \quad (3\text{-}14)$$

with Euler's constant $\gamma = 0.577$

and

$$B^{ee}_{n'i'ni} = \frac{(\overline{kb})^2}{2I}e^{-j\bar{k}_x(i'-i)}\{\frac{e^{-j\bar{k}_z|n'-n|\bar{c}}}{j\bar{k}_z} + \sum_{m=1}^{\infty}[\frac{1}{\bar{v}_m}e^{-\bar{v}_m|n'-n|\bar{c}}e^{-j2\pi m(i'-i)/I} + \frac{1}{\bar{v}_{-m}}e^{-\bar{v}_{-m}|n'-n|\bar{c}}e^{j2\pi m(i'-i)/I}$$
$$- \frac{I}{m\pi}\delta_{ii'}\delta_{nn'}]\} - \frac{(\bar{\gamma}_1\bar{b})^2}{\pi}\{K_0(\bar{\gamma}_1\bar{r}_0)|_{r_0\neq 0} + \sum_{m=1}^{\infty}[e^{-j\bar{k}_x ml}K_0(\bar{\gamma}_1\bar{r}_m) + e^{j\bar{k}_x ml}K_0(\bar{\gamma}_1\bar{r}_{-m})]\},$$

$$B^{em}_{n'i'ni} = B^{me}_{n'i'ni} = \frac{\overline{kb}^2}{2I}e^{-j\bar{k}_x(i'-i)}\{\frac{\bar{k}_x}{j\bar{k}_z}e^{-j\bar{k}_z|n'-n|\bar{c}} +$$
$$\sum_{m=1}^{\infty}[\frac{\bar{u}_m}{\bar{v}_m}e^{-\bar{v}_m|n'-n|\bar{c}}e^{-j2\pi m(i'-i)/I} + \frac{\bar{u}_{-m}}{\bar{v}_{-m}}e^{-\bar{v}_{-m}|n'-n|\bar{c}}e^{j2\pi m(i'-i)/I}]\} \quad (3\text{-}15)$$
$$- j\frac{\bar{\gamma}_1\overline{kb}^2}{\pi}\{\frac{i'-i}{\bar{r}_0}K_0(\bar{\gamma}_1\bar{r}_0)|_{r_0\neq 0} +$$
$$\sum_{m=1}^{\infty}[e^{-j\bar{k}_x ml}\frac{i'-i-mI}{\bar{r}_0}K_0(\bar{\gamma}_1\bar{r}_m) + e^{j\bar{k}_x ml}\frac{i'-i+mI}{\bar{r}_0}K_0(\bar{\gamma}_1\bar{r}_{-m})]\},$$

$$B^{mm}_{n'i'ni} = \frac{\bar{b}^2}{2I}e^{-j\bar{k}_x(i'-i)}\{\frac{\bar{k}_x^2}{j\bar{k}_z}e^{-j\bar{k}_z|n'-n|\bar{c}} + \sum_{m=1}^{\infty}[\frac{\bar{u}_m^2}{\bar{v}_m}e^{-\bar{v}_m|n'-n|\bar{c}}e^{-j2\pi m(i'-i)/I} - (\frac{I\bar{k}^2}{4\pi m} + \bar{u}_m)\delta_{ii'}\delta_{nn'}$$
$$+ \frac{\bar{u}_{-m}^2}{\bar{v}_{-m}}e^{-\bar{v}_{-m}|n'-n|\bar{c}}e^{j2\pi m(i'-i)/I} - (\frac{I\bar{k}^2}{4\pi m} - \bar{u}_{-m})\delta_{ii'}\delta_{nn'}]\}$$
$$+ \frac{\bar{b}^2}{\pi}\{[(\bar{k}^2 + \bar{\gamma}_1^2\frac{(n'-n)^2\bar{c}^2}{\bar{r}_0^2})K_0(\bar{\gamma}_1\bar{r}_0) + \bar{\gamma}_1\frac{(n'-n)^2\bar{c}^2 - (i'-i)^2}{\bar{r}_0^3})K_1(\bar{\gamma}_1\bar{r}_0)]|_{r_0\neq 0}$$
$$+ \sum_{m=1}^{\infty}e^{-j\bar{u}ml}[(\bar{k}^2 + \bar{\gamma}_1^2\frac{(n'-n)^2\bar{c}^2}{\bar{r}_m^2})K_0(\bar{\gamma}_1\bar{r}_m) + \bar{\gamma}_1\frac{(n'-n)^2\bar{c}^2 - (i'-i-mI)^2}{\bar{r}_m^3})K_1(\bar{\gamma}_1\bar{r}_m)]$$
$$+ \sum_{m=1}^{\infty}e^{j\bar{u}ml}[(\bar{k}^2 + \bar{\gamma}_1^2\frac{(n'-n)^2\bar{c}^2}{\bar{r}_{-m}^2})K_0(\bar{\gamma}_1\bar{r}_{-m}) + \bar{\gamma}_1\frac{(n'-n)^2\bar{c}^2 - (i'-i+mI)^2}{\bar{r}_{-m}^3})K_1(\bar{\gamma}_1\bar{r}_{-m})]\},$$

with $\bar{r}_{\pm m} = \sqrt{(n'-n)^2\bar{c}^2 + (i'-i\mp mI)^2}$.

The linear equation system (3-13), which has double indices for the unknowns and four indices for the coefficients, can be easily converted into the standard linear equation (1D unknown vector and 2D coefficient matrix) by re-labeling the unknowns and the

coefficients. One important fact about the coefficients $B^{ee}_{n'i'ni}$, etc. is that they only depend on the index differences of the source and field points. Use of this fact in the algorithm implementation can significantly reduce the number of coefficients to be calculated, from I^2N^2 to $(2I\text{-}1)N$. The actual computation in a 2.4GHz PC has shown that the CPU time used is reduced by an order of magnitude for a case with I=10 and N=80. It is also noted that the first infinite series in the coefficients $B^{ee}_{n'i'ni}$ (3-15) converges rapidly since v_m, given by (3-7a), becomes real (positive) as m moves few steps away from zero. The other infinite series that contains K_0 and/or K_1 also converges quickly as discussed before.

The electric and magnetic polarizabilities $\alpha^e_{i'}$ and $\alpha^m_{i'}$ can be approximated by the following expression [20] for sufficient small disks (kd<1)

$$\alpha^e = \frac{2}{3}d^3,\ \alpha^m = -\frac{1}{3}d^3 \tag{3-16a,b}$$

A better approximation was given by Eggimann [37], which includes up to the third order of kd

$$\begin{aligned}\alpha^e &= \frac{2}{3}d^3[1+(\frac{2}{15}-\frac{1}{24}\sin^2\theta_i)(kd)^2 - j\frac{(kd)^3}{9\pi}],\\ \alpha^m &= -\frac{1}{3}d^3[1-(\frac{1}{20}+\frac{1}{40}\sin^2\theta_i)(kd)^2 + j\frac{(kd)^3}{9\pi}].\end{aligned} \tag{3-17a,b}$$

Equation (3-17) will be used for the polarizabilities in the actual calculations.

3.2.3 The scattered far fields and the energy balance (TE)

The dipole interaction fields or radiation fields (3-8) and (3-9) can be used to calculate the scattered far fields. In fact, the second term in each equation in (3-8,9) represents a localized field because of the modified Bessel functions K_0 and K_1 with real arguments, while the first term consists of two types of Floquet modes: a finite number of propagation modes (for those m yielding imaginary v_m) and an infinite number of evanescent modes (for those m yielding real v_m). In the spatial regions that are far from the disk lattice array, the fields are dominated by the propagation modes, which can be abstracted from (3-8) and (3-9) as

$$
\begin{aligned}
\frac{E^{y}_{far}}{E_0} &= \frac{E^{y,e}_{far} + E^{y,m}_{far}}{E_0} = \sum_{m=M_1}^{M_2} \bar{k} W_m^{\pm} e^{\mp j|v_m|z - ju_m x}, \\
\frac{H^{z}_{far}}{H_0} &= \frac{H^{z,e}_{far} + H^{z,m}_{far}}{H_0} = \sum_{m=M_1}^{M_2} \bar{u}_m W_m^{\pm} e^{\mp j|v_m|z - ju_m x}, \\
\frac{H^{x}_{far}}{H_0} &= \frac{H^{x,e}_{far} + H^{x,m}_{far}}{H_0} = \sum_{m=M_1}^{M_2} j\bar{v}_m W_m^{\pm} e^{\mp j|v_m|z - ju_m x}, \\
W_m^{\pm} &= \frac{\bar{b}^2}{2I} \sum_{n=0}^{N-1} \sum_{i=0}^{I-1} \left(\frac{\bar{k}}{\bar{v}_m} \bar{p}_{ni} + \frac{\bar{u}_m}{\bar{v}_m} \bar{m}_{ni} \right) e^{j(u_m ia \pm |v_m| nc)}
\end{aligned}
\tag{3-18}
$$

where the upper (lower) sign is associated with the $z>Nc$ ($z<0$) zone, or the transmission (reflection) zone as shown in Fig.3.2, $[M_1, M_2]$ is the region of m where v_m is imaginary.

Then, once system equations (3-13) are solved for the "normalized" dipole moments, the transmitted wave field can be calculated by simply adding the incident field (3-1) to the total dipole radiation field (3-18) with the plus sign, while the reflected wave field can be obtained directly from the total dipole radiation field (3-18) by choosing the minus sign.

From the far field expressions (3-18), one can derive the energy conservation relation. We choose a region bounded by four planes: $x = x_0$, $x = x_0+Ia$, $z = L$, $z = -L$, with L being a sufficient large so that evanescent modes can be neglected, and x_0, an arbitrary number. Since the far fields (3-18) are actually two-dimensional fields, we choose unit thickness in the y direction. Considering there are no sources inside the region, the energy conservation law can be expressed as

$$
\begin{aligned}
0 &= \oiint \frac{1}{2} \mathrm{Re}[\boldsymbol{E} \times \boldsymbol{H}^*] \bullet \boldsymbol{n} dS \\
&= \int_{x_0}^{x_0+Ia} \frac{1}{2} \mathrm{Re}[\boldsymbol{E} \times \boldsymbol{H}^*]|_{z=L} \bullet \hat{\boldsymbol{z}} dx + \int_{x_0}^{x_0+Ia} \frac{1}{2} \mathrm{Re}[\boldsymbol{E} \times \boldsymbol{H}^*]|_{z=-L} \bullet (-\hat{\boldsymbol{z}}) dx \\
&\quad + \int_{-L}^{L} \frac{1}{2} \mathrm{Re}[\boldsymbol{E} \times \boldsymbol{H}^*]|_{x=x_0+Ia} \bullet \hat{\boldsymbol{x}} dz + \int_{-L}^{L} \frac{1}{2} \mathrm{Re}[\boldsymbol{E} \times \boldsymbol{H}^*]|_{x=x_0} \bullet (-\hat{\boldsymbol{x}}) dz
\end{aligned}
\tag{3-19}
$$

where a "*" denotes a complex conjugate. It can be shown that the third and fourth integrals in the right-hand side of the second equation will cancel each other because of the periodicity of the problem. Using the incident field (3-1) and scattered field (3-18), the first and the second integrals have been carried out and result is given as

$$1=\left|1+\bar{k}W_0^+\right|^2+\sum_{\substack{m=M_1\\ m\neq 0}}^{M_2}\frac{|\bar{v}_m|}{\bar{k}_z}\left|\bar{k}W_m^+\right|^2+\sum_{m=M_1}^{M_2}\frac{|\bar{v}_m|}{\bar{k}_z}\left|\bar{k}W_m^-\right|^2 \tag{3-20}$$

Here we call each term (corresponding to m) in the right-hand side of (3-20) a diffraction energy efficiency, if it has a "+"superscription, or a reflection energy efficiency, if it has a "–" superscription. The energy conservation relation (3-20), though not sufficient, is necessary for a correct solution, and will be checked in the following numerical results.

3.3 Transverse magnetic waves incidence (TM)

For TM excitation, the applied magnetic field is perpendicular to the plane of incidence, while the electric field is within the plane of incidence as shown in Fig.3.5. (It is also refereed to as parallel-polarization or H-polarization.) A TM plane wave with an incident angle of θ_i (Fig.3.5) has a form of

$$\begin{aligned} &H_i^y=H_0e^{-j(k_xx+k_zz)},\ (E_i^x,E_i^z)=(\cos\theta_i,-\sin\theta_i)E_0e^{-j(k_xx+k_zz)},\\ &\text{with}\quad k_x=k\sin\theta_i,\ k_z=k\cos\theta_i,\ k^2=\omega^2\mu_0\varepsilon_0\varepsilon_{\mathrm{H}},\ H_0=\eta^{-1}E_0. \end{aligned} \tag{3-21}$$

Here ε_{H}, k and η are the relative permittivity, propagation constant and characteristic impedance of the host medium, respectively.

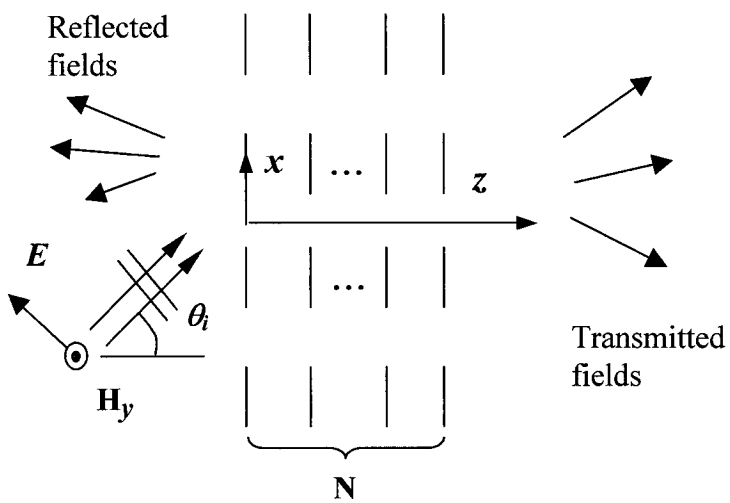

Fig.3.5 Transverse magnetic wave incidence (TM case).

For the TM incidence, the induced magnetic dipoles on conducting disks will be zero since the magnetic field is parallel to the disk surface; while the induced electric dipoles will follow the direction of tangential component of the applied electric field, i.e. along the x-direction. In a similar manner as for the TE case, the problem is converted to solving for the dipole moments of a 3D x-directed electric dipole array. The interaction fields as well as the total scattered fields can be calculated once the dipole moments are known. Use of the symmetry of the problem in the y=direction allows perfect magnetic conducting (PMC) planes be inserted into both arrays at $y = \pm b/2$, and one needs only to consider the region bounded by any two consecutive PMC planes, as shown in Figs.3.6a, which includes a 2D array. Also, by considering the periodicity of the problem along the x-direction, the total number of unknown dipoles is reduced to $I \times N$ in the 2D array.

3.3.1 The dynamic interaction fields (TM)

We start with the case of single electric/magnetic dipole at the origin, as shown in Fig.3.6b. The results for the dipole arrays in Fig.3.6a can be obtained by using the superposition principle. In view of the dipole direction, a vector potential $\boldsymbol{A} = A_x \hat{\boldsymbol{x}}$ is chosen for the electric dipole field

$$\boldsymbol{H} = \mu_0^{-1} \nabla \times \boldsymbol{A}, \quad \boldsymbol{E} = (j\omega\mu_0\varepsilon)^{-1} (\nabla\nabla \bullet \boldsymbol{A} + k^2 \boldsymbol{A}), \tag{3-22}$$

where $\hat{\boldsymbol{x}}$ is the unit vectors along the x-direction and $\varepsilon = \varepsilon_0 \varepsilon_H$. The control equation for the potential function then becomes

$$\nabla^2 A_x + k^2 A_x = -(j\omega\mu_0) p \delta(x)\delta(y)\delta(z), \tag{3-23}$$

where p is the induced electric dipole moment on the disk at the origin.

The solutions of (3-23), which have their tangential magnetic field vanishing at the upper and lower PMC boundaries, can be expressed as follows

$$\begin{aligned} A_x &= \frac{j\omega\mu_0}{2\pi b} p[K_0(jkr) + 2\sum_{n=1}^{\infty} \cos(2\pi n y / b) K_0(\gamma_n r)], \\ \gamma_n &= \sqrt{(2\pi n / b)^2 - k^2}, \; r = \sqrt{x^2 + z^2}, \end{aligned} \tag{3-24a,b}$$

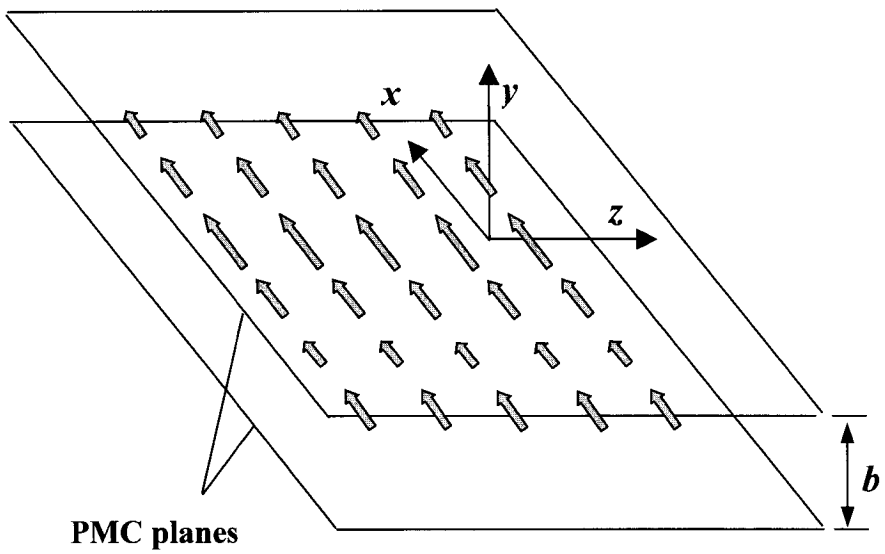

(a)

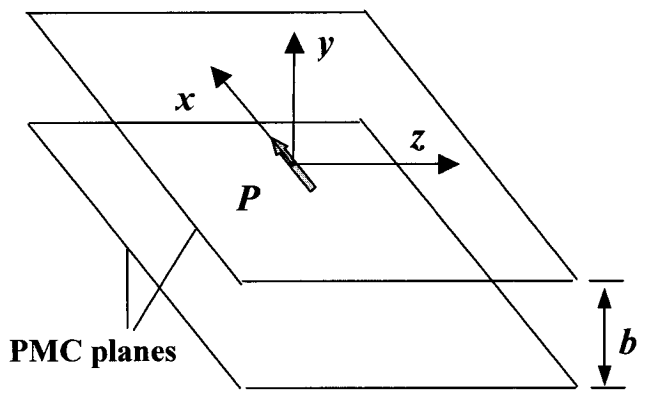

(b)

Fig.3.6 (a) The equivalent 2D x-directed electric dipole array located between two perfect magnetic conducting (PMC) planes at $y = \pm b/2$, and (b) the corresponding single electric dipole problem.

where all the symbols have the same meaning as in the TE case. Based on the same arguments as in Sec.3.2, the higher order terms (n>2) in the series of (3-24) can be dropped, and by superposing each dipole's contribution (3-24) multiplied by a relative phase delay exp(-$jk_x mIa$), the total potential for the entire dipole array (Fig.3.6a) can be written as

$$A_x = \frac{j\omega\mu_0}{2\pi b}\sum_{n=0}^{N-1}\sum_{i=0}^{I-1}\sum_{m=-\infty}^{\infty} p_{ni} e^{-jk_x mIa}[K_0(jkr_{mi}^n) + 2\cos\frac{2\pi y}{b} K_0(\gamma_n r_{mi}^n)], \quad \text{with } r_{mi}^n = \sqrt{(z-nc)^2 + (x-mIa-ia)^2}, \tag{3-25}$$

where p_{ni}, the induced electric dipole moment at the ith disk within the mth period in a disk row located in nth lattice plane. To calculate the field at a lattice node (disk center), the contribution from that dipole has to be removed from the summation. Applying the Poisson's summation formula (3-7) to (3-25), and then using (3-22), the fields $E^{x,e}$ can be written as

$$\begin{aligned} E^{x,e} = \frac{1}{2\pi b\varepsilon}\{&\frac{\pi}{Ia}\sum_{n=0}^{N-1}\sum_{i=0}^{I-1} p_{ni} e^{jk_x ia}\sum_{m=-\infty}^{\infty}(-v_m) e^{j2\pi mi/I} e^{-v_m|z-nc|-ju_m x} \\ &+ 2\cos(\frac{2\pi y}{b})\sum_{n=0}^{N-1}\sum_{i=0}^{I-1} p_{ni}\sum_{m=-\infty}^{\infty} e^{-jk_x mIa}[(k^2 + \gamma_1^2\frac{(x-mIa-ia)^2}{(r_{mi}^n)^2})K_0(\gamma_1 r_{mi}^n) \\ &+ \gamma_1\frac{(x-mIa-ia)^2 - (z-nc)^2}{(r_{mi}^n)^3} K_1(\gamma_1 r_{mi}^n)]\}, \end{aligned} \tag{3-26}$$

3.3.2 Determination of the induced dipole moments (TM)

The total electric field will be the summation of incident field and dipole radiation field (interaction field). At a disk center (lattice node) with indices (n',i'), the similar limit operation [35] has to be performed to evaluate the field

$$E_{n'i'}^{x,tot} = E_i^x + E_{n'i'}^{x,e}(x \to i'a, y = 0, z \to n'c), \tag{3-27}$$

which includes (i) subtracting the contribution of the dipole at x=i'a , z=n'c, y=0 from the interaction field (3-26); (ii) calculating the singular asymptotic value of the modified Bessel function as its argument tends to zero; (iii) separating the divergent part in the infinite series as $n \to n$' and $i \to i$'. It can be shown that the two singular parts from (ii) and (iii) respectively

will cancel each other. For brief, the detail derivations of the limit operation are omitted here and only the final results are given below.

Since the induced electric dipole at a disk is proportional to the total fields at the disk center, we have

$$p_{n'i'} = \alpha_{i'}^{e} \varepsilon (E_{i}^{x} + E_{n'i'}^{x,e}) \tag{3-28}$$

where $\alpha_{i'}^{e}$, the electric polarizability of the i'th disk under TM excitation, which for sufficient small disks, is the same as (3-16a) under TE excitation, and for disk size range up to third order of kd, is given by [37]

$$\alpha^{e} = \frac{2}{3} d^{3} [1 + (\frac{2}{15} - \frac{1}{40} \sin^{2} \theta_{i})(kd)^{2} - j \frac{(kd)^{3}}{9\pi}], \tag{3-29}$$

After carrying out the limit operation and by using the "normalized" dipole moments and dimensionless parameters given by (3-12), the equations (3-28) can be expressed as

$$\frac{b^{3}}{\alpha_{i'}^{e}} \bar{p}_{n'i'}^{x} = \cos\theta_{in} e^{-j(\bar{k}_{x} i' + \bar{k}_{z} \bar{c} n')} + \sum_{n=0}^{N-1} \sum_{i=0}^{I-1} (A \delta_{n'n} \delta_{i'i} + B_{n'i'ni}) \bar{p}_{ni}^{y}, \tag{3-30}$$
$$i' = 0,1,...I-1, \quad n' = 0,1,...,N-1,$$

where

$$A = \frac{-1}{2\pi} \{1.202 - \frac{1}{3} (\frac{\pi b}{Ia})^{2} + \frac{(\bar{kb})^{2}}{2} [\ln(\frac{16\pi}{\bar{k}^{2} I\bar{b}} \sin^{2} \frac{\bar{kb}}{2}) - \gamma] + \frac{(\bar{kb})^{4}}{96} - j \frac{(\bar{kb})^{3}}{3}\}, \tag{3-31}$$

$$\begin{aligned} B_{n'i'ni} = {} & \frac{\bar{b}^{2}}{2I} e^{-j\bar{k}_{x}(i'-i)} \{ j\bar{k}_{z} e^{-j\bar{k}_{z}|n'-n|\bar{c}} + \sum_{m=1}^{\infty} [\bar{v}_{m} e^{-\bar{v}_{m}|n'-n|\bar{c}} e^{-j2\pi m(i'-i)/I} - (\bar{u}_{m} - \frac{I\bar{k}^{2}}{4\pi m}) \delta_{ii'} \delta_{nn'} \\ & + \bar{v}_{-m} e^{-\bar{v}_{-m}|n'-n|\bar{c}} e^{j2\pi m(i'-i)/I} - (-\bar{u}_{-m} - \frac{I\bar{k}^{2}}{4\pi m}) \delta_{ii'} \delta_{nn'}] \} \\ & + \frac{\bar{b}^{2}}{\pi} \{ [(\bar{k}^{2} + \bar{\gamma}_{1}^{2} \frac{(i'-i)^{2}}{\bar{r}_{0}^{2}}) K_{0}(\bar{\gamma}_{1}\bar{r}_{0}) + \bar{\gamma}_{1} \frac{(i'-i)^{2} - (n'-n)^{2}\bar{c}^{2}}{\bar{r}_{0}^{3}}) K_{1}(\bar{\gamma}_{1}\bar{r}_{0})] |_{r_{0} \neq 0} \\ & + \sum_{m=1}^{\infty} e^{-j\bar{u}mI} [(\bar{k}^{2} + \bar{\gamma}_{1}^{2} \frac{(i'-i-mI)^{2}}{\bar{r}_{m}^{2}}) K_{0}(\bar{\gamma}_{1}\bar{r}_{m}) + \bar{\gamma}_{1} \frac{(i'-i-mI)^{2} - (n'-n)^{2}\bar{c}^{2}}{\bar{r}_{m}^{3}}) K_{1}(\bar{\gamma}_{1}\bar{r}_{m})] \\ & + \sum_{m=1}^{\infty} e^{j\bar{u}mI} [(\bar{k}^{2} + \bar{\gamma}_{1}^{2} \frac{(i'-i+mI)^{2}}{\bar{r}_{-m}^{2}}) K_{0}(\bar{\gamma}_{1}\bar{r}_{-m}) + \bar{\gamma}_{1} \frac{(i'-i+mI)^{2} - (n'-n)^{2}\bar{c}^{2}}{\bar{r}_{-m}^{3}}) K_{1}(\bar{\gamma}_{1}\bar{r}_{-m})] \} \end{aligned} \tag{3-32}$$

with Euler's constant $\gamma = 0.577$, and $\bar{r}_{\pm m} = \sqrt{(n'-n)^2 \bar{c}^2 + (i' - i \mp mI)^2}$.

3.3.3 The scattered far fields and the energy balance (TM)

The scattered far fields can be obtained from (3-26) by neglecting (i) the 2nd term (2nd triple summations) which represent a localized field because of the modified Bessel functions K_0 and K_1 with real arguments, and (ii) the terms in the 1st triple summations whose m index yielding real v_m (corresponding to evanescent modes). The results can be written as

$$\frac{E^x_{far}}{E_0} = \sum_{m=M_1}^{M_2} \bar{v}_m T_m^{\pm} e^{\mp j|v_m|z - ju_m x}, \qquad \frac{H^y_{far}}{H_0} = \sum_{m=M_1}^{M_2} (\pm j\bar{k}) T_m^{\pm} e^{\mp j|v_m|z - ju_m x},$$
$$T_m^{\pm} = -\frac{\bar{b}^2}{2I} \sum_{n=0}^{N-1} \sum_{i=0}^{I-1} \bar{p}_{ni} e^{j(u_m ia \pm |v_m| nc)} \tag{3-33}$$

where the upper (lower) sign is associated with the $z>Nc$ ($z<0$) zone, or the transmission (reflection) zone as shown in Fig.3.5, $[M_1, M_2]$ is the region of m where v_m is imaginary.

Then, once system equations (3-30) are solved for the "normalized" dipole moments, the transmitted wave field can be calculated by simply adding the incident field (3-21) to the total dipole radiation field (3-33) with the plus sign, while the reflected wave field can be obtained directly from the total dipole radiation field (3-33) by choosing the minus sign.

Following the same procedure as in Sec.3.2.3, the energy conservation relation is derived as below

$$1 = \left|1 + j\bar{k} T_0^+\right|^2 + \sum_{\substack{m=M_1 \\ m\neq 0}}^{M_2} \frac{|\bar{v}_m|}{\bar{k}_z} \left|\bar{k} T_m^+\right|^2 + \sum_{m=M_1}^{M_2} \frac{|\bar{v}_m|}{\bar{k}_z} \left|\bar{k} T_m^-\right|^2 \tag{3-34}$$

Again, each term (corresponding to m) in the right-hand side of (3-34) is called a diffraction energy efficiency, if it has a "+"superscription, or a reflection energy efficiency, if it has a "–" superscription. The energy conservation relation (3-34) can be used to verify the above formulism through numerical examples.

3.4 Some numerical results

First, consider an AMVH designed with the following parameters:
c = 0.5mm, $a = b$ = 0.6mm, ε_H = 3.0, I = 10, N = 81 and f = 30GHz. The disk diameters in one period are [0.26 0.289 0.345 0.393 0.424 0.434 0.424 0.393 0.345 0.289] (mm). This design produces an effective modulation of the relative permittivity as (will be explained in the next chapter)

$$\varepsilon_{er}(i) = 3.6 + 0.4\cos[2\pi(i-1)/10] \tag{3-35}$$

It is easy to verify from (3-7b) that for the given case, the only two propagating modes in the scattered field are the m = 0 and −1 orders (the corresponding v_m are imaginary). To test the accuracy of the analytical method proposed here, the infinite series in the coefficients in (3-15) was truncated at m = 5, 10, 20 and 50 terms and calculated the respective energy conservation relation (3-20) for 40 different angles of incidence. The maximum relative errors in (3-20) for the four truncations are 2%, 0.9%, 0.5%, and 0.2% respectively. It is thus decided to retain 50 terms in the series for all the following calculations (computing time increase is not significant from 20 terms to 50 terms).

Figure 3.7a shows the predicted amplitudes of the two waves in the transmission side of the hologram as functions of the angle of incidence, assuming unit amplitude of the incident wave, and hereafter. As seen from the figure, for the incidence angles between 25^0 and 33^0, the dominant wave in the transmitted field switches from the 0-order mode to the −1-order mode, the former is in the direction of the incident wave, whereas the latter is a diffraction wave into the opposite side about the normal. The maximum coupling to the diffraction wave (near 100%) occurs at an angle of about 29^0 from the figure, which is in fact the Bragg angle that has a designed value of 28.8^0 for the frequency. The results by neglecting the magnetic dipoles' contribution (as shown in Sec. 3.2) are also plotted in the same figure for comparison. As seen, the magnetic polarization effect is indeed quite small for AMVHs made of cascaded planer disk lattices, while electrical dipoles play the key role in modulating the host medium's dielectric constant. The predicted amplitudes of the two waves in the reflection side of the hologram are shown in Figure 3.7b. The artificial volume hologram is seen to be basically a transmissive device that has little reflection for a wide range of angle of incidence (less than −14dB in terms of return loss).

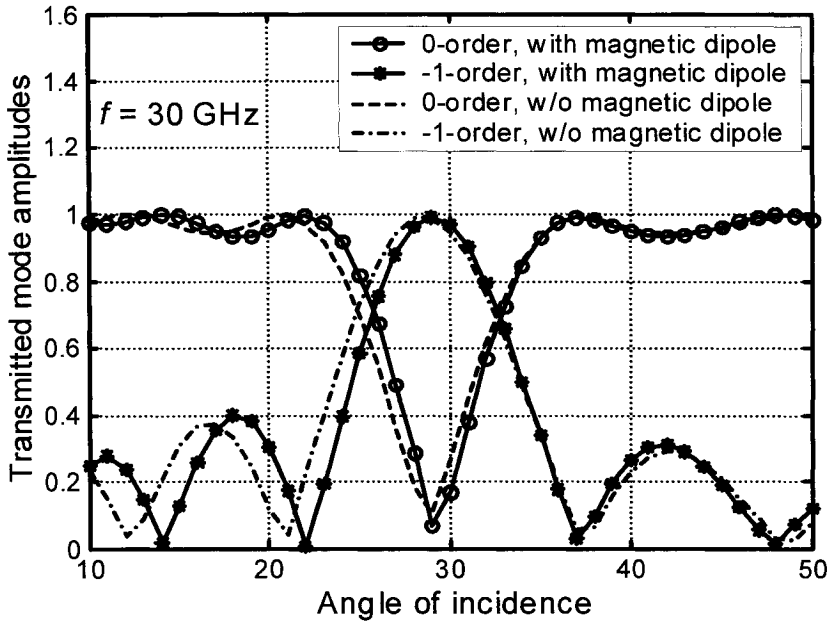

(a) Transmitted wave modes

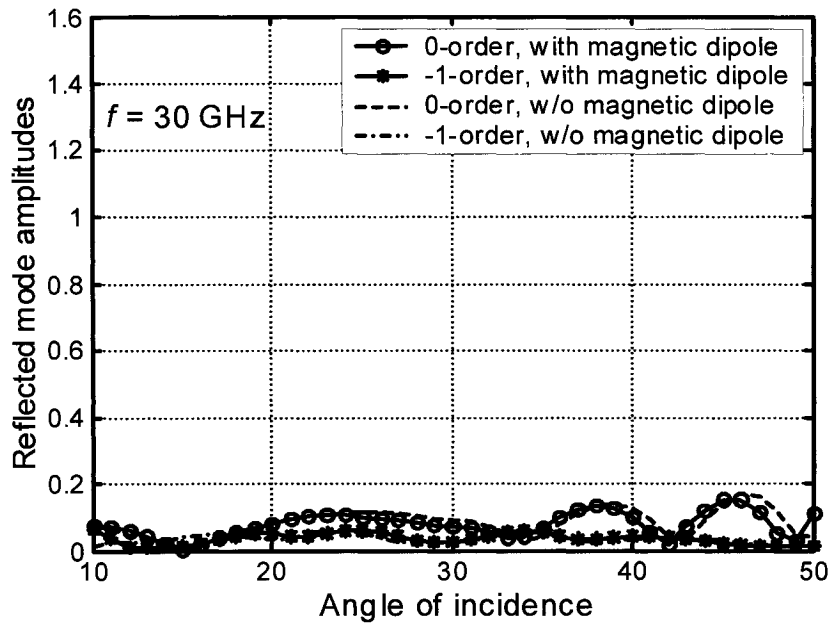

(b) Reflected wave modes

Fig.3.7 Predicted wave amplitudes of the two propagating modes (a) in transmission side, (b) in reflection side, under a TE plane wave incidence (1st example). (The scales of the two figures are set to be same for easy comparison, though the reflection modes are barely seen under this scale.)

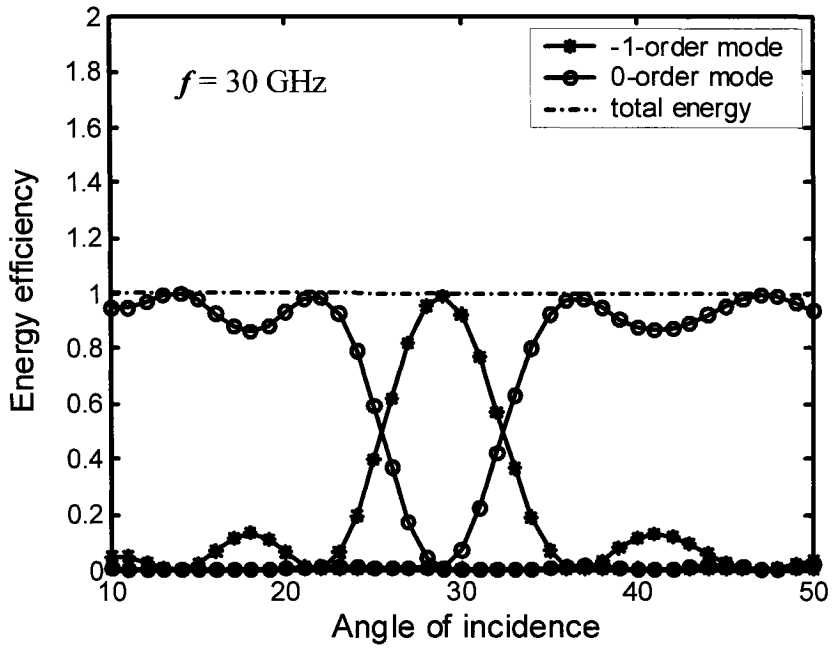

Fig.3.8 Predicted energy efficiencies of the transmitted and the reflected waves, under a TE plane wave incidence.

The predicted energy efficiencies (see eq.(3-20)) for the propagating modes and the total energy balance are shown in Fig.3.8, where the data points near the zero line (horizontal axis) are the energy efficiencies of the two reflected modes. The energy conservation law (3-20) is satisfied to an extent of ±0.5% for the entire angle range.

Next, consider a second AMVH design with the following parameters: c = 0.5mm, $a = b$ = 0.62mm, ε_H = 3.0, I = 12, N = 91 and f = 30GHz. The disk diameters in one period are [0.268 0.29 0.336 0.383 0.419 0.442 0.45 0.442 0.419 0.383 0.336 0.29 0.268] (mm). This hologram has a Bragg angle of 22.7^0, which is also the angle formed by the normal and either of the two symmetrical recording beams. The predicted results are shown in Fig.3.9a,b, where a similar wave mode conversion phenomenon (0-order mode to −1-order mode) is observed at the Bragg angle. A general conclusion drawn from these examples is that when the incident beam falls in the neighbor of the Bragg angle (a small region of about 8^0 for the two examples), the forward scattered beam is along the diffraction (the −1-order) direction; whereas, when the incident beam falls out of that region, the

forward scattered beam is along the incidence direction (or 0-order direction, also called the direct transmission direction).

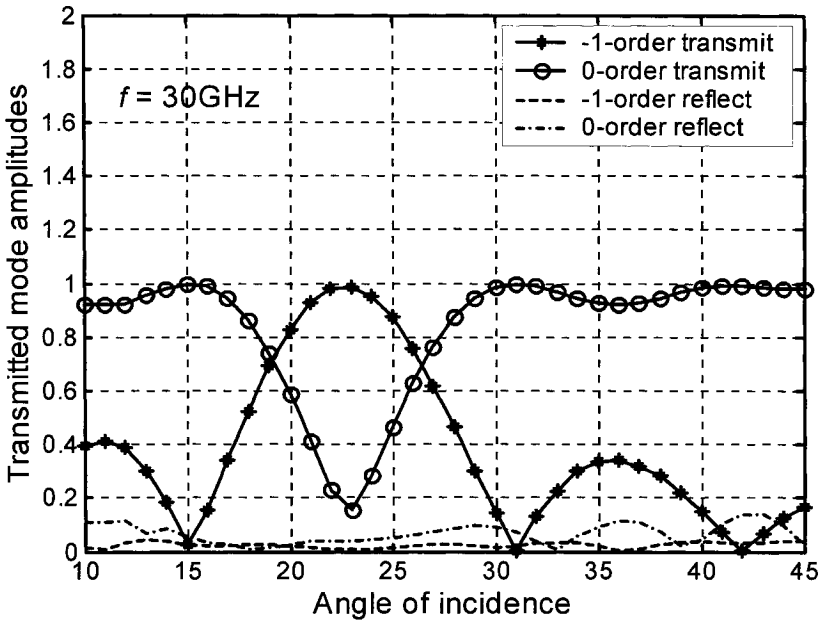

(a) Mode amplitudes

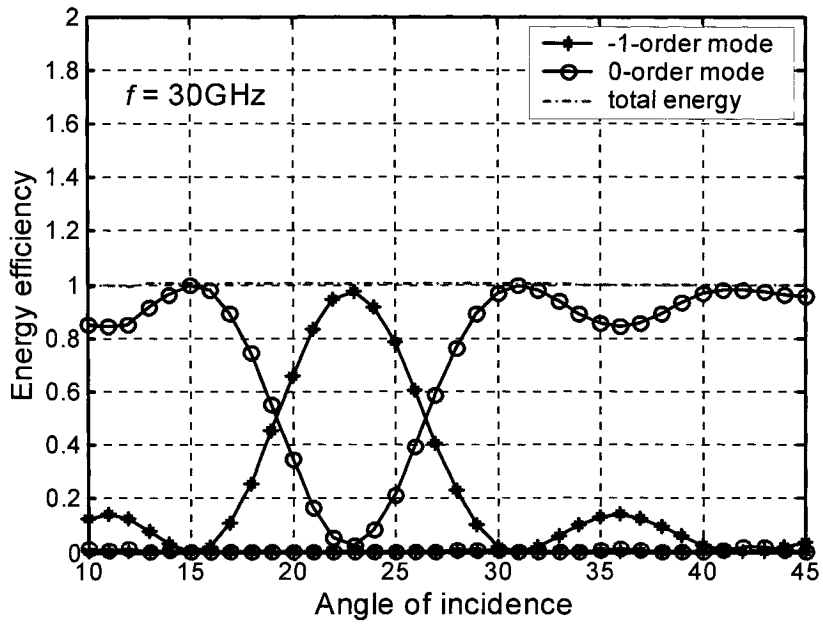

(b) Mode energy efficiencies

Fig.3.9 Predicted (a) wave amplitudes, (b) energy efficiencies, of the two propagating modes under a TE plane wave incidence (2nd example).

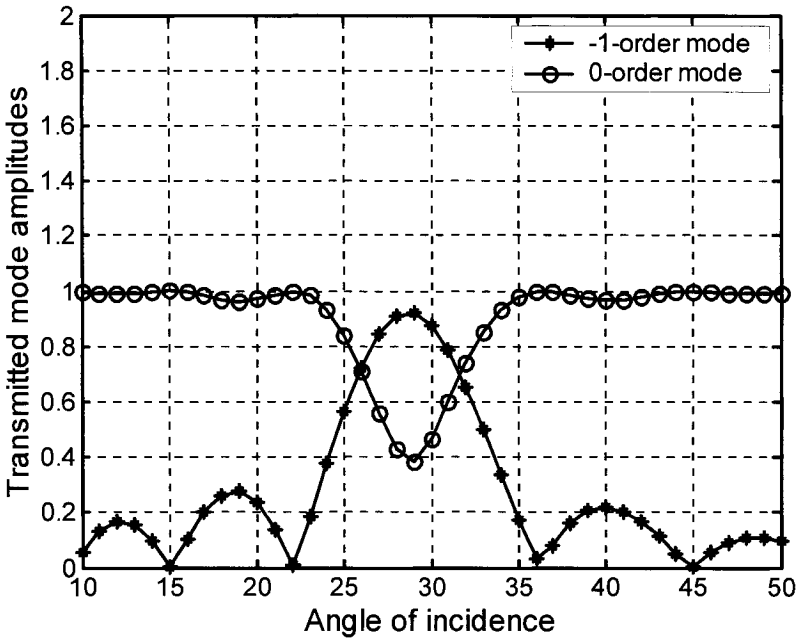

(a) Mode amplitude

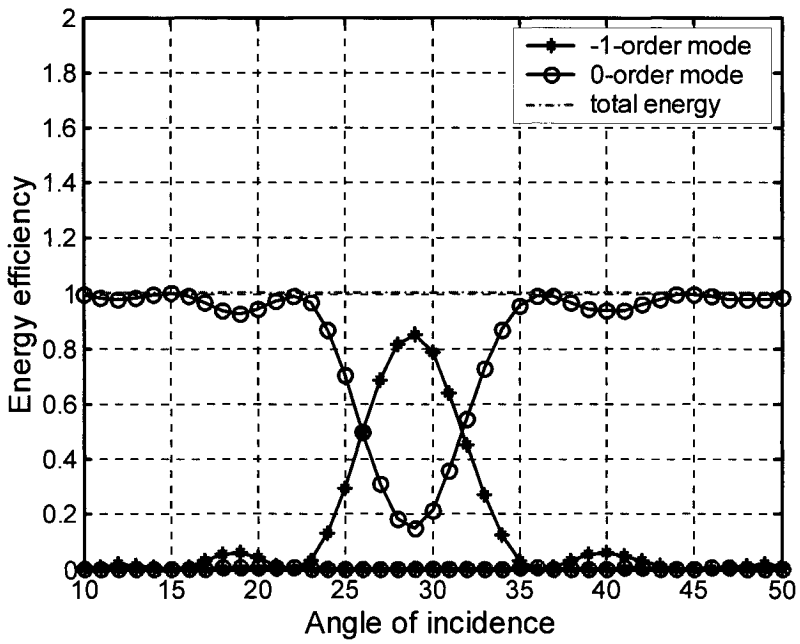

(b) Mode energy efficiencies

Fig.3.10 Predicted (a) wave amplitudes in transmission side, (b) energy efficiencies, of the two propagating modes, under a TM plane wave incidence.

Finally, consider the same AMVH as in the first example but put it in a TM setup as depicted in Fig.3.5. With a TM plane wave incidence, one still have two propagating modes in the scattered field at f = 30GHz, i.e. the m = 0 and –1 orders (the corresponding v_m are imaginary). The simulation results are given in Fig.3.10. As seen, a similar wave mode conversion phenomenon (0-order mode to –1-order mode) occurs around the Bragg angle of 29^0. Again, the energy conservation law is seen to be satisfied quite well in Fig.3.10b. However, the wave beam conversion efficiency is lower compared to the TE case. This is because for the TM case, the tangential electric field of the incident wave that polarizes the conducting disks decreases as the angle of incidence increases. As a result, the induced electric dipole moments and therefore the effective dielectric modulation are weaker for the TM case, except for the normal incidence where $\theta_{in} = 0^0$.

3.5 Slanted holograms with single holographic grating

It is mentioned in Sec.3.1 that when the two recording beams are not symmetrical about the normal of a hologram, the resulting holographic grating will be slanted at a certain angle with respect to the normal. In AMVH realization of a slanted holographic grating, each lattice layer will have a certain displacement δ in the x-direction with respect to its preceding layer (from left to right), as shown in Fig.3-11. The slant angle from the normal direction is given by

$$tg\varphi = \delta / c \tag{3-36}$$

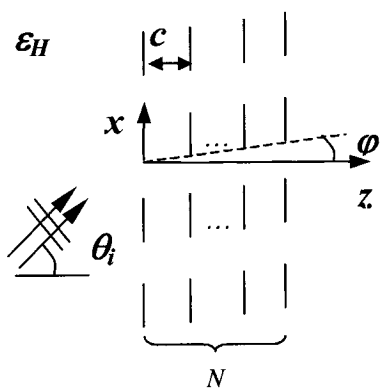

Fig.3-11 A finite cascade of the planar disk lattices with a slant angle of φ.

To simplify the analysis of such a slanted cascade of planar conducting disk lattices of varying disk size, the procedure described in Sec.3.2 will be used with the magnetic dipoles' contribution being neglected, since the latter has been shown quite small in the above numerical examples, as compared with the electric dipoles' contribution. Also, only the TE case is considered below; while the TM case can be treated in a similar manner.

3.5.1 The dynamic interaction fields (TE)

The following derivation uses the procedure developed by the author in [38]. In formulating the total potential function by phase delaying and adding each electric dipole's contribution, the relative phase delay will be $\exp[-jk_x(mIa+n\delta)]$ instead of $\exp(-jk_x mIa)$ to include each layer's displacement; so will be the distance calculation.

By considering this, equation (3-6a) can be re-written, for the slanted grating, as

$$A_y = \frac{j\omega\mu_0}{2\pi b}\sum_{n=0}^{N-1}\sum_{i=0}^{I-1}\sum_{m=-\infty}^{\infty} p_{ni}e^{-jk_x(mIa+n\delta)}[K_0(jkr_{mi}^n)+2\cos\frac{2\pi y}{b}K_0(\gamma_n r_{mi}^n)], \quad \text{with } r_{mi}^n=\sqrt{(z-nc)^2+(x-mIa-ia-n\delta)^2}, \tag{3-37}$$

For most cases, δ is much smaller than a, so its effect in the distance calculation can be neglected, but its contribution to the phase calculation should be retained. Then, equation (3-8a) becomes

$$E^{y,e} = \frac{1}{2\pi\varepsilon b}\{\frac{\pi k^2}{Ia}\sum_{n=0}^{N-1}\sum_{i=0}^{I-1}p_{ni}e^{jk_x ia}\sum_{m=-\infty}^{\infty}\frac{1}{v_m}e^{j2\pi m(ia+n\delta)/Ia}e^{-v_m|z-nc|-ju_m x} - 2\gamma_1^2\cos(\frac{2\pi y}{b})\sum_{n=0}^{N-1}\sum_{i=0}^{I-1}p_{ni}\sum_{m=-\infty}^{\infty}e^{-jk_x(mIa+n\delta)}K_0(\gamma_1 r_{mi}^n)\}, \tag{3-38}$$

with $r_{mi}^n \approx \sqrt{(z-nc)^2+(x-mIa-ia)^2}$

Following the same procedure for deriving the field at the disk centers as in Sec.3.2.2 and using the dimensionless parameters given in (3-12), the final linear equation system for the "normalized" dipole moments is re-written as

$$\frac{b^3}{\alpha_{i'}^e}\bar{p}_{n'i'}^y = e^{-j(\bar{k}_x i'+\bar{k}_z \bar{c} n')} + \sum_{n=0}^{N-1}\sum_{i=0}^{I-1}(A^{ee}\delta_{n'n}\delta_{i'i} + B_{n'i'ni}^{ee})\bar{p}_{ni}^y, \qquad (3\text{-}39)$$
$$i' = 0,1,\ldots I-1, \quad n' = 0,1,\ldots,N-1,$$

where,

$$A^{ee} = \frac{1}{\pi}\{1.202 + \frac{(\overline{kb})^2}{2}[\gamma + \frac{1}{2} + \ln\frac{I}{4\pi\bar{b}}] + \frac{(\overline{kb})^4}{96} + j\frac{(\overline{kb})^3}{6}\}, \qquad (3\text{-}40)$$
with Euler's constant $\gamma = 0.577$

$$B_{n'i'ni}^{ee} = \frac{(\overline{kb})^2}{2I}e^{-j\bar{k}_x(i'-i)}\{\frac{e^{-j\bar{k}_z|n'-n|\bar{c}}}{j\bar{k}_z} + \sum_{m=1}^{\infty}[\frac{e^{-\bar{v}_m|n'-n|\bar{c}}e^{-j2\pi m[(i'-i)+(n'-n)\bar{\delta}/I}}{\bar{v}_m} + \frac{e^{-\bar{v}_{-m}|n'-n|\bar{c}}e^{j2\pi m[(i'-i)+(n'-n)\bar{\delta}/I}}{\bar{v}_{-m}} - \frac{I}{m\pi}\delta_{ii'}\delta_{nn'}]\} \qquad (3\text{-}41)$$
$$-\frac{(\bar{\gamma}_1\bar{b})^2}{\pi}e^{-j\bar{k}_x(n'-n)\bar{\delta}}\{K_0(\bar{\gamma}_1\bar{r}_0)|_{r_0\neq 0} + \sum_{m=1}^{\infty}[e^{-j\bar{k}_x mI}K_0(\bar{\gamma}_1\bar{r}_m) + e^{j\bar{k}_x mI}K_0(\bar{\gamma}_1\bar{r}_{-m})]\},$$

with $\bar{r}_{\pm m} = \sqrt{(n'-n)^2\bar{c}^2 + (i'-i\mp mI)^2}$, $\bar{\delta} = \delta/a$.

3.5.2 Numerical results

Slanted holographic grating can be used in the design of an AMVH to control the transmitted beam to the desired direction. Let's re-consider the first AMVH example in Sec.3.4 by introducing three different slant angles $\varphi = 2.75^0$, 5.48^0, and -2.75^0, respectively. Figures 3-12 to 3-14 show the predicted results for the three slanted holograms. It is seen from the figures that the –1-order transmitted wave reaches its maximum as the incidence angle is about 32^0, 35^0, and 26^0 for the three cases, respectively. It can be predicted from (3-7b) that at these incidence angles, the diffraction angles of the –1-order wave with respect to the normal are 25.6^0, 22.9^0, and 31.6^0, respectively. In optical holography [21], this corresponds to the cases where the object and reference beams used to form the interference pattern in emulsions are not symmetrical about the normal of holograms.

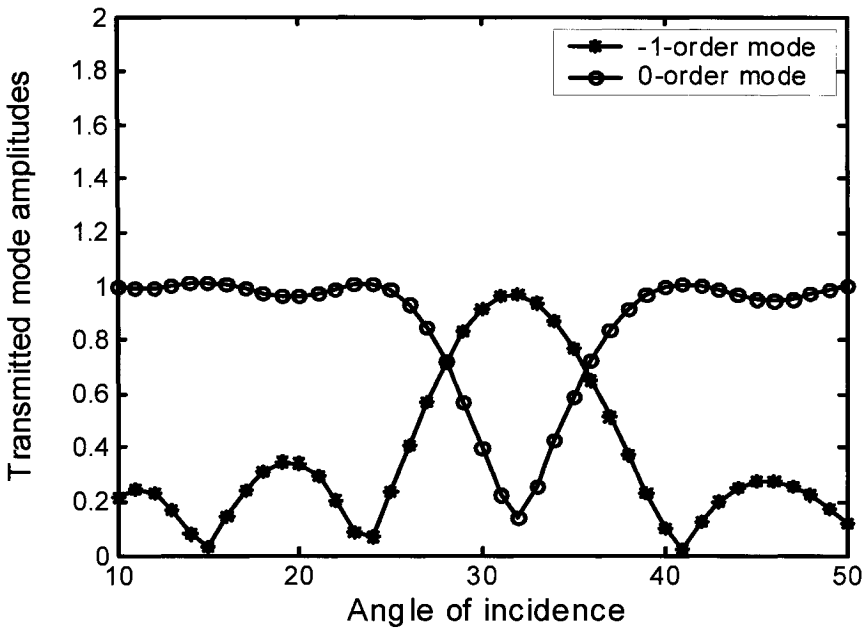

Fig.3-12 Predicted amplitudes of the two transmitted waves for a slanted AMVH with a slant angle of 2.75^0 ($\delta/a = 0.04$).

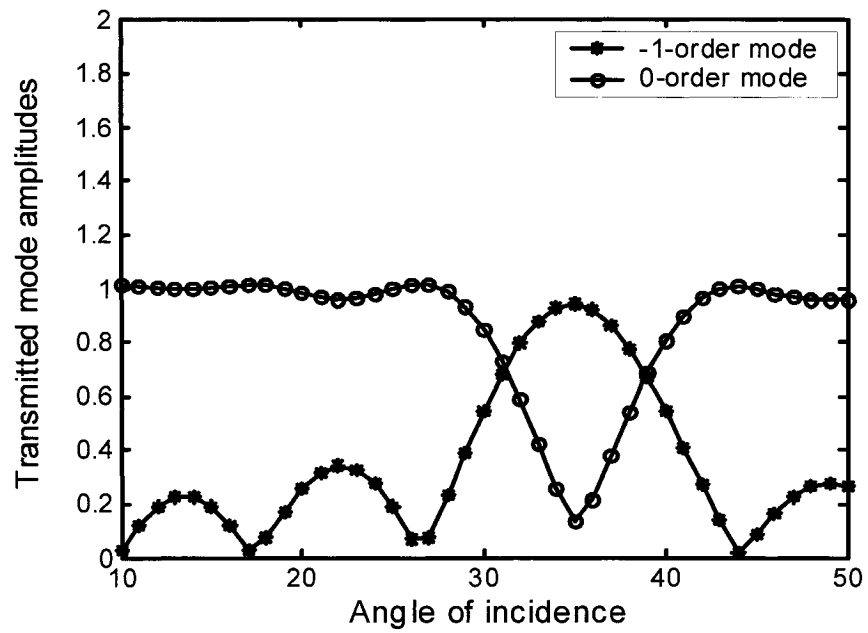

Fig.3-13 Predicted amplitudes of the two transmitted waves for a slanted AMVH with a slant angle of 5.48^0 ($\delta/a = 0.08$).

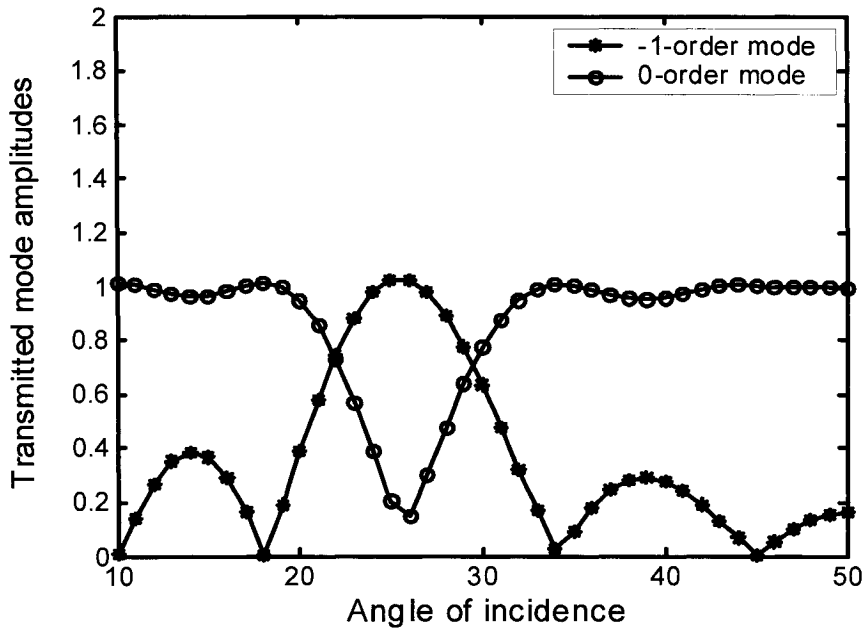

Fig.3.14 Predicted amplitudes of the two transmitted waves for a slanted AMVH with a slant angle of -2.75^0 ($\delta/a = -0.04$).

3.6 Chapter summary and remarks

It has been shown that the self-consistent dynamic-dipole interaction theory (DDIT) presented in this chapter can be used for both TE and TM scattering of AMVHs containing single (or slanted) holographic grating. Since the induced dipoles on different lattice planes have been treated as independent unknowns, the theory also applies to the AMVHs where disk size varies along different layers (z-direction) as well. Such cases will be considered in Chapter 6 where the AMVHs have multiple holographic gratings integrated.

The small-obstacle assumption and the equivalent dipole concept had been widely used in 50s-60s in artificial dielectric [18-20] and in small aperture transmission [44-46]. Collin and Eggimannn [35] had applied this concept to single planar conducting disk lattice of uniform size to calculate the dynamic interaction constant C (see eq.(2-1c)). The latter then can be used in the shunt-susceptance transmission line models for simulating the

propagations (i) through a single planar disk lattice of uniform size as in [20], and (ii) in multiple layered disk lattices of uniform size as recently reported in [59-61]. Our theory also used the concept, but is formulated for multi-layer lattices with disk size varying in both transverse and propagation directions. It can directly predict the propagation and scattering behavior of the multi-layer structures without involving the approximate transmission line models. It is thus more rigorous as it includes all the higher order propagating and evanescent modes.

Chapter 4

Effective medium model of AMVHs and the rigorous coupled-wave theory

An artificial dielectric implemented by embedding a 3D periodical array of uniform obstacles in a host dielectric can be considered as an effective continuous media with an equivalent *homogeneous* permittivity. By analogy to this, an AMVH consisting of periodically distributed *non-uniform* obstacles in a host dielectric can be treated as an effective continuous media with an equivalent *periodically–inhomogeneous* permittivity. The latter's scattering characteristics can, then, be analyzed by using some available theoretical approaches, such as the coupled-wave theory (CWT) [39-42]. Existing methods of predicting effective dielectric properties have been limited to the cases of uniform obstacles (inclusions) [17-20]. In this chapter, first, a method of calculating the effective dielectric modulations of AMVHs is presented, which extends the traditional effective medium theory to model the structures with periodically-varying-size obstacles (inclusions). The rigorous coupled-wave theory is, then, used to analyze the effective medium model of the AMVH presented in the previous chapter.

4.1 Effective dielectric calculation

Consider a single grating, slanted AMVH consisting of N-layer rectangular lattices of conducting disks shown in Fig.4.1. All the parameters and symbols have the same meaning as before (Sec.3.1). The applied electric field can be in the y-direction (perpendicular-polarization) or in the x-direction (parallel-polarization), but for brevity, only perpendicular-polarization case is considered below (Fig.4.1c). The basic assumptions described in Sec.3.1 also hold here.

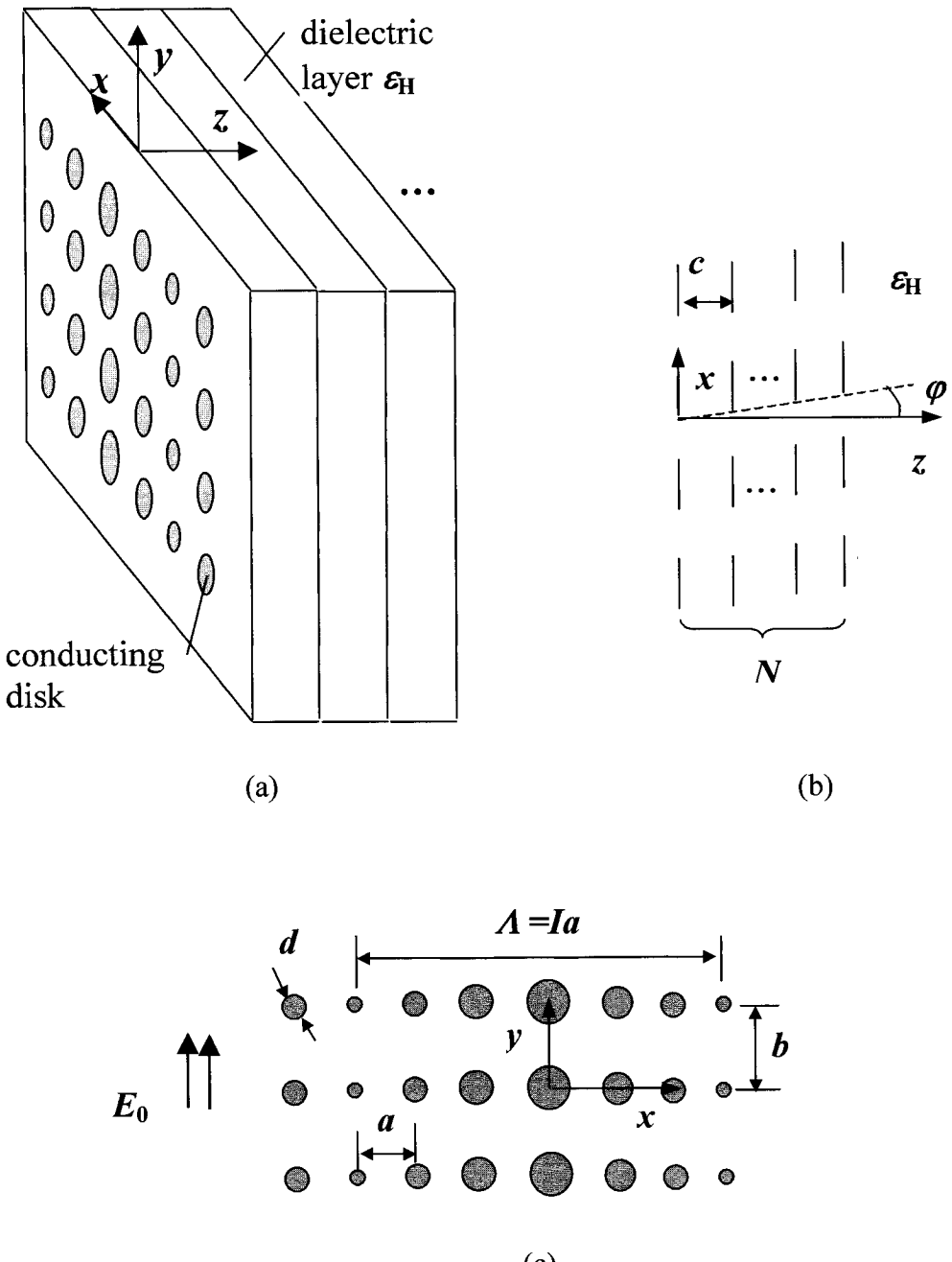

Fig.4.1 (a) An AMVH consisting of N-layer rectangular lattices of conducting disks; (b) side view and the slant angle; (c) front view and dimensions.

The applied E-field will induce a y-directed electric dipole at each disk with its moment being proportional to the total field at the disk center. The total field is the sum of the applied field and the interaction field produced by all the induced dipoles. The induced x-directed dipole at a disk due to the dissimilar sizes of its neighboring disks can be neglected, compared to the y-directed dipole that is parallel to the applied E-field. Because of the symmetry in the y-direction, one only needs to consider a horizontal layer bounded by two conducting planes at $y = \pm b/2$. The problem has also a periodicity in the x-direction with a period of Ia (Fig.4.1c), so we have total of $I \times N$ unknown dipole moments.

Let $p_{ni}, i = 1,\ldots,I,\ n = 1,\ldots,N,$ be the dipole moments of the ith disk in one period located in the nth lattice. The field at the i'th disk's center on the n'th lattice generated by p_{ni} can be written as [20]

$$e^{y}_{n'i',ni} = -\frac{p_{ni}}{\pi b \varepsilon_0 \varepsilon_H} \sum_{k=1}^{\infty} (\frac{2\pi k}{b})^2 K_0(\tfrac{2\pi k}{b} r) \approx \frac{4\pi p_{ni}}{b^3 \varepsilon_0 \varepsilon_H} [K_0(\tfrac{2\pi}{b} r) + 4K_0(\tfrac{4\pi}{b} r)], \qquad (4\text{-}1)$$
$$r = \sqrt{(n'-n)^2 c^2 + [(m'-m)Ia + (i'-i)a + (n'-n)\delta]^2},\ \delta / c = \tan\varphi.$$

where K_0 is the modified Bessel function of second kind, m, m' are the period indices along a disk row, and in the second (approximate) equation we only kept two terms in the summation since K_0 decays exponentially. The total interaction field at the node (i', n') can be obtained from the sum of all the dipoles' fields, except the one located at (i', n').

After some manipulations [20], this total interaction field can be expressed as

$$E^{y}_{n'i'} / E_0 = \frac{1.202}{\pi} \bar{p}_{n'i'} - 4\pi \{ \sum_{n=1}^{N}{}' \sum_{i=1}^{I}{}' \bar{p}_{ni} [K_0(\tfrac{2\pi}{b} r_0) + 4K_0(\tfrac{4\pi}{b} r_0)] +$$
$$\sum_{n=1}^{N} \sum_{i=1}^{I} \bar{p}_{ni} \sum_{m=1}^{\infty} [K_0(\tfrac{2\pi}{b} r_m) + 4K_0(\tfrac{4\pi}{b} r_m) + K_0(\tfrac{2\pi}{b} r_{-m}) + 4K_0(\tfrac{4\pi}{b} r_{-m})]. \qquad (4\text{-}2)$$
$$\bar{p}_{n'i'} \equiv p_{n'i'} / (\varepsilon_0 \varepsilon_H b^3 E_0),\quad i = 1,\ldots,I,\ n = 1,\ldots,N,$$
$$r_{\pm m} = \sqrt{(n'-n)^2 c^2 + [\pm mIa + (i'-i)a + (n'-n)\delta]^2},\ m = 0,1,\cdots.$$

where the sum $\Sigma'\Sigma'$ excludes the term of (i, n) = (i', n'). From the linear relation of the induced dipole moment and the total field

$$p_{ni} = \alpha_i \varepsilon_0 \varepsilon_H (E_0 + E^{y}_{ni}) \qquad (4\text{-}3)$$

in which the proportional constant $\alpha_i = \frac{2}{3} d_i^3$ is the electric polarizability of the ith disk [15], we have

$$\begin{aligned} \frac{b^3}{\alpha_i} \bar{p}_{n'i'} &= 1 + \frac{1.201}{\pi} \bar{p}_{n'i'} - 4\pi \sum_{n=1}^{N} \sum_{i=1}^{I} B_{n'i',ni} \bar{p}_{ni} \\ B_{n'i',ni} &= [K_0(\tfrac{2\pi}{b} r_0) + 4K_0(\tfrac{4\pi}{b} r_0)]\Big|_{r_0 \neq 0} + \\ &\sum_{m=1}^{\infty} [K_0(\tfrac{2\pi}{b} r_m) + 4K_0(\tfrac{4\pi}{b} r_m) + K_0(\tfrac{2\pi}{b} r_{-m}) + 4K_0(\tfrac{4\pi}{b} r_{-m})]. \end{aligned} \tag{4-4}$$

By definition of the effective permittivity [20], we have

$$\begin{aligned} D^y_{a,ni} &= \varepsilon_0 \varepsilon_H E^y_{a,ni} + M p^y_{ni} = \varepsilon_0 \varepsilon_{r,ni} E^y_{a,ni}, \\ \varepsilon_{r,ni} &= \varepsilon_H + \frac{M p^y_{ni}}{\varepsilon_0 E^y_{a,ni}} \cong \varepsilon_H + \frac{b^2 p^y_{ni}}{ac \varepsilon_0 E^y_0} = \varepsilon_H (1 + \frac{b^2}{ac} \bar{p}^y_{ni}) \end{aligned} \tag{4-5a,b}$$

where M is the number of disks per unit volume which is equal to $1/(abc)$, and $\varepsilon_{r,ni}$ the averaged values of the effective relative dielectric at lattice nodes. For a given AMVH (known α_i), p_{ni} can be solved in (4-4) and the effective modulated dielectric constant is thus obtained from (4-5). On the other hand, given a desired dielectric grating (known $\varepsilon_{r,ni}$), p_{ni} can be calculated from (4-5) (assuming the lattice constants a,b,c), the polarizability and thus the disk diameters can be determined by (4-4). Equations (4-4,5) are, therefore, an extension of the Clausius-Mosotti theory to include non-uniform obstacles in artificial dielectric structures. In practical calculation, the series in the 2nd equation of (4-4) is found convergent quite fast (truncated at m=5), and use has been made of the fact that $B_{n'i',ni}$ depends only on the differences n'-n and i'-i, which significantly reduces the computing time.

4.2 Numerical examples

Considering a volume hologram with following parameters and dimensions,

$a = b = 0.6$ mm, c $= 0.5$ mm, $I = 10$, $N = 81$, $\varepsilon_H = 3.0$,

$\mathrm{d}_{1\text{-}11} = [0.26, 0.289, 0.345, 0.393, 0.424, 0.434, 0.424, 0.393, 0.345, 0.289, 0.26]$.

Figure 4.2 shows the calculated effective dielectric distribution using the proposed formula (4-4)-(4-5), as well as the results using the table lookup method based on the formula in [16] (Eq.(14), c/a > 0.6). As is seen, the difference between the two results is obvious when *c/a* is close to 0.6. It is also seen that as *c/a* decreases the effective dielectric distribution on the edge layer deviates slightly from that on the middle layer, due to the finite array effect in the thickness (*z*) direction. The second example is to design the disk diameters of a volume hologram with following parameters and desired dielectric grating, which has been used in [12],

$$N = 81, I = 10,\ a = b = 0.6\,\text{mm},\ \varepsilon_H = 3.0,\ \varepsilon_r = 3.6 + 0.1\sin(\frac{2\pi}{aI}x + x_0).$$

The predicted disk diameters are shown in Fig.4.3, along with the results by using the table lookup method based on the formula in [19]. As is seen, using the table lookup method results in slightly small disk diameters.

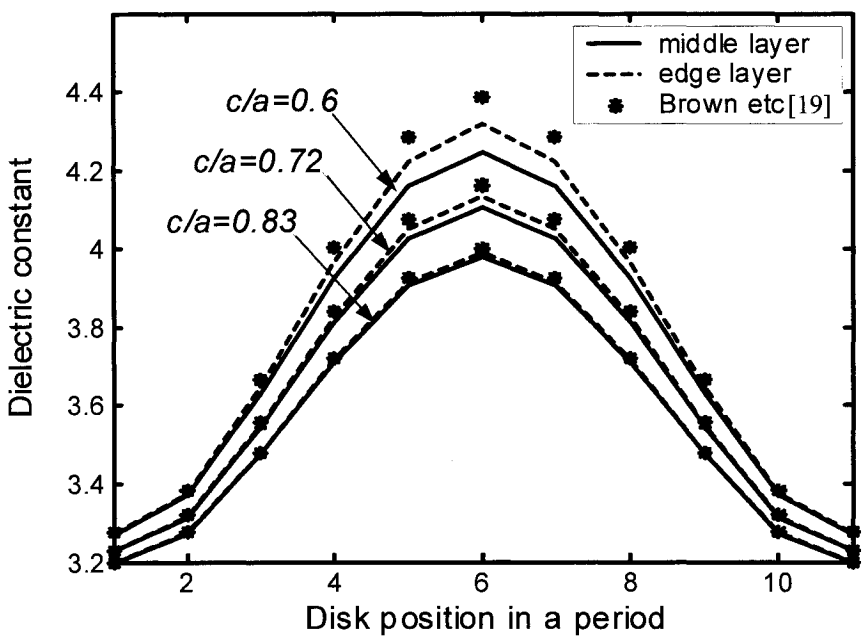

Fig.4.2 Calculated effective dielectric constant at the lattice nodes in one grating period of the structure for three different *c/a* ratios.

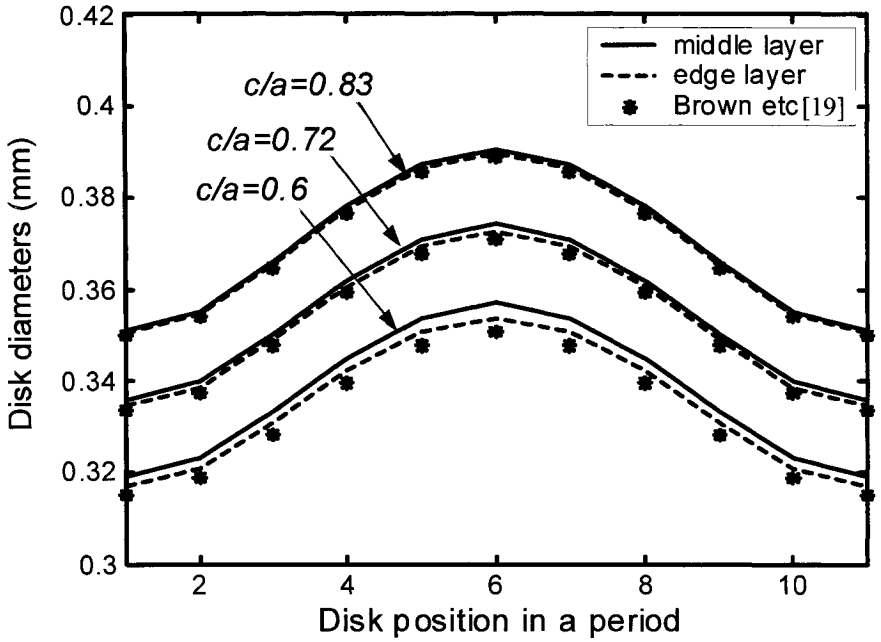

Fig.4.3 Designed disk diameters at the lattice nodes in one grating period of the structure for three different *c/a* ratios.

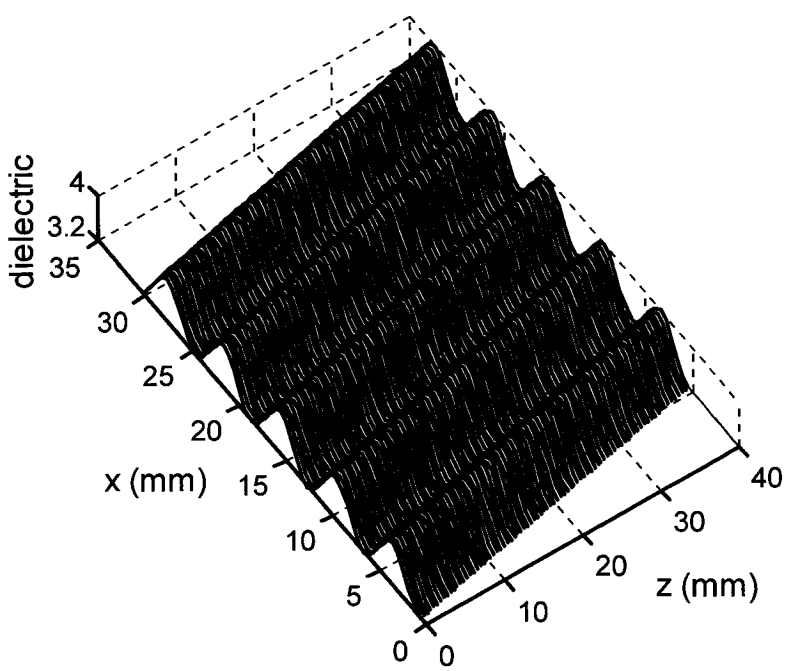

Fig.4.4 Calculated effective dielectric distribution for a slanted volume hologram ($\varphi = 6.8^{o}$).

Finally, figure 4.4 gives a 3-D plot of the calculated effective dielectric distribution for a slanted volume hologram with the same parameters as in the first example (c=0.5mm, δ=0.06mm), and a slant angle of $\varphi = \tan^{-1}(0.12) = 6.8^{\circ}$.

4.3 The coupled-wave modeling

Once the equivalency between a discrete disk lattice model and a continuous dielectric grating has been established, the coupled-wave theory [39,40] can be applied to obtain the scattering characteristics of the continuous model. It would be interesting to compare the results from the dynamic-dipole-interaction theory proposed in this thesis based on the actual disk lattice structure to those from the coupled-wave theory based on the effective medium model.

Let us consider a 1D sinusoidal dielectric slab grating as shown in Fig.4.5, which is an equivalent of the single grating AMVH introduced in Sec.3.1 (Fig.3.1). The effective continuous variation in the relative permittivity is given by

$$\varepsilon_2(x,z) = \varepsilon_2[1 + \Delta\varepsilon\cos(2\pi x / Ia)] \tag{4-6}$$

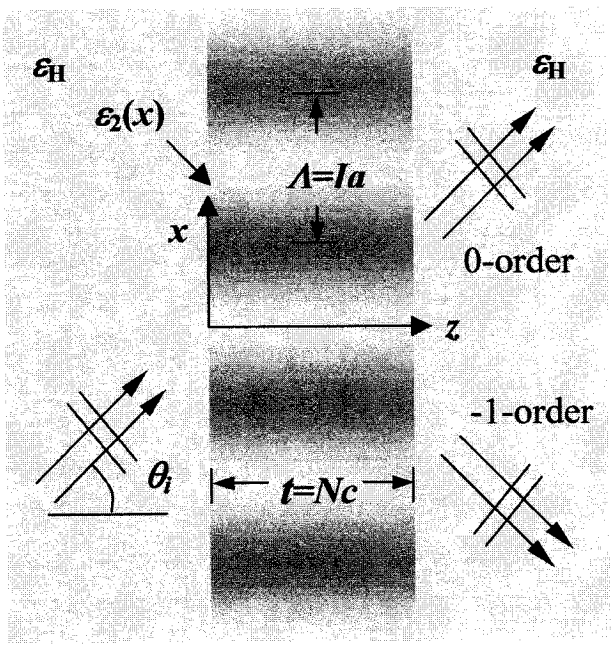

Fig.4.5 The equivalent continuous slab grating embedded in a homogeneous host dielectric.

With a TE (perpendicular-polarization) plane wave incidence, the wave equation is given by

$$\{\nabla^2 + k_2^2[1 + \Delta\varepsilon\cos(2\pi x / Ia)]\}E^y(x,z) = 0, \quad k_2^2 = \omega^2\mu_0\varepsilon_0\varepsilon_2 \tag{4-7}$$

Using the modal expansion method [40], the solution to (4-7) can be expressed as

$$E^y(x,z) = \sum_{n=-\infty}^{\infty} f_n(z)\exp(-jk_{nx}x), \quad k_{nx} = k_2\sin\theta_i + \frac{2\pi n}{Ia} \tag{4-8}$$

Substituting (4-8) into (4-7) and arranging the resulting series in a modal expansion form, we then have

$$\frac{d^2 f_n(z)}{dz^2} + (k_2^2 - k_{nx}^2)f_n(z) + \frac{k_2^2\Delta\varepsilon}{2}[f_{n-1}(z) + f_{n+1}(z)] = 0, \quad n = 0, \pm 1, \pm 2, \cdots \tag{4-9}$$

For the parameters and frequency used in the numerical calculation in the next section, there exist only two scattered propagation modes (m=0, −1) from the periodic structure. We thus keep only these two modes in (4-9), which then becomes

$$\begin{aligned} &\frac{d^2 f_0(z)}{dz^2} + (k_2^2 - k_{0x}^2)f_0(z) + \frac{k_2^2\Delta\varepsilon}{2}f_{-1}(z) = 0, \\ &\frac{d^2 f_{-1}(z)}{dz^2} + (k_2^2 - k_{-1x}^2)f_{-1}(z) + \frac{k_2^2\Delta\varepsilon}{2}f_0(z) = 0, \end{aligned} \tag{4-10}$$

Equation (4-10) is a two-wave second-order system that needs to be solved in connection with the solutions in the neighboring regions in both sides of the slab grating. The solution to (4-10) that satisfies all boundary conditions is given in Appendix B and will be used in the next section for numerical comparisons. The solution for the TM case (parallel-polarization) can be derived in a similar way, but the numerical calculation could be more tedious since the effective dielectric modulation now depends on the angle of incidence.

4.4 Numerical results and comparisons

First, consider the AMVH used as the first example in Sec.3.4. The parameters are duplicated here: c = 0.5mm, a = b = 0.6mm, ε_H = 3.0, I = 10, N = 81 and f = 30GHz. The disk diameters in one period are [0.26 0.289 0.345 0.393 0.424 0.434 0.424 0.393 0.345 0.289] (mm).

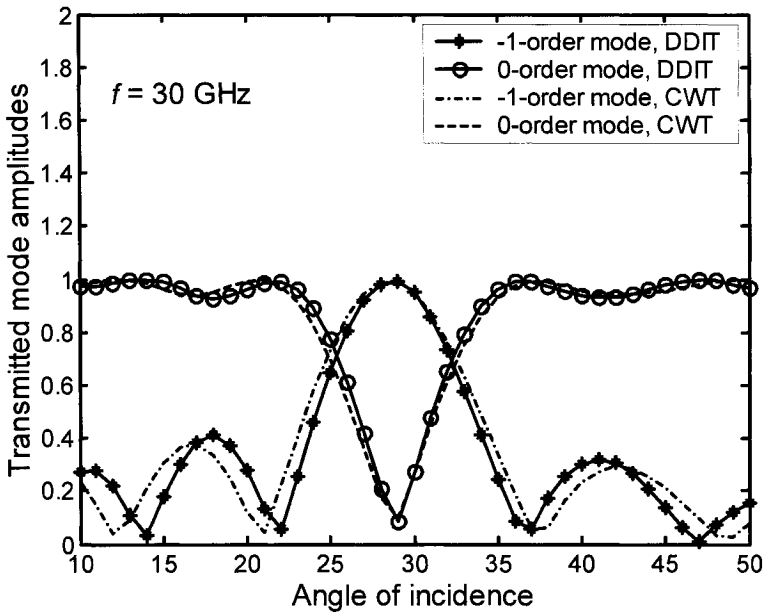

(a) Transmitted modes

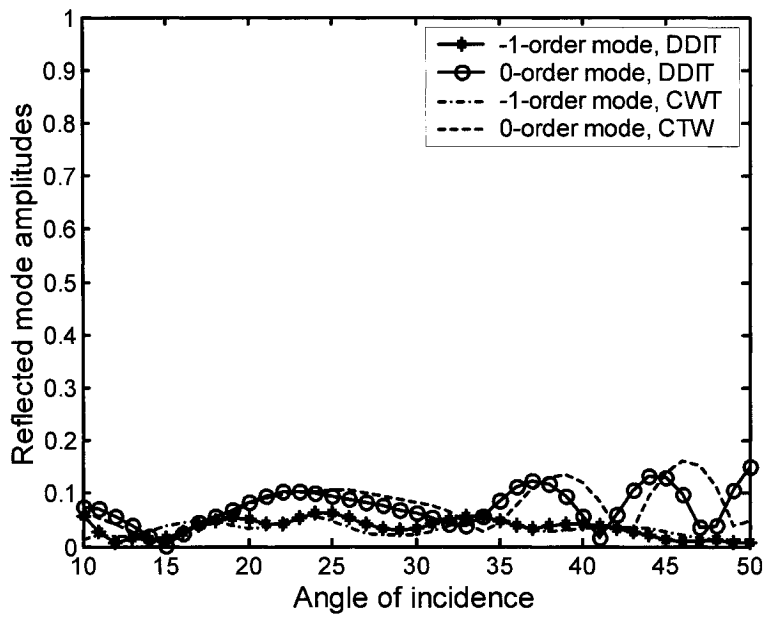

(b) Reflected modes

Fig.4.6 Comparison on predicted mode amplitudes of the (a) transmitted and (b) reflected waves, for the first example in Sec.3.4.

Use of the method presented in Sec.4.1 generates the effective permittivity modulation as

$$\varepsilon_{er}(i) = 3.6 + 0.4\cos[2\pi(i-1)/10] \tag{4-11}$$

Simulated results on transmitted wave modes using the coupled-wave theory (CWT) and the dynamic-dipole-interaction-theory (DDIT) are plotted in Fig.4.6a. In the DDIT calculation, the magnetic dipoles' contribution is included. A good agreement has been observed for the two methods, particularly near the Bragg angle (29^0). Result comparison on reflected wave modes is given in Fig.4.6b, which also shows the close results between the two methods.

Next, consider the 2nd AMVH example in Sec.3.4. The parameters are duplicated here: c = 0.5mm, a = b = 0.62mm, ε_H = 3.0, I = 12, N = 91 and f = 30GHz. The disk diameters in one period are [0.268 0.29 0.336 0.383 0.419 0.442 0.45 0.442 0.419 0.383 0.336 0.29 0.268] (mm). Its effective permittivity modulation is predicted as

$$\varepsilon_{er}(i) = 3.6 + 0.4\cos[2\pi(i-1)/12] \tag{4-12}$$

The results from the two methods are compared and shown in Figs.4.7a,b, for the transmission and reflection waves, respectively. Also, good agreement has been obtained, specifically at the Bragg angle (22.7^0 in this case). In fact, previous studies [40] have shown that the coupled-wave-theory produces more accurate results when incidence angle is close to the Bragg angle.

4.5 Chapter summary and remarks

It has been demonstrated that for a single-grating AMVH (unslanted) with a given effective permittivity modulation, the coupled-wave theory can provide quite accurate predictions, and can be quickly evaluated compared to the DDIT, as it has an analytical solution. However, for multiple-grating or slanted grating AMVHs, the effective permittivity modulations are not simple 1D functions, and the resulting differential equation systems will have non-constant coefficients, which, in general, need to be solved numerically.

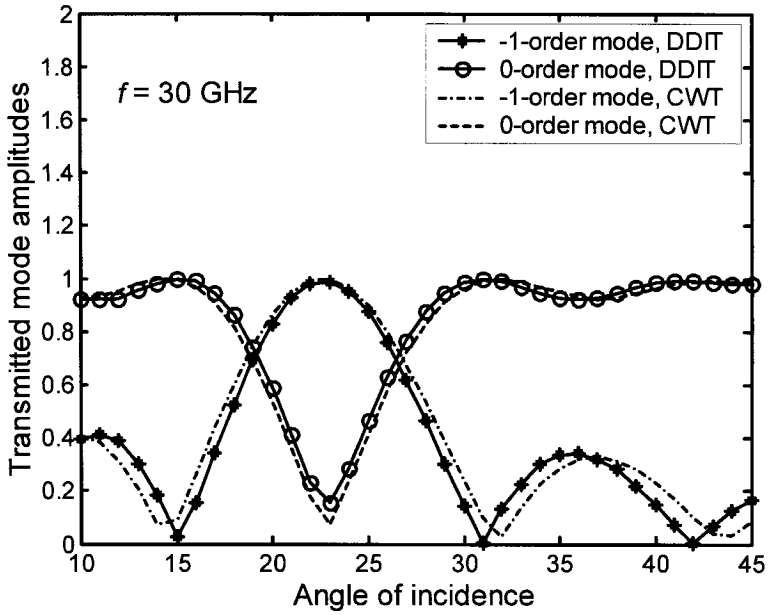

(a) Transmitted modes

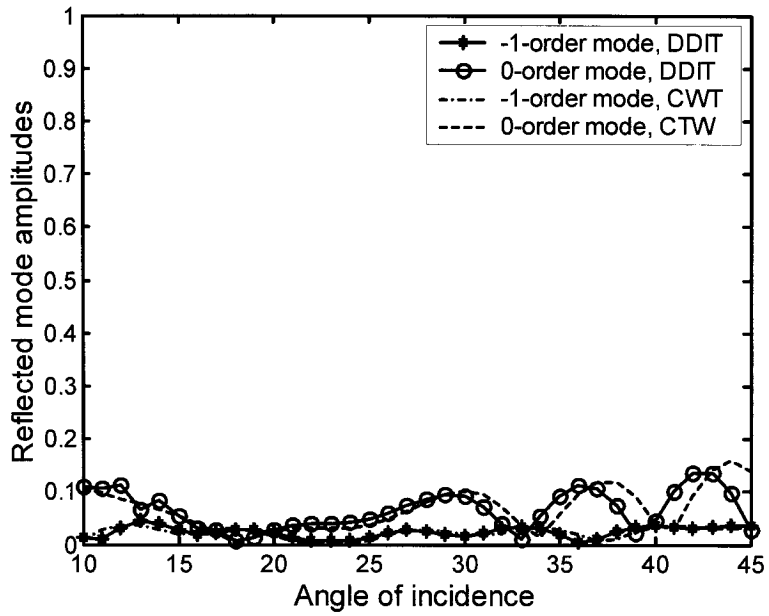

(b) Reflected modes

Fig.4.7 Comparison on predicted mode amplitudes of the (a) transmitted and (b) reflected waves, for the second example in Sec.3.4.

Furthermore, for design optimization of AMVHs, each time the parameters being updated, the effective permittivity modulation has to be recalculated using the above procedure (Sec.4.1) before the CWT analysis can be applied; whereas, the DDIT works directly on the actual AMVH structures.

It should be noted that there exist various versions of the coupled-wave/mode theory based on different approximations and assumptions during the long research history of grating diffraction [40]. The one used here is a more general and rigorous method proposed by Moharam and Gaylord [41]. We have also tried Kogelnik's coupled-wave theory [39] where the second-order derivative is neglected, but the result shows a remarkable discrepancy from the rigorous theory as well as from our method (DDIT), and is therefore not presented here.

The last but not the least note to be mentioned before ending this chapter is that the equivalence between an AMVH and its effective medium model is not a one-to-one map, i.e., there can be more than one AMVH that have the same effective medium model.

Chapter 5

Parametric analysis, optimized patch design, and potential applications of single-grating AMVHs

There are many parameters involved in the design of artificial microwave volume holograms, which may have different effects on their scattering characteristics and performance. It is of importance to carry out a parametric study in order to obtain an optimization design for a specific application. The parameters used in AMVHs can be divided into two categories, (i) those related with the lattice structures and constants, such as disk spacing a, b, lattice layer thickness c, and the number of lattice layers; (ii) those related with metallic patches, such as shapes and sizes, and the property (ε_H) dielectric substrates. Since artificial microwave volume hologram is a new concept and research direction, its merits and application potentials in microwave engineering and antenna areas still need to be explored. Nevertheless, some possible applications of AMVHs will be discussed in this chapter.

5.1 Effect of lattice constants *c*, *b* and the number of layers

First, consider the effect of the lattice layer thickness c. One interesting feature is that the angular window, where the incident beam energy is mostly coupled into the diffraction (-1-order) beam, can be scaled by varying the lattice layer thickness c. Figures 5.1a and 5.1b show the recalculated transmitted mode amplitudes for the 1st example given in Sec.4.4 for the layer thickness c = 1.0mm and c = 1.5mm, respectively. Comparing Figs.5.1a,b to Fig.4.6a, one can see that the angular window is compressed as the layer thickness c increases. A similar phenomenon has been observed in [43] for stratified volume holographic optical elements. It is also seen that increasing the lattice layer thickness has actually decreased the maximum coupling efficiency between the two modes.

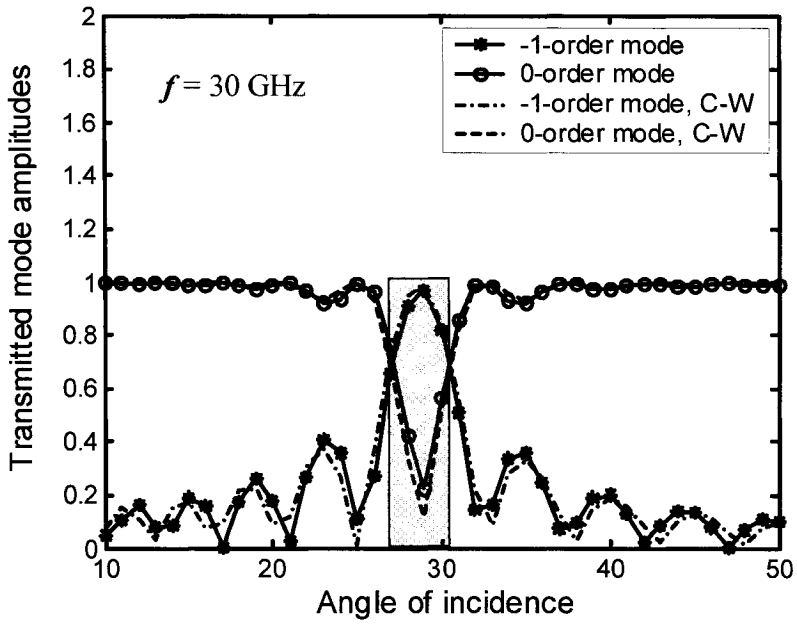

(a)

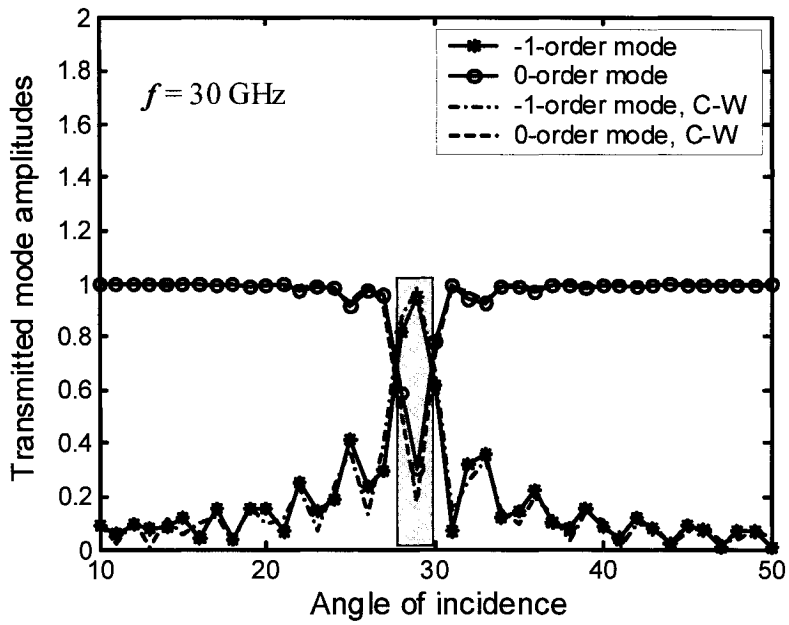

(b)

Fig.5.1 Predicted amplitudes of the two transmitted waves with updated the lattice layer thickness, (a) c=1.0mm, and (b) c=1.5mm.

The results from the coupled-mode theory are also plotted in the same figures for comparison. It should be mentioned that when the lattice layer thickness varies, the effective dielectric modulation is changed accordingly, though the disk sizes remain the same. Therefore, for the parametric study or design optimization of an AMVH using the coupled-wave theory, the effective medium model, e.g., Eqs. (4-4, 4-5), needs to be recalculated each time the hologram is adjusted and before the theory can be applied. In contrast to this, the dynamic-dipole-interaction theory developed in this thesis work is basically a parametric approach that works directly on the original disk media. On the other hand, as stated at the end of chapter 4, since one can design many AMVHs with different parameters but equivalent to the same effective medium model and therefore having the same output for a given incidence, by calculating the effective medium model one can judge if the changes made on an AMVH could result in a different output.

Next, let's vary the lattice parameter b, while keep all other parameters the same. Comparison of results for b = 0.6, 0.8, 1.0mm, respectively, is shown in Fig.5.2. It is obvious that the diffraction effect decreases as b increases, since a larger b corresponds a lower effective permittivity modulation.

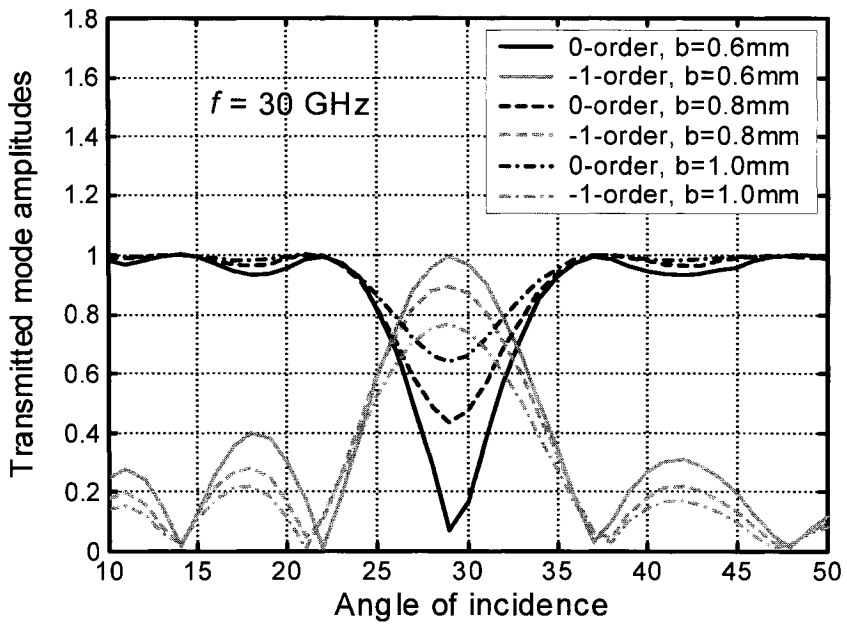

Fig.5.2 Results for different values of the lattice constant b, for the 1st example in Sec.4.4

Finally, consider the effect of the number of planar lattice layers. By adding or reducing some lattice layers of an AMVH, while keeping all the other parameters unchanged, the effective dielectric modulation basically remains the same except for the total thickness varying accordingly. Figure 5.3 show the transmitted mode amplitudes versus the number of layers at the Bragg angle incidence. As seen, there are special numbers of layers where the diffraction mode (-1-order) reaches its maximum. It seems that both transmitted mode amplitudes are periodic functions of the total thickness for Bragg angle incidence. This relationship is useful on choosing the number of lattice layers when design AMVHs.

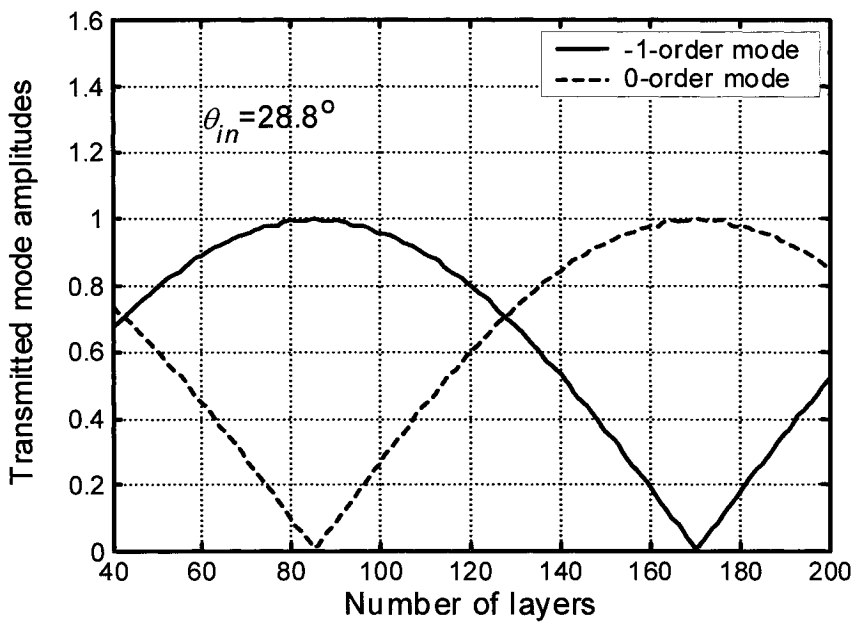

Fig. 5.3 Transmitted mode amplitudes versus number of layers at Bragg angle incidence with the layer thickness c = 0.5mm, and f = 30GHz.

5.2 Effect of metallic patch geometry

As we have seen, the modulation of the host dielectric constant in an AMVH relies on the polarization capability of the conducting patches used in the AMVH. This capability is quantitatively characterized by the patch's electric polarizability [44-47]. By examining the electric polarizability of different patch geometries under an applied *E*-field, one may find a patch shape that has a higher ratio of polarizability over patch area.

An intuitive thought on how to select patch shape is the following. The electric polarization of a charge distribution depends on the charge's amplitudes as well as the charge's locations (or distances between opposite charges). By placing large charges of opposite signs far apart in a patch, one can anticipate a large electric polarization value. Since large charge density appears near the patch edges, it is wise to design patch edges as far as possible from the patch center. For example, consider a circular patch versus a rectangular patch as shown in Fig.5.4. If the two patches have the same size (*d*), then the square patch more likely yields larger electric polarization than the circular one when placed in an electric field, since the former has more edge portion (top and bottom) with longer distances between them than the latter.

In the following, a numerical procedure based on the method of moments will be carried out to quantitatively predict the electric polarizability of a square patch, and therefore to prove this conjecture.

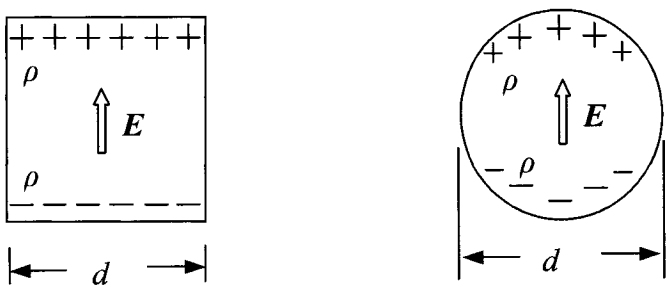

Fig. 5.4 Charge distributions on different patch shapes and their contributions to polarization.

5.2.1 Method of moments (MoM)

Consider a planar conducting patch of arbitrary shape located in the x-y plane, as shown in Fig. 5.5a. A homogeneous electric field E_0 is applied along the y-direction. The corresponding aperture problems have been studied previously by using numerical procedures, such as the method of moments [48]. The electric potential on the patch surface should be a constant, and can be expressed as the sum of the applied potential field and the potential due to the induced charge density on the surface:

$$V_{tot}(|\mathbf{r}|) = V_{app}(|\mathbf{r}|) + V_{ind}(|\mathbf{r}|) = const., \quad \mathbf{r} \in \Omega \tag{5-1}$$

where,

$$V_{app} = V_0 - E_0 y, \quad V_{ind} = \frac{1}{4\pi\varepsilon} \iint_{\Omega} \frac{\rho(\mathbf{r})}{|\mathbf{r}'-\mathbf{r}|} dS', \text{ with } V_{ind}(|\mathbf{r}| \to \infty) \to 0. \tag{5-2a,b}$$

By choosing the arbitrary reference V_0, from (5-1) we can always have

$$\frac{1}{4\pi\varepsilon} \iint_{\Omega} \frac{\rho(\mathbf{r})}{|\mathbf{r}'-\mathbf{r}|} dS' - E_0 y = 0, \quad \text{or,} \quad \frac{1}{4\pi\varepsilon} \iint_{\Omega} \frac{\rho(\mathbf{r})}{|\mathbf{r}'-\mathbf{r}|} dS' = E_0 y. \tag{5-3}$$

Equation (5-3) is an integral equation for the charge density, which includes the induced charge on both sides of the patch (due to the symmetry, charges on both sides are equal).

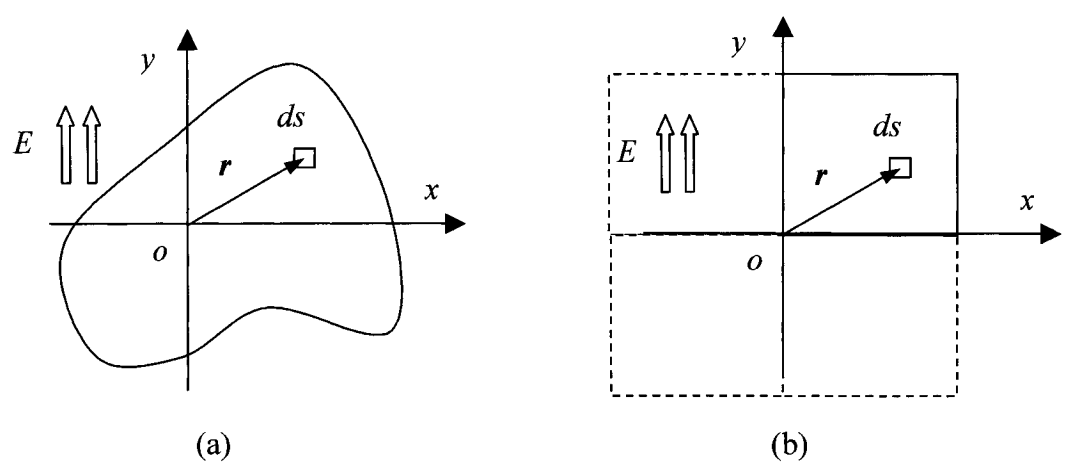

Fig.5.5 (a) Electric static problem: a arbitrary planar conducting patch in a homogeneous E-field; (b) a quarter of a square conducting patch.

The y-directed component of the total polarization vector can be written as

$$P_y = \iint_{\Omega} \rho(\mathbf{r}) y dS', \tag{5-4}$$

From (5-4) and following the definition of electric polarizability,

$$P = \alpha_e \varepsilon E \tag{5-5}$$

we have

$$\alpha_e = 4\pi \iint_{\Omega} \frac{\rho(\mathbf{r})}{4\pi\varepsilon E_0} y dS' = 4\pi \iint_{\Omega} \bar{\rho}(\mathbf{r}) y dS', \tag{5-6}$$
where $\bar{\rho} = \rho / 4\pi\varepsilon E_0$.

With the dimensionless charge density $\bar{\rho}$ defined in (5-6), the integral equation (5-3) can be rewritten as

$$\iint_{\Omega} \frac{\bar{\rho}(\mathbf{r})}{|\mathbf{r}'-\mathbf{r}|} dS' = y, \quad \mathbf{r} \in \Omega \tag{5-7}$$

In the MoM calculation, the patch region is meshed into triangular subdomains and the unknown charge density is interpolated by piece-wise constant charge densities defined at the centers of triangle elements. Let $\bar{\rho}_n$ the constant charge density defined on the nth triangle element Ω_n, the discretization of Eqs.(5-7) and (5-6) gives

$$\sum_{n=1}^{N} \bar{\rho}_n \iint_{\Omega_n} \frac{dS'}{|\mathbf{r}'-\mathbf{r}_m|} = y_m, \quad m = 1, \cdots, N. \tag{5-8}$$

$$\alpha_e = 4\pi \sum_{n=1}^{N} \bar{\rho}_n y_n \Delta S_n, \tag{5-9}$$

Here, we actually used the Dirac delta functions as the weighting functions (point-matching [49]). Linear equation system (5-8) can be solved in the usual way. For the diagonal elements ($m = n$) of the system matrix, the integral in (5-8) can be completed explicitly, and therefore, there is no need for special treatment of the singularity of numerical integration. The analytic expression is given in Appendix C. In most cases, the patches to be considered have certain geometrical symmetries, and by taking advantage of

the problem's symmetries, only a half or a quarter of original area need to be involved in the calculation. Figure 5.5b shows a quarter of a square patch that is involved in the MoM calculation, since the problem is symmetrical about y-axis and anti-symmetrical about the x-axis.

5.2.2 Numerical results on square and circular patches

Both a square patch and a disk patch are considered in the numerical calculation of polarizability, and the latter serves as a benchmark to exam the correctness and accuracy of the algorithm since analytic result exists for disk patches (Eq.(3.16a)). Figures 5.6a and 5.6b show the typical meshes of the square and disk patches, respectively, where the dots represent the centers of the triangles. The calculated polarizability for disk patch is shown in the following Table 5.1 for different numbers of triangle elements used. As it is seen, the numerical result does converge to the exact value, though the converging speed is not that fast. This is because of the use of the constant element. It is expected that use of high order elements could improve the convergence rate.

Table 5.1. Computed polarizability for disk patch.

Disk patch (d=0.4mm, constant triangle element)		
Nodes	Elements	Polarizability
153	256	0.03922
231	400	0.03959
561	1024	0.04014
1281	2400	0.04121
Theoretical value ($(\alpha_e = \frac{2}{3}d^3)$)		0.04267

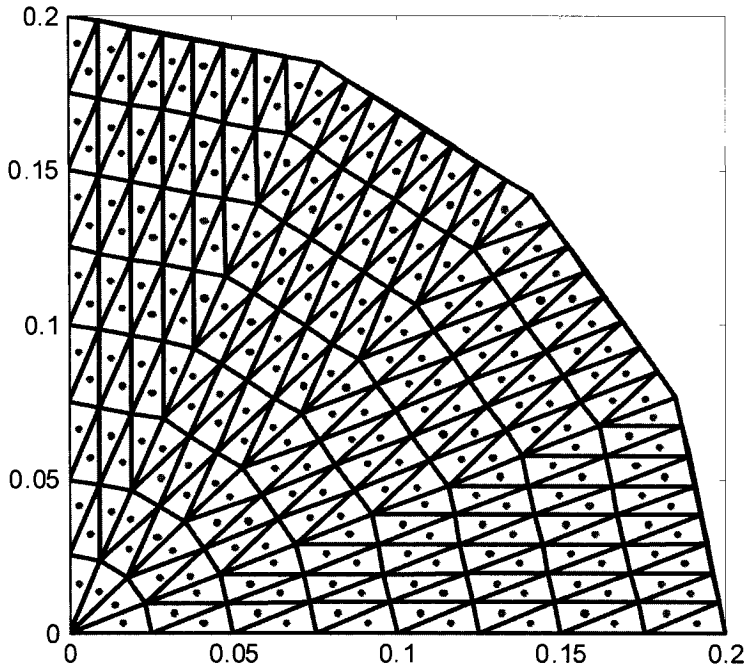

(a)

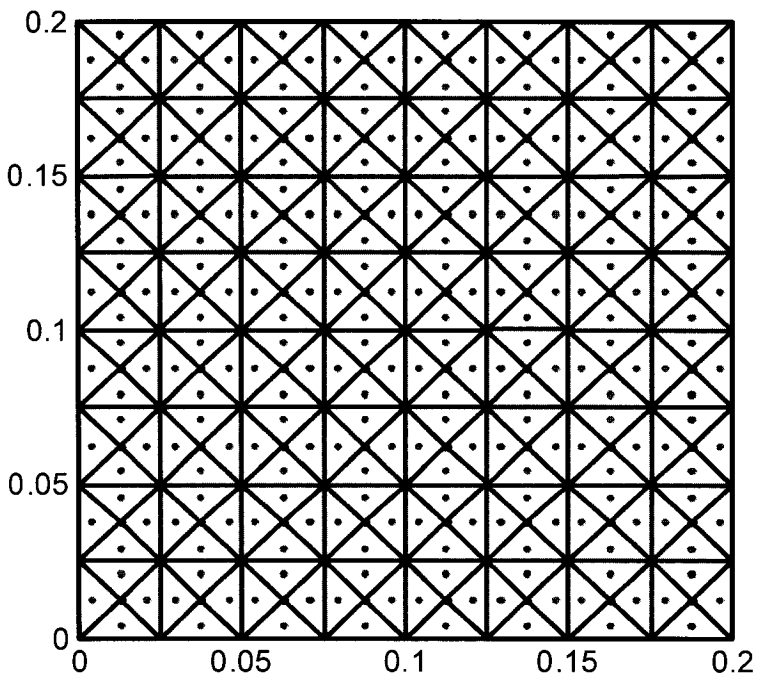

(b)

Fig.5.6 Typical meshes for a quarter of (a) a disk and (b) a square patch; dots: centers of the triangles.

Based on the disk patch results, we calculate the square patch's polarizability using the same constant triangle element (1024 elements employed), and the results are given in Fig.5.7. For comparison, the disk patch's polarizabilities (analytic values) are also plotted in the same figure.

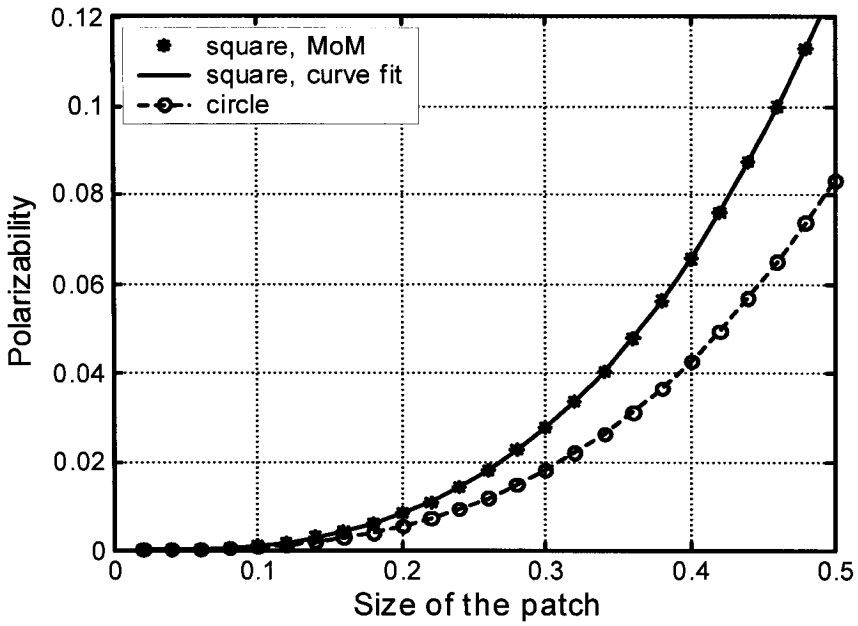

Fig.5.7 Computed electric polarizability vs. patch size for the square patch geometry.

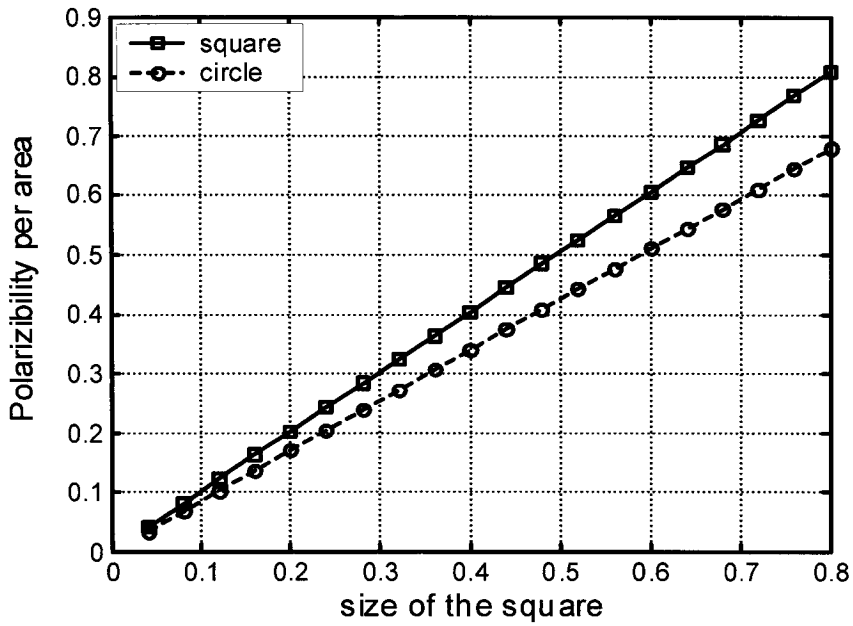

Fig.5.8 Electric polarizability per area for the square and disk patches.

About 50% increase on polarizability is observed for a square patch in comparison with a disk patch of same size (0.06557 vs 0.04267 for d=0.4mm). One of the benefits of using high polarizability patches is it results in fewer lattice layers. Since discrete numerical data are not convenient to use in the design of AMVHs, a curve fitting has been done to represent the relation analytically. By analogy with the disk patch, a cubic power function relationship is anticipated, and this function is finally determined as

$$\alpha_e = 1.02456 d^3 \tag{5-10}$$

The cubic curve represented by (5-10) is also plotted in Fig. 5.7 (solid line), and is seen in perfect fit with the numerical data. Figure 5.8 shows the average polarizibilities produced per unit area (α_e/S) from square and disk patch geometries. Square geometry yields about 20% higher α_e/S ratio than disk geometry.

The computed charge density distributions are given in Figs.5.9a and 5.9b for the disk and square patches, respectively. It shows that large charge density values are distributed near the edges (or edge portion) far from the horizontal symmetrical axis (x-axis), which also validates the conjecture depicted in Fig.5.4.

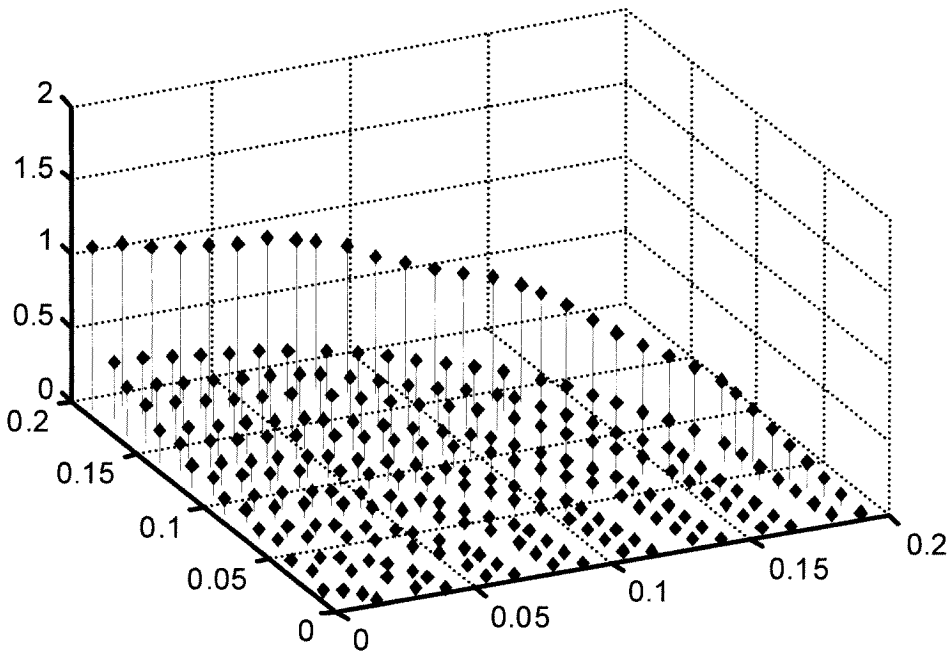

(a)

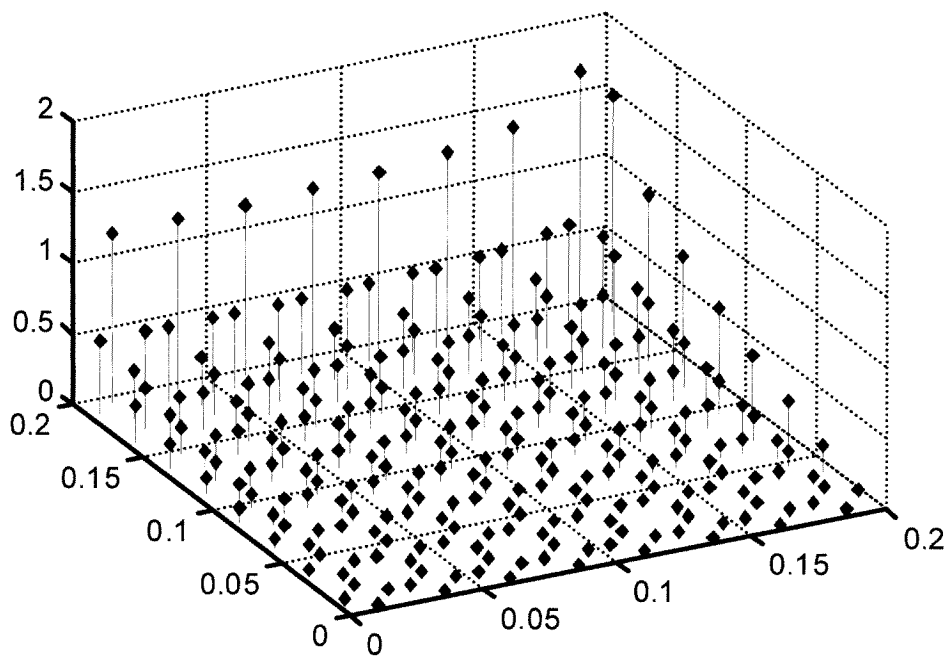

(b)

Fig.5.9 Computed charge density at the element centers in one quarter of (a) a disk patch, and (b) a square patch.

5.3 Possible applications of single-grating AMVHs

Before discussing the potential applications, let us take a look at the frequency response of AMVHs. Since the Bragg condition for a grating structure relates the angle of incidence to the frequency, it is possible to convert the angular window to a frequency window in Figures 5.1a,b. The range of the frequency scan is selected in such a way so that there exist only two propagating Floquet modes in the scattered field. Figure 5.10 shows the mode amplitudes of two transmitted waves versus frequency at a fixed incident angle of 29^0. As seen, the frequency response is quite similar to those incident angle responses (say, Fig.3.7a). The directly transmitted mode (0-order) vanishes at about f = 30GHz, the Bragg frequency, where the diffracted mode (−1-order) reaches its maximum. Again, by varying the thickness of the lattice layer, the frequency window can be scaled as well (see Sec.5.1).

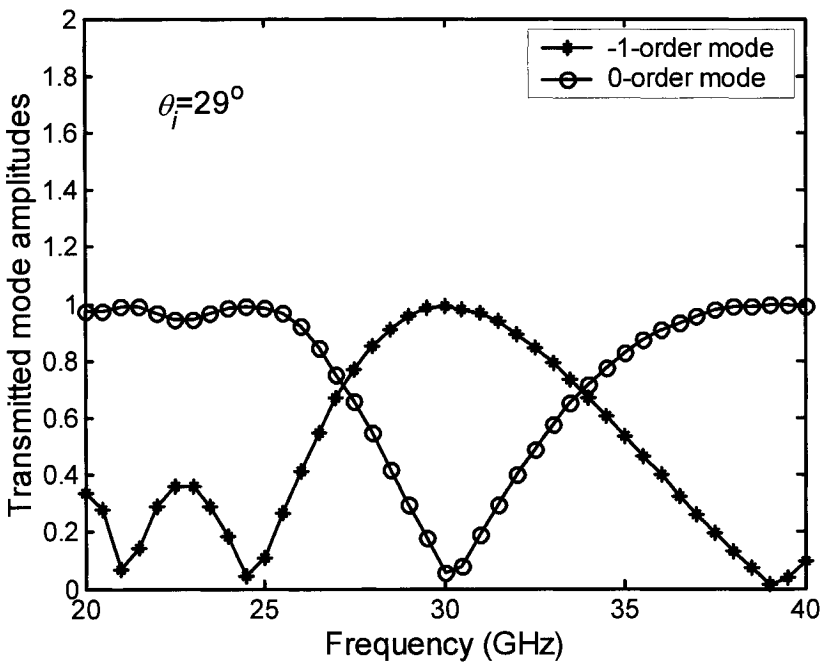

Fig.5.10 Mode amplitudes of the two transmitted waves versus frequency.

Based on the knowledge of single-grating AMVHs described from Chapter 3 through Chapter 5, we can depict some of their possible applications as in Fig.5.11. The first picture (Fig.5.11a) shows a dual-beam antenna application, where the incident beam from a feed can be divided into two beams at an arbitrary ratio and redirect them into the free space in two arbitrary directions. The ratio adjustment can be done by varying the angle of incidence; while the required output directions can be realized by simply using them as the recording beams' directions during the AMVH design. The extension of this configuration is a dual-beam, dual-band antenna as shown in Fig.5.11b. It uses the function shown in Fig.5.10 (Bragg frequency) to separate the beams of different frequencies by routing them to different directions (we may call it frequency-enabled beam routing). In a similar manner, one can design an antenna with certain direction diversity as shown Fig.5.11c. At the Bragg angle, an incoming beam is redirected to a specific direction, while at other angles, it directly passes through the AMVH (we may call it angle-enabled beam routing). Compared to phased array antennas, such angle and frequency discrimination functions are implemented here with passive AMVH devices, whereas the former usually use many active devices. A more powerful feature of AMVHs is the wave-front modification. Fig.5.11d shows a typical such application as a beam focusing lens, where the hologram is recorded according to the interference pattern of a plane wave and a spherical wave. In terms of frequency and angular filtering, unlike FSS (frequency selective surface) frequency filters and conventional spatial filters, AMVHs basically do not reflect the un-wanted beams (not accounting for the reflection from air-dielectric interfaces), but instead, route them to other directions in the transmission side. Therefore, their scattering cross-sections are very small. Those are the basic application patterns. By grouping or cascading several AMVHs, one could realize more useful application designs.

It should be mentioned that the single-grating AMVHs we have discussed so far are merely the simplest, most basic type of AMVHs in the beginning/intermediate stage of the long journey of developing novel and practical AMVH devices for advanced antenna and microwave applications. Although there may not be many direct applications for them, study of this type of simple model helps to better understand the fundamental concepts and underline physics of AMVHs. With the continuation of the discussion of AMVHs in the following chapters of the thesis, more possible applications will be presented therein.

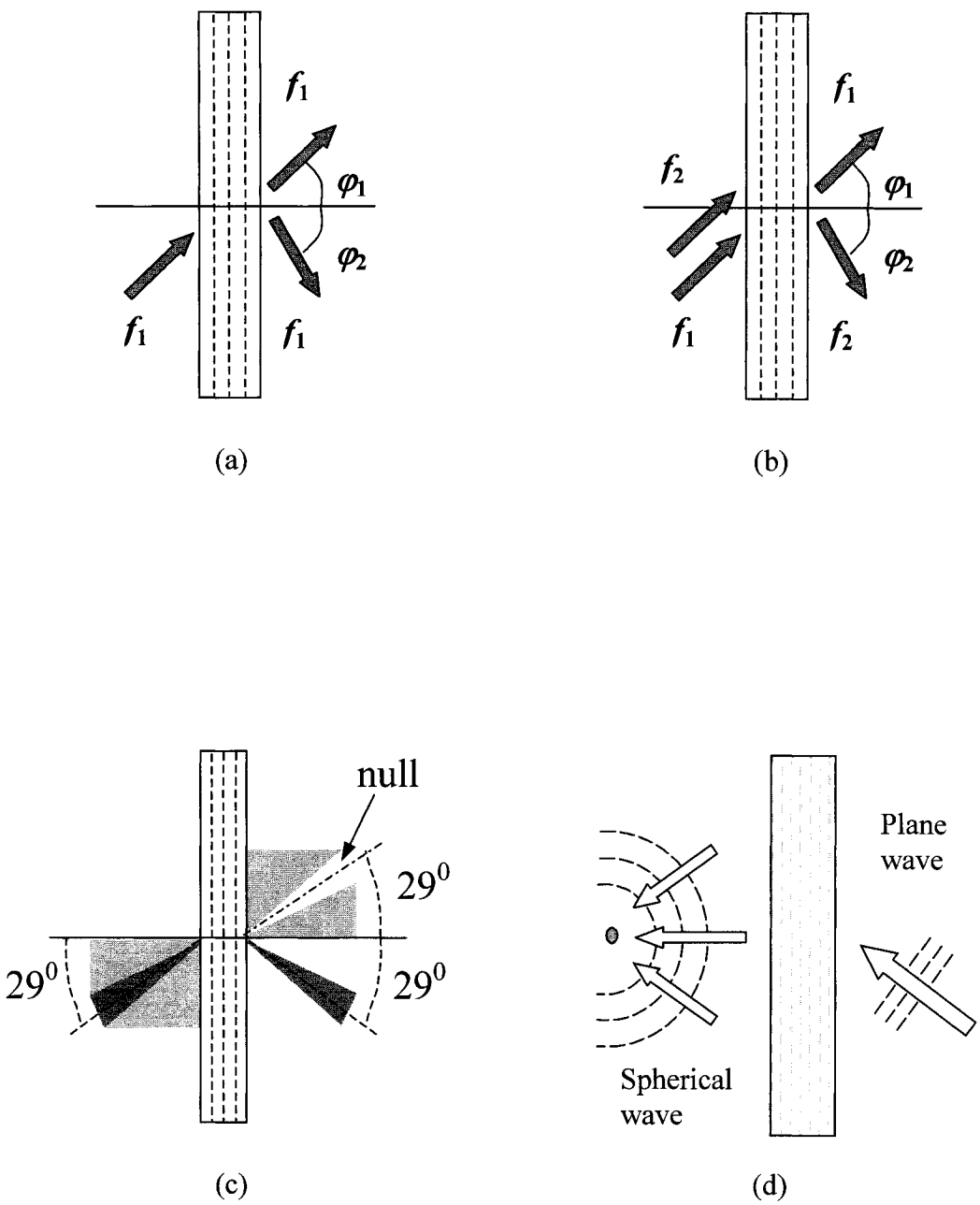

Fig.5.11 Schematic illustration of the possible applications of AMVHs, (a) dual-beam antenna, (b) frequency-enabled beam routing, (c) angle-enabled beam routing, (d) beam focus (or beam wave-front modification).

5.4 Chapter summary and remarks

The parametric study conducted in this thesis provides some preliminary results showing the possible changes in structure response when some parameters vary. Though the study is limited, it does give an outline as for which parameter need to be adjusted and in which direction (increasing or decreasing), when carry out a design optimization. Many parameters have opposite effects, and a trade off is often required to obtain a global optimization. For instance, in order to increase the effective modulation strength, one may (a) increase the patch sizes (limited by the small-obstacle assumption, unless one use other methods to predict the results); or (b) decrease the spacing between lattice planes, and so the total thickness, which reduces the total interaction distance between wave and structure and may weaken the wave form conversion results.

In addition to the square patch shape, it is possible to design a complex patch geometry that occupies less area but has higher electric polarizability. Bear in mind that complex patch shapes often cause fabrication difficulty, and eventually its high theoretical polarizability may not be achievable. It is noted that in selecting the patch shape, we have only considered the electric polarizability and neglected the magnetic polarizability since the magnetic dipoles' contribution is relative small (Sec.3.4). For more accurate evaluation of patch geometries, magnetic polarizability needs to be considered as some geometry may result in a high magnetic polarizability. A numerical method (MoM) has been proposed in [45] for the calculation of magnetic polarizability. It should also be mentioned that the curve fitting formula (5-10) for square patch electric polarizability is valid for the static case or very low frequencies, just like eq (3-16) for circular patches. We still lack a formula that is equivalent to eq.(3-17) and is valid up to the third order of kd for square patches.

Chapter 6

Multiplex AMVHs consisting of multiple holographic gratings: analysis, design, and application potential

One way to overcome the application limitation of single-grating AMVHs is to multiplex several holographic grating into one hologram, each grating plays its own role. Following the idea of multiple exposed thick holograms in the optic holography [50,51], multiplex AMVHs can be implemented by superposing the interference patterns of several pair of object and reference beams. For simplicity, it is assumed that those gratings that are recorded in the same hologram are commensurate along the hologram surface, i.e., the resulting structure after the superposition is still a periodic structure along the hologram surface, and therefore can be analyzed by the dynamic-dipole-interaction-theory developed in the early chapters.

6.1 Multiplex AMVHs design and simulation

At a given frequency, each dielectric grating can be considered to be proportional to the interference pattern of a set of object-reference beams. To simplify the analysis, consider a multiplex AMVH consisting of only two dielectric gratings of equal strength. Those superposing more than two dielectric gratings of different strengths can be processed in a similar way. Figure 6.1 shows two sets of object-reference plane waves beams (or simply called recording beams hereafter), propagating through a slab region in a dielectric host medium. The intensity of the total field of a set of recording beams is proportional to

$$|E_o^y + E_r^y|^2 \propto \cos(\boldsymbol{K}_{\alpha\beta} \bullet \boldsymbol{r}), \quad \text{where } \boldsymbol{K}_{\alpha\beta} = \boldsymbol{k}_\alpha - \boldsymbol{k}_\beta \text{ is the grating vector}$$

and where $\boldsymbol{k}_\alpha, \boldsymbol{k}_\beta$ are the propagation vectors of the set of beams α and β.

By adding together the field intensities of the beam set #1 and the beam #2, the total modulation of dielectric constant can be written as

$$\varepsilon_r(\boldsymbol{r}) = \varepsilon_a + \varepsilon_{d1}\cos(\boldsymbol{K}_{11'} \bullet \boldsymbol{r}) + \varepsilon_{d2}\cos(\boldsymbol{K}_{22'} \bullet \boldsymbol{r}), \quad \varepsilon_{1d} = \varepsilon_{2d} \tag{6-1}$$

where

$$\begin{aligned} \boldsymbol{K}_{11'} &= k[(\cos\varphi_1 - \cos\varphi_{1'})\boldsymbol{z} + (\sin\varphi_1 + \sin\varphi_{1'})\boldsymbol{x}] \\ \boldsymbol{K}_{22'} &= k[(\cos\varphi_2 - \cos\varphi_{2'})\boldsymbol{z} + (\sin\varphi_2 + \sin\varphi_{2'})\boldsymbol{x}] \end{aligned} \tag{6-2}$$

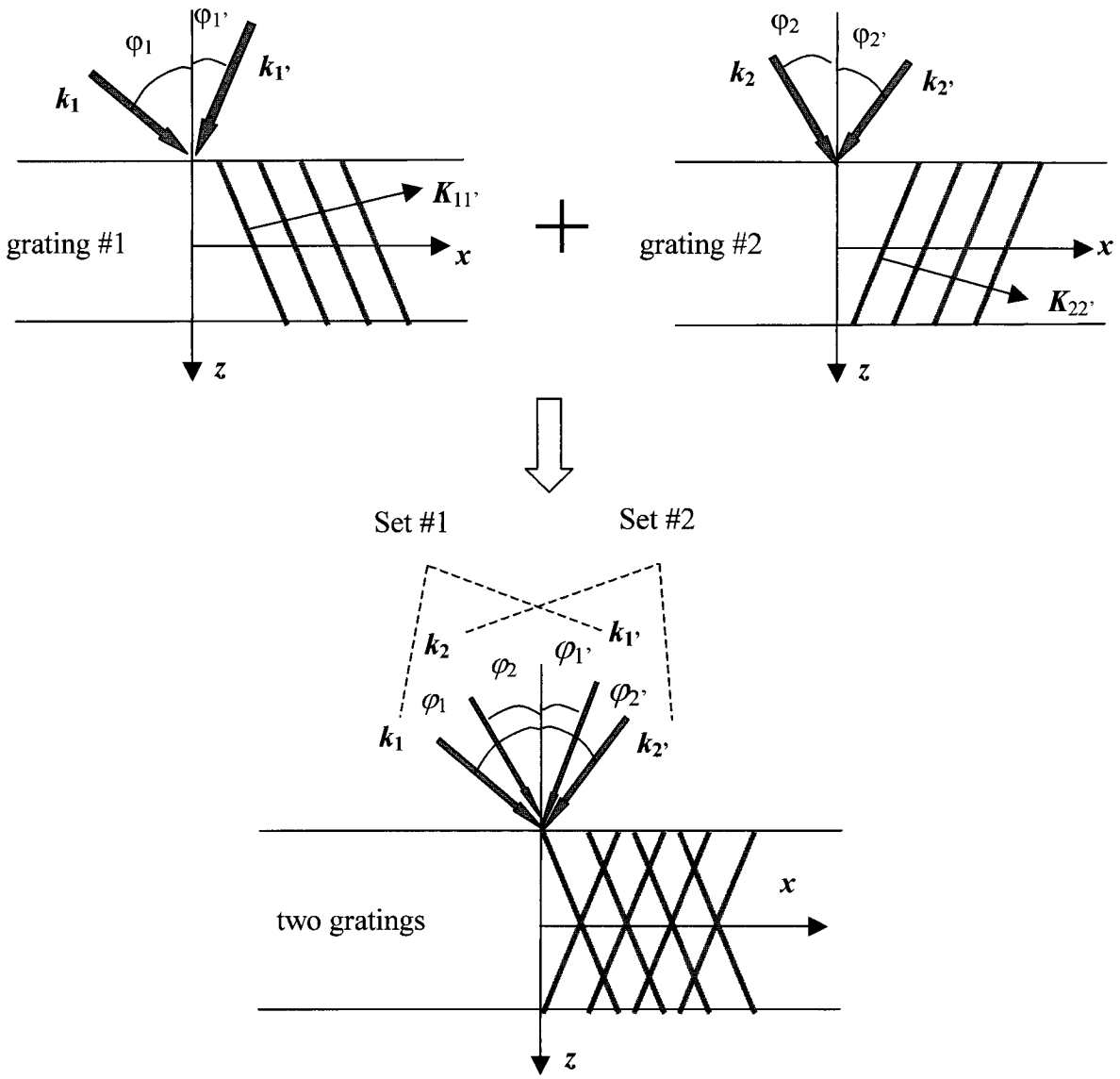

Fig.6.1 A multiplex AMVH formed by superimposing two holographic gratings.

Let

$$\begin{aligned} \Lambda_1 &= \lambda/(\sin\varphi_1 - \sin\varphi_{1'}), \quad \phi_1 = (\varphi_1 + \varphi_{1'})/2, \\ \Lambda_2 &= \lambda/(\sin\varphi_2 - \sin\varphi_{2'}), \quad \phi_2 = (\varphi_2 + \varphi_{2'})/2, \end{aligned} \tag{6-3}$$

then (6-1) can be rewritten as

$$\varepsilon_r(x,z) = \varepsilon_a + \varepsilon_{d1}\cos[2\pi x/\Lambda_1(x - z\tan\phi_1)] + \varepsilon_{d2}\cos[2\pi x/\Lambda_2(x - z\tan\phi_2)] \tag{6-4}$$

The condition for ε_r to be a periodic function of x requires that there exist two minimum integers n_1 and n_2 so that

$$n_1\Lambda_1 = n_2\Lambda_2 = \Lambda, \tag{6-5}$$

where Λ_1, Λ_2 are the wavelengths of the two gratings, and Λ will be the period of ε_r in the x-direction. Equations (6-3) and (6-5) relate the grating parameters to the recording beam parameters. In practical designs, to reduce higher order modes in readout processes, n_1 and n_2 should be controlled as small as possible. The corresponding disk size modulation can be calculated from (6-4) by using the procedure described in Chapter 4 (static-dipole-interaction theory). Below we give two design examples of multiplex AMVHs with simulated results. Those are arbitrary samples and serve only for illustration of the processes of recording and reproducing beams in AMVHs (may have no use in practices).

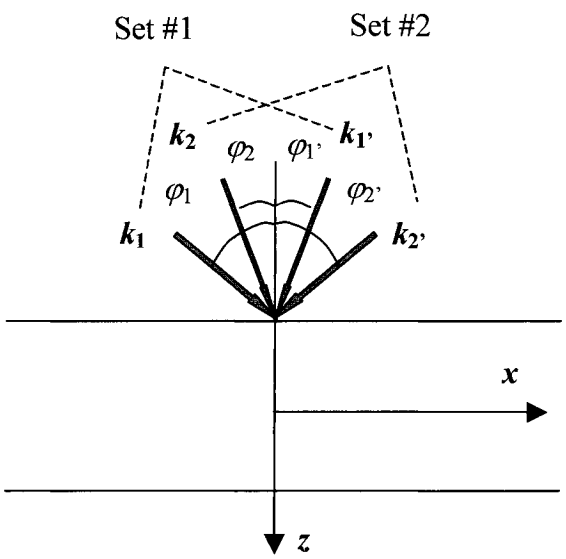

Fig.6.2 A multiplex AMVH having a symmetry axis along z-axis.

6.1.1 Multiplex AMVH Case 1: symmetrical modulation

Consider the following angles of incidence of the two set of recording beams (Fig.6.2), and dielectric constants and frequency.

$$\varphi_1 = -\varphi_{2'} = 24.1^0,\ \varphi_2 = -\varphi_{1'} = 5.75^0,\ \varepsilon_a = 3.8,\ \varepsilon_{d1} = \varepsilon_{d1} = 0.38,\ \varepsilon_H = 3.0,\ f = 30\,\text{GHz},$$

Those angles (measured in the host dielectric) correspond to $\pm 45^0$ and $\pm 10^0$ in air.

From (6-3) and (6-5),

$$\Lambda_1 = \Lambda_2 = \Lambda = \lambda/(\sin\varphi_1 + \sin\varphi_2) = 11.35mm,\ \phi_1 = -\phi_2 = (\varphi_1 - \varphi_2)/2 = 9.17^0,$$

Then, the effective dielectric modulation (6-4) becomes symmetrical about z-axis and can be simplified as

$$\varepsilon_r(x,z) = \varepsilon_a + 2\varepsilon_{d1}\cos(2\pi x/\Lambda)\cos(2\pi z\tan\phi_1/\Lambda)$$

which has a period of Λ=11.35mm in the x-direction. The lattice parameters are chosen as

$$a = b = 0.65\text{mm},\ c = 0.5\text{mm},\ I = 18\,(Ia \approx \Lambda),\ N = 86.$$

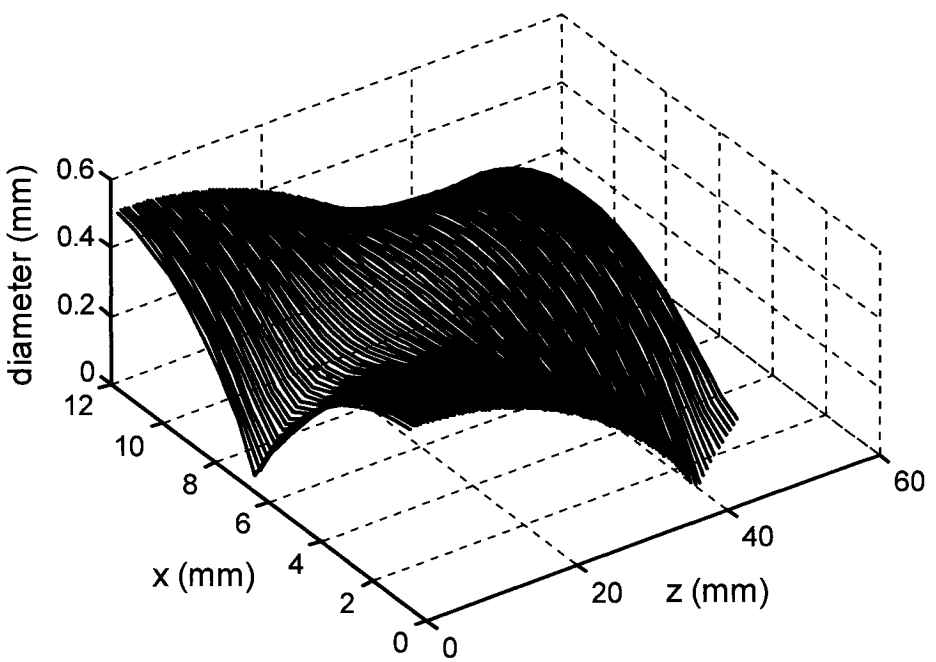

Fig. 6.3 Disk diameter distribution at I×N=18×86 lattice nodes.

The angles are measured from the z-axis with the positive direction being counterclockwise. The calculated disk diameter distribution as a 2D function of x and z is plotted in Fig.6.3. It can be easily verified from (3-7b) that for the given frequency and a range of incidence angle [4^0, 28^0], there exist four propagation modes, i.e., the 0-, –1-, –2-, and +1-orders.

Within the angle range, $\theta_i = 24.1^0 (= \varphi_1)$ and $5.75^0 (= \varphi_2)$ are the Bragg angles of gratings #1 and #2 (formed by beam sets #1 and #2), respectively (Fig.6.2). A readout beam illuminating the hologram at either of the angles will cause a strong reproduction of one of the two recording beams of the respective grating. This reproduced beam appears as the –1-order mode for the case in the Floquet mode expansion of the scattered field (3-18), while the directly transmitted beam as the 0-order mode (Fig.6.4). Figure 6.5 shows the calculated amplitudes of these four propagating modes in the transmission side varying with angle of incidence. As seen, at the Bragg angles of around 6^0 and 24^0, the –1-order diffraction mode becomes dominant with an angle of around -24^0 and -6^0, respectively. For angles between these two values, the 0-order mode is pronounced. (see the diagrams below the figure). At these incidence angles, higher order modes (+1- and –2-orders) exist with their angles being (37^0 and -66^0) and (66^0 and -37^0), respectively. Therefore, an incidence along $\boldsymbol{k}_1$ associated with grating #1 do not reproduce either of beams $\boldsymbol{k}_2$ and $\boldsymbol{k}_{2'}$ that are associated with grating #2, and *vice versa*. This means the cross-coupling is very low for the multiplex AMVH case.

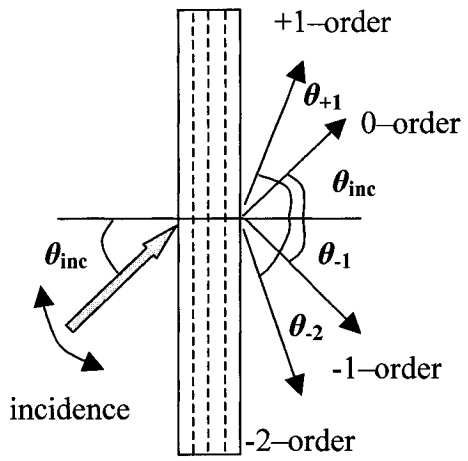

Fig.6.4 Reproduced modes by a plane wave read-out beam.

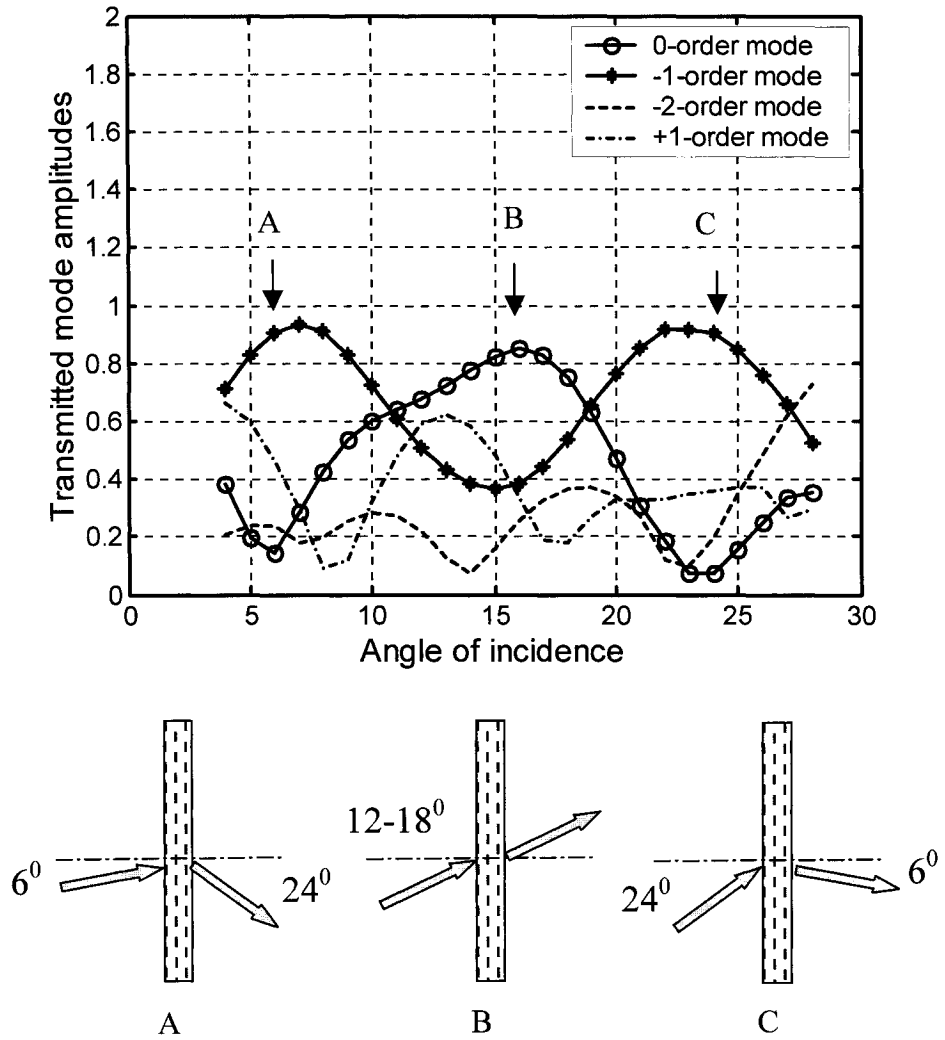

Fig.6.5 Mode amplitudes of the four propagating waves in the forward-scattered field.

6.1.2 Multiplex AMVH Case 2: asymmetrical modulation

Consider the following angles of incidence of the two set of recording beams (Fig.6.6), and dielectric constants and frequency.

$\varphi_1 = \varphi_2 = 26.37^0$, $\varphi_{2'} = -\varphi_{1'} = 8.51^0$, $\varepsilon_a = 3.8$, $\varepsilon_{d1} = \varepsilon_{d1} = 0.38$, $\varepsilon_H = 3.0$, $f = 30\,\text{GHz}$,

As seen, beam 1 in set #1 and beam 2 in set #2 merge into one beam. Those angles (measured in the host dielectric) correspond to 50.29^0 and $\pm 14.86^0$ in air.

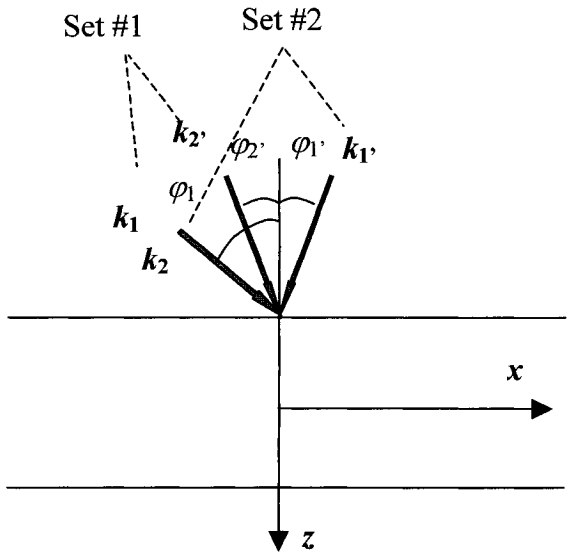

Fig.6.6 A multiplex AMVH with a common recording beam.

From (6-3) and (6-5),

$$\Lambda_1 = \lambda/(\sin\varphi_1 - \sin\varphi_{1'}) \approx 9.75\text{mm}, \quad \phi_1 = (\varphi_1 + \varphi_{1'})/2 = 8.93^0,$$
$$\Lambda_2 = \lambda/(\sin\varphi_2 - \sin\varphi_{2'}) \approx 19.5\text{mm}, \quad \phi_2 = (\varphi_2 + \varphi_{2'})/2 = 17.44^0,$$
$$\Lambda = \Lambda_2 = 2\Lambda_1 = 19.5\text{mm},$$

So, there is a common period of Λ=19.5mm for the two gratings along the x-direction. The lattice parameters are chosen as

$$a = b = 0.65\text{mm}, \quad c = 0.5\text{mm}, \quad I = 30\,(Ia \approx \Lambda), \quad N = 73.$$

The calculated disk diameter distribution is given in Fig.6.7 as a 3D plot, which is not symmetrical about z-axis. There are a total of eight propagation modes for the given frequency and the range of incidence angle [-10^0, 28^0], i.e., 0-, −1-, −2-, −3-, −4-, +1-, +2-, and +3-orders. For this range of incidence angle, the three Bragg angles are $\theta_i = 26.37^0 (= \varphi_1 = \varphi_2)$, $8.51^0 (= \varphi_{2'})$, $-8.51^0 (= \varphi_{1'})$, respectively. Because of the common beam or the common Bragg angle ($\boldsymbol{k}_1$=$\boldsymbol{k}_2$), there will be two different ways for readout. When a readout beam is in the common beam direction $\boldsymbol{k}_1$=$\boldsymbol{k}_2$, it reproduces both the $\boldsymbol{k}_{1'}$ and $\boldsymbol{k}_{2'}$ beams (Fig.6.6). This can be called "beam-splitter readout". When a readout beam is in the $\boldsymbol{k}_{1'}$ ($\boldsymbol{k}_{2'}$) direction, it reproduces the common beam $\boldsymbol{k}_1$=$\boldsymbol{k}_2$ (direct diffraction), while the latter, in turn, can reproduce the $\boldsymbol{k}_{2'}$ ($\boldsymbol{k}_{1'}$) beam (secondary diffraction). This is thus called

"cross-coupling readout". Either way, an incidence at any Bragg angle always reproduces the two other recording beams, though they do not have to have the same amplitudes. The directions of the diffraction orders rely on the incidence angle of the readout beam by

$$\sin\varphi_{\pm m} = \sin\vartheta_{in} \pm m\frac{2\pi}{k\Lambda}, \quad m = 0,1,2,\cdots. \tag{6-6}$$

Figure 6.8 shows the predicted mode amplitudes of the eight forward-scattered propagating waves varying with angle of incidence. Unlike the first example in the previous subsection, the two reproduced recording beams are not always tied with two specific diffraction orders, but will be related to different orders depending on the angle of incidence. This will be evident when we explain below how the beam reproducing occurs at the Bragg angles. It is also noted that not all eight modes exist within the whole angle range, the data marks that fall on the x-axis in Fig.6.8 indicate the corresponding propagating modes disappear or don't exist (non-propagating) for the angles.

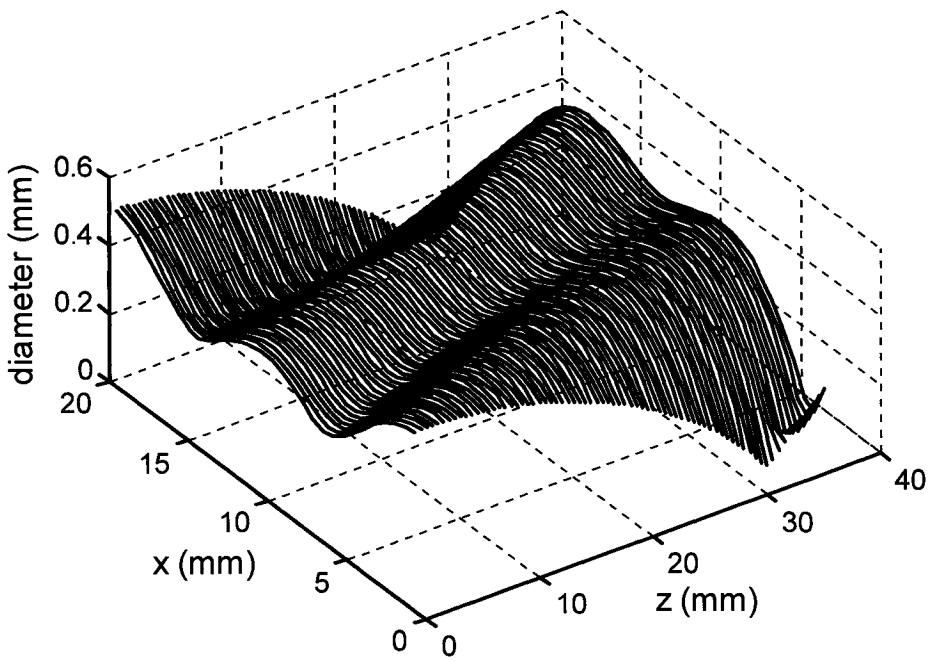

Fig. 6.7 Disk diameter distribution at $I\times N$=30×73 lattice nodes.

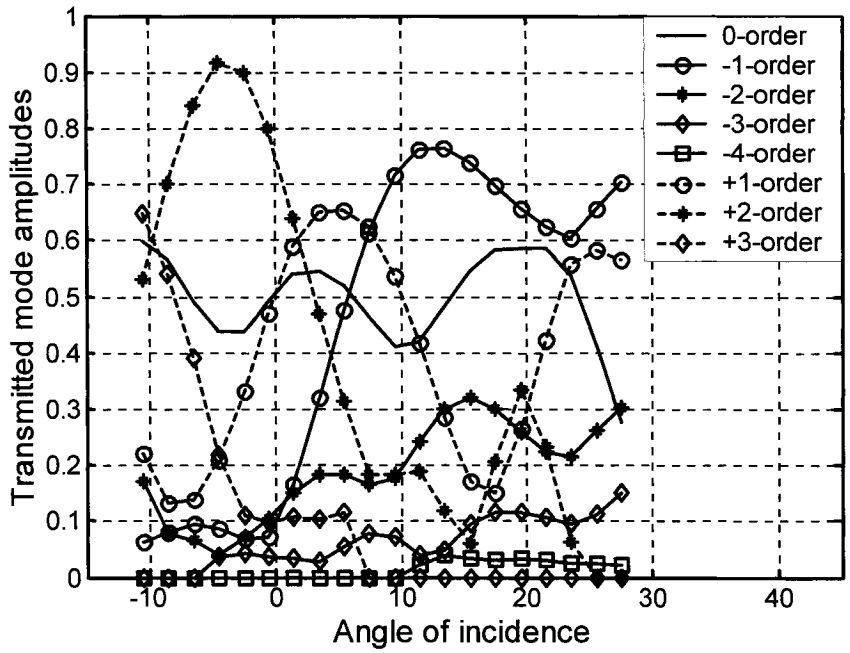

Fig.6.8 Mode amplitudes of the eight propagating waves in the forward-scattered field.

At a Bragg angle of $\theta_{in} = -8.51^0 (= \varphi_{1'})$, the readout beam is in the $\boldsymbol{k}_{1'}$ direction and the reproduced beams are in $\boldsymbol{k}_1$=$\boldsymbol{k}_2$ (+26.37^0) and $\boldsymbol{k}_{2'}$ (+8.51^0) directions, respectively. The directions of the diffraction orders are calculated by (6-6) as

$$\varphi_{-1} = -26.37^0,\ \varphi_{-2} = -47.75^0,\ \varphi_{+1} = 8.51^0,\ \varphi_{+2} = 26.37^0,\ \varphi_{+3} = 47.75^0,$$

and all the other orders become non-propagating.

As seen in Fig.6.8, the direct diffraction wave ($\boldsymbol{k}_1$=$\boldsymbol{k}_2$) corresponds to the +2-order and is dominant (dashed line and asterisk marks). The secondary diffraction wave ($\boldsymbol{k}_{2'}$) is the +1-order, and is quite small (dashed line and circle marks). Some other modes, such as 0-order (direct transmission) and +3-order (dashed line and diamond marks), are in between.

At Bragg angle of $\theta_{in} = 26.37^0 (= \varphi_1 = \varphi_2)$, the readout beam is in $\boldsymbol{k}_1$=$\boldsymbol{k}_2$ direction and the reproduced beams are in $\boldsymbol{k}_{1'}$ (−8.51^0) and $\boldsymbol{k}_{2'}$ (+8.51^0) directions, respectively. The directions of the diffraction orders are given through (6-6) as

$$\varphi_{-1} = 8.51^0,\ \varphi_{-2} = -8.51^0,\ \varphi_{-3} = -26.37^0,\ \varphi_{-4} = -47.75^0,\ \varphi_{+1} = 47.75^0,$$

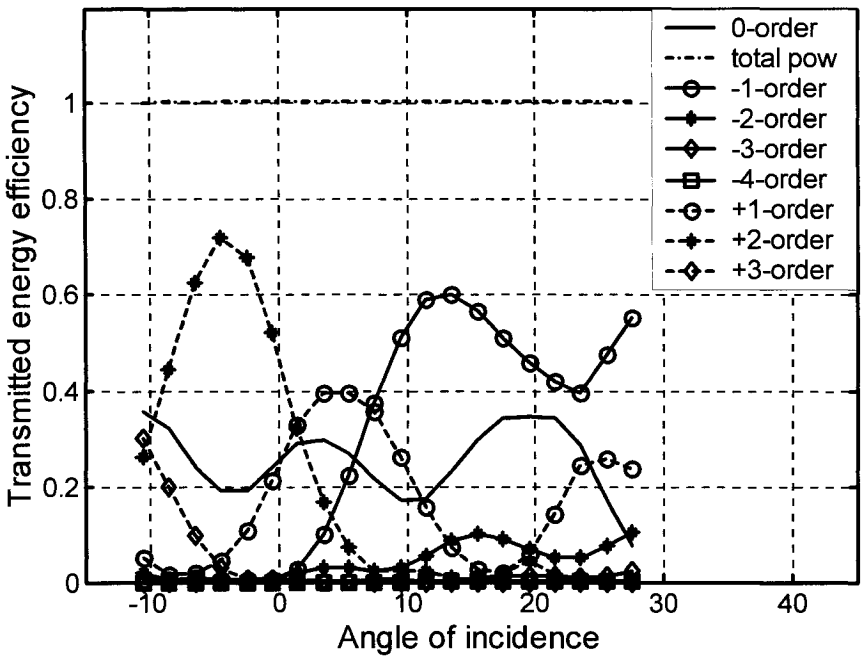

Fig.6.9 Energy efficiencies of the eight propagating waves in the forward-scattered field.

and other orders are non-propagating. Now, the two direct diffraction waves $\boldsymbol{k}_1$, and $\boldsymbol{k}_2$, correspond to the –2-order and –1-order, respectively, while the latter is dominant (solid line and circle marks in Fig.6.8) and the former is relative small (solid line and asterisk mark in Fig.6.8). This is probably because the latter is closer spatially to the common beam than the former. The case at the Bragg angle of $\theta_{in} = 8.51^0 (= \varphi_{2'})$ can be discussed in a similar way.

The energy efficiencies of all propagating waves are also calculated and are plotted in Fig.6.9, in which the energy conservation law is satisfied very well (central dot line), in spite of the fact that there are as many as eight propagating modes in each side (transmission and reflection) of the hologram. (For a clear plot, the reflection modes' efficiencies, which are quite small, are not shown in the figure)

6.2 Microwave free-space beam splitter and combiner

Now, consider a special, but important sub-set of the above general multiplex AMVHs. Let the beams $\boldsymbol{k}_1$, and $\boldsymbol{k}_2$ in Fig.6.2 of subsection 6.1.1 collapse into one beam

along the z-direction, as shown in Fig.6.10a, we then obtain a symmetrical beam splitter that could be useful in practical applications, such as spatial power combining. Since the beam $\boldsymbol{k}_1$ is a common beam of the recording sets #1 and #2, it is anticipated that illuminating the hologram along its normal will reproduce the symmetrical beams 2 and 2'simultaneously (Fig.6.10b). Below we first consider the simpler case represented by Fig.6.10a.

6.2.1 1-to-2 and 1-to-3 beam splitting

For the beam splitter as shown in Fig.6.10, the dielectric modulation function (6-4) becomes

$$\varepsilon_r(x,z) = \varepsilon_a + 2\varepsilon_{d1}\cos(\frac{2\pi}{\Lambda}x)\cos(\frac{2\pi}{\Lambda}z\tan\frac{\varphi_1}{2}), \quad \text{with } \Lambda = \frac{\lambda}{\sin\varphi_1} \tag{6-7}$$

Consider the following parameters for the splitter,

$$\varepsilon_H = 3.0,\ \varepsilon_0 = 3.8,\ \varepsilon_1 = 0.39,\ \lambda = 5.774\text{mm},\ \varphi_2 = -\varphi_{2'} = 29.67^0,$$
$$\Lambda = Ia = 11.662\text{ mm},\ I = 14,\ N = 66,\ a = b = 0.833\text{ mm},\ c = 0.508\text{ mm},$$

The angle is given in the host dielectric, which corresponds to 59^0 in air. The calculated 2D disk diameter distribution is plotted in Fig.6.11.

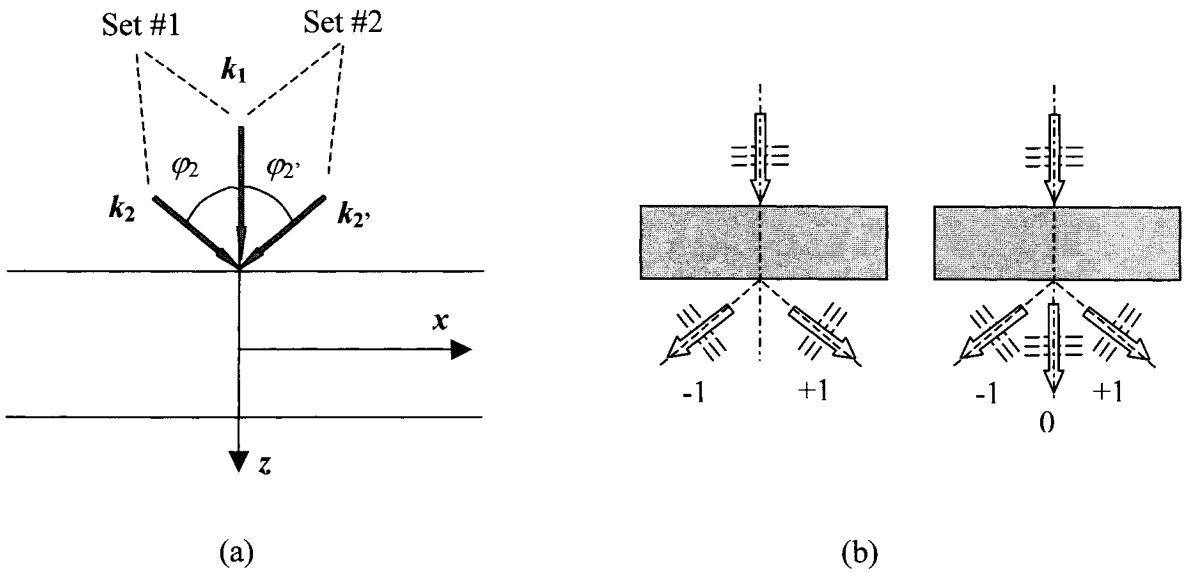

(a) (b)

Fig. 6.10 Free-space beam 1-to-2 or 1-to-3 splitter based on symmetrical multiplex AMVHs, (a) recording step, (b) reconstructing step (1-to-2 and 1-to-3 splitting).

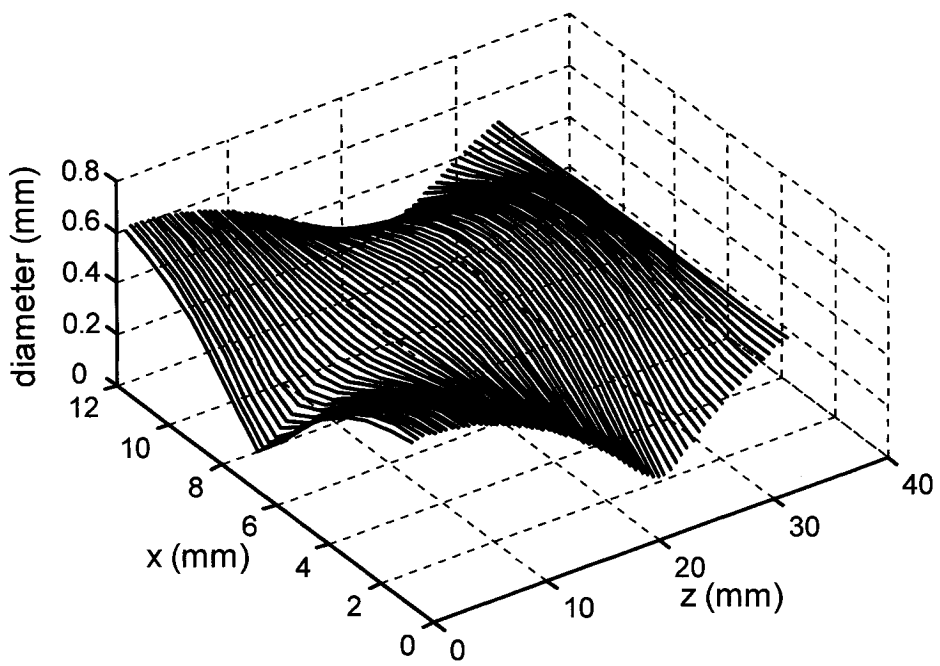

Fig. 6.11 Disk diameter distribution at $I \times N$=14×66 lattice nodes for the 1-to-2 splitter.

For a readout beam at normal incidence, there are three propagating modes (0- and ±1-orders) that could be reproduced. Figure 6.12a shows the predicted mode amplitudes of the three transmitted waves against frequency. Due to the symmetry of the problem, the ±1-order modes have the exact same behavior. As seen, at a frequency range of $f \in$ [28, 30] GHz, the direct transmitted beam (0-order) nearly vanishes (solid line) and the total incident energy splits evenly between the two diffract modes (±1-orders). The angle of the output beam with respect to the normal is determined by the frequency, which is 59^0 (in air) for 30GHz. Higher order modes (±2-orders) appear as $f >$ 29.5GHz, but they are not significant (asterisk marks). So are the reflected modes (dashed lines). The energy efficiencies of the propagation modes and the total energy balance are shown in Fig.6.12b. This readout process is simply a 1-to-2 beam splitting.

It is found that by adding more layers of same lattice, it is possible to achieve 1-to-3 splitting, i.e., the normal incident beam is converted to two diffraction waves (±1-orders) plus the directly transmitted wave (0-order).

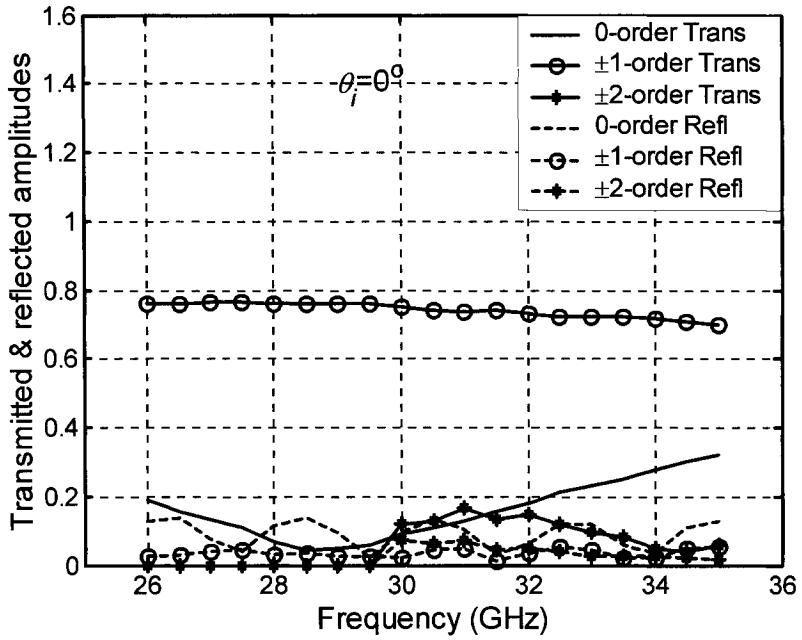

(a)

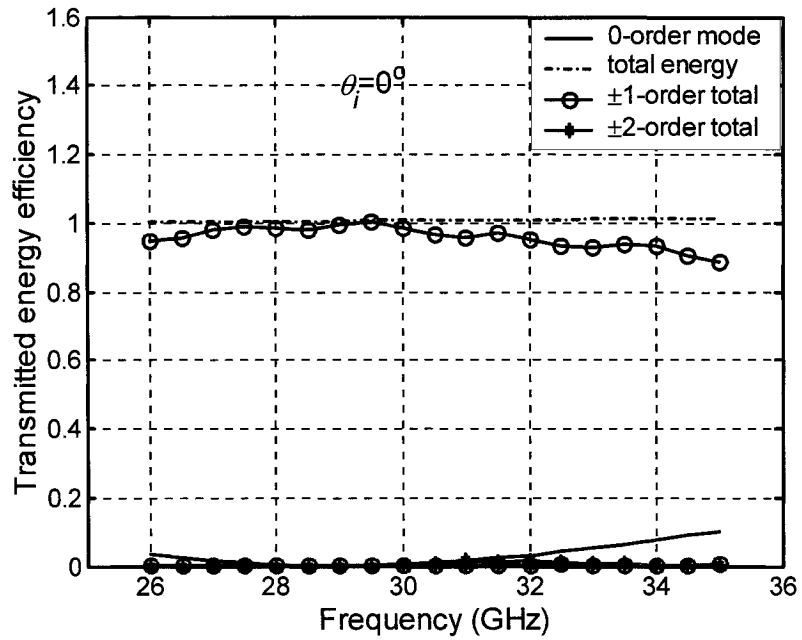

(b)

Fig.6.12 Calculation of the reproduced wave beams, (a) mode amplitudes, (b) mode energy efficiencies, of a 1-to-2 beam splitter based on a multiplex AMVH (N=66).

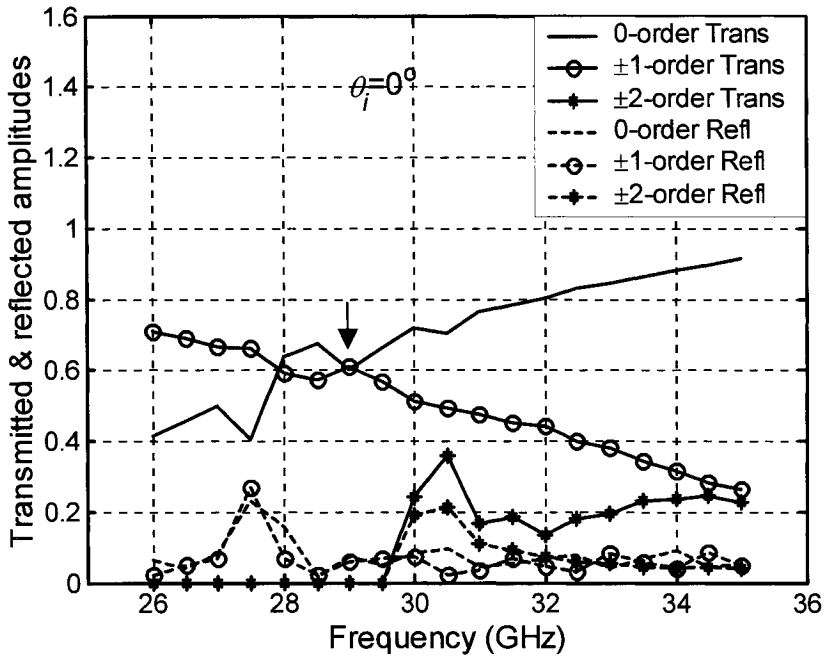

Fig.6.13 The reproduced waves of a beam splitter with more layers (N=89), showing the cross-point, where the 0-order and ±1-orders have the equal amplitude.

Figure 6.13 shows such splitting result by setting the number of layers to be N = 89, which is found using try-and-correct method. As can be seen, the resulting three modes have equal amplitudes at a frequency of about 29 GHz. It can be shown that the 1-to-3 splitting can also be realized by varying the layer thickness c, instead of the number of layers [52]. Actually, any desired amplitude ratio between the 0-order and ±1-orders can be achieved by continually varying the total thickness Nc. Finally, based on the reciprocity principle [53], a beam splitter can be a beam combiner, by reversing the propagation direction.

6.2.2 1-to-4 or 1-to-5 beam splitting

The simple beam splitting scheme can be extended to include more recording beams (therefore more reproduced beams). Figure 6.14a shows five recording beams comprising four recording sets (gratings), with the common recording beam being the normal incident wave. In the reconstructing step, use of a normal incident plane wave as the read-out beam will reproduce at least four beams in symmetry about the normal of the hologram, which

correspond to the ±1-orders and ±2-orders (Fig.6.14b). The parameters used for the splitter are,

$\varepsilon_H = 3.0$, $\varepsilon_0 = 3.8$, $\varepsilon_1 = 0.287$, $\varepsilon_2 = 0.137$, $\varphi_2 = -\varphi_{2'} = 28.76^0$, $\varphi_3 = -\varphi_{3'} = 13.92^0$,
$\lambda = 5.774$mm, $\Lambda = Ia = 24$ mm, $I = 40$, $N = 75$, $a = b = 0.6$ mm, $c = 0.508$ mm,

The propagation angles of the reproduced beams in air are $\pm 56.4^0$ and $\pm 24.6^0$. The calculated 2D disk diameter distribution is plotted in Fig.6.15. For the given parameters, it can be shown that there are total of nine possible propagating modes, i.e., 0-order, ±1-orders, ±2-orders, ±3-orders, and ±4-orders. While the higher orders (±3- and ±4-orders) have propagation angles larger than the critical angle of the dielectric and will be confined by the air-dielectric interface, the 0-order mode will come out of the hologram and could become one of the split beams. Figure 6.16 shows the simulated wave amplitudes of the reproduced beams vs the frequency of incidence. As seen, at 30 GHz the ±1-orders and ±2-orders have the same amplitude and the 0-order becomes relative small, thus a 1-to-4 evenly splitting is approximately realized. To arbitrarily raise one mode while suppress another mode to the required levels is not trivial. But, by altering the above parameters and adjusting the relative grating strength, this can be done to a certain degree.

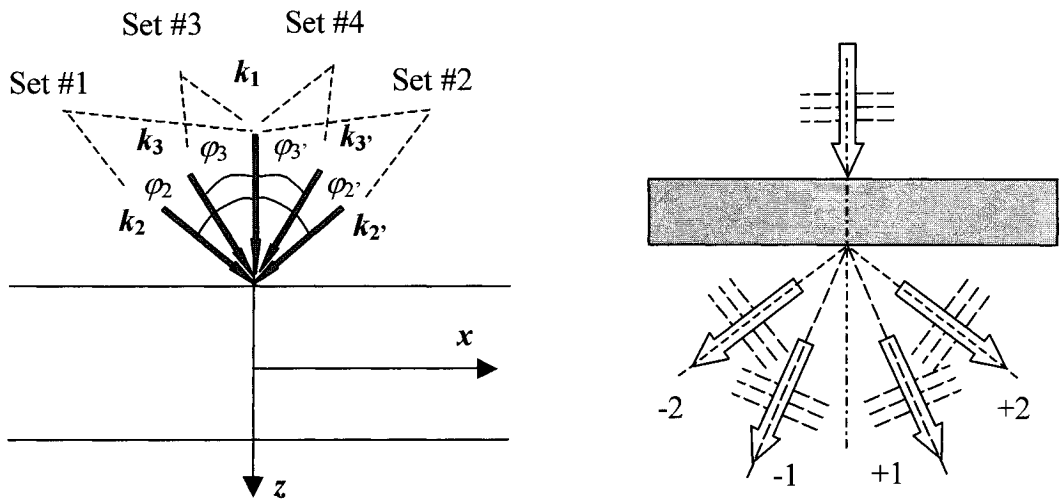

(a) (b)

Fig. 6.14 Free-space 1-to-4 beam splitter based on symmetrical multiplex AMVHs, (a) recording step, (b) reconstructing step.

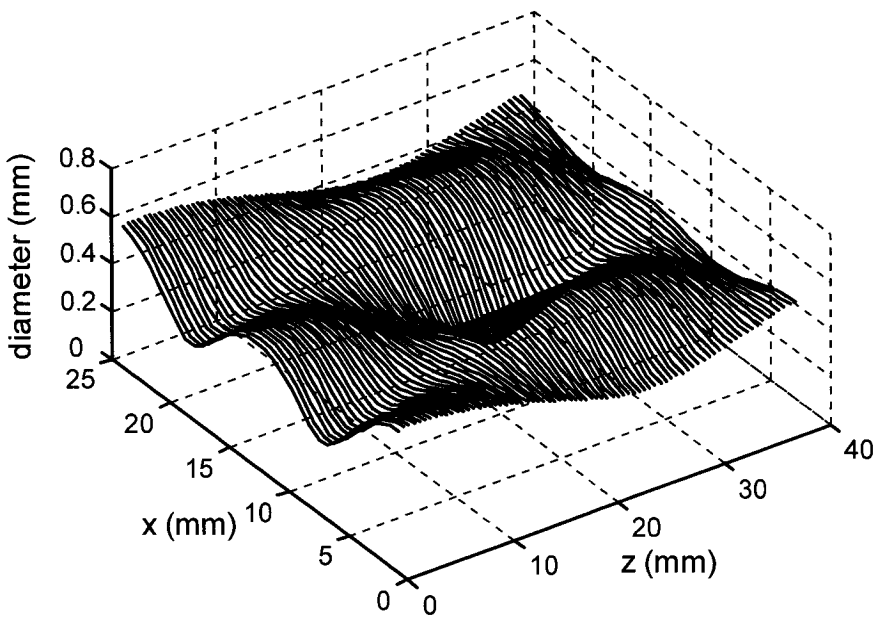

Fig. 6.15 Disk diameter distribution at $I \times N$=40×75 lattice nodes for the 1-to-4 splitter.

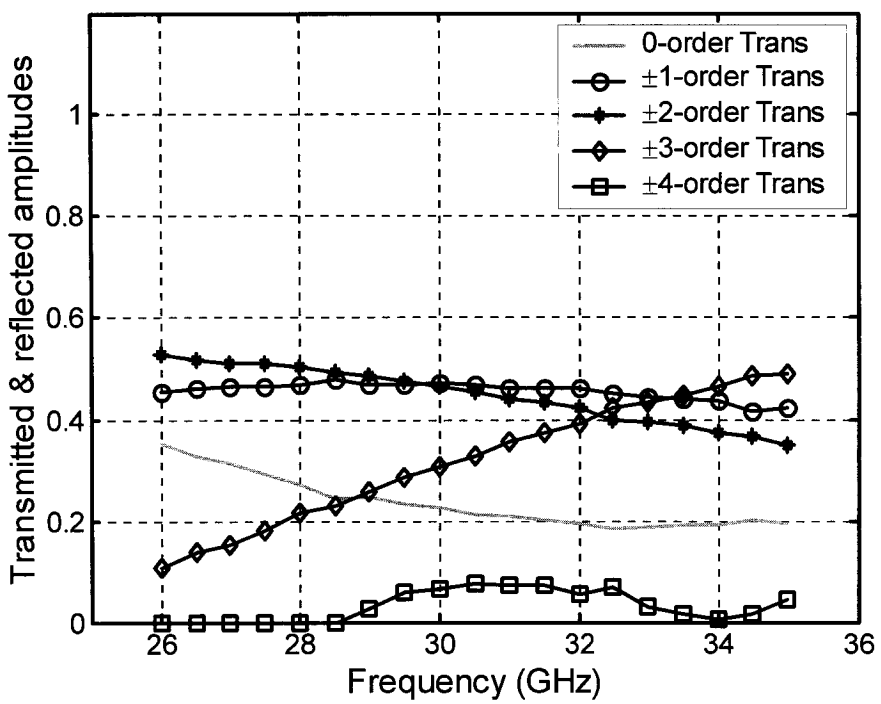

Fig.6.16 Split waves' amplitudes from a multiplex AMVH beam splitter (1-to-4).

6.3 Chapter summary and remarks

It has been shown through simulations that multiplex AMVHs can be realized in the similar way as in optical multiplex holograms, by superposing the interference patterns of several pair of object and reference beams. Among the examples presented above, those with a common beam in the recording stage are of practical importance, as they can be used as microwave spacial beam splitting and combining devices. Others could be useful in multi-beam (or multi-function) antennas or in shared apertures. For multiplex AMVHs, each holographic grating has a related angular window of finite width. When integrating multiple gratings into one hologram, in order to prevent these angular windows from overlapping each other, there will be a limit on the maximum number of beams that can be shared in the hologram. This will depend on the widths of the angular windows as well as the total-reflection angle of the dielectric host.

There are actually two ways to carry out the superposition of multiple beam interference patterns. One is to sequentially record each interference pattern (due to a pair of object and reference beams), the resulting grating function is a simple algebra addition of each individual grating function representing each interference pattern. Multiplex holograms formed in this way are usually called sequential-recording multiplex holograms in optical holography. All the multiplex AMVHs discussed in this chapter fall within this category. The other way is to simultaneously record the entire interference pattern of all the object-reference beam pairs, the resulting grating function is a geometrical addition of each grating vector. Multiplex holograms formed in this way are usually called simultaneous-recording multiplex holograms in optical holography. The latter has a more complicated grating function that includes many cross terms representing the intermodulation effects. It would be interesting to explore the features of simultaneous-recording multiplex holograms under the context of AMVHs, though many research works were done in optic area.

Chapter 7

Experimental procedure and measurements

The experimental work related with this thesis research was carried out at the Quasi-Optical Microwave Lab at the Communications Research Center (CRC). The artificial microwave volume holograms designed were fabricated by the CRC's chemical shop. This chapter will describe the experiment setup, measurement technique, and the hologram fabrication. The measured results are compared with the theoretical results for different AMVH designs. Use of Gaussian beams and their possible effects on the measured results are also discussed.

7.1 The fabricated AMVHs

The artificial microwave volume holograms (AMVHs) fabricated at CRC use Rogers 3003 dielectric sheets as the substrates and Arlon CLTE-P prepreg material as the bonding films. Rogers 3003 is a low loss dielectric (ε_r = 3.00±0.04) for high frequency applications with laminate capable of being used up to 30-40 GHz. It also has good mechanical and temperature properties for multi-layer board constructions. Arlon CLTE-P prepreg material has a dielectric constant ε_r = 2.94, which is quite close to Rogers 3003. The selection of the bonding material is carefully considered to minimize the variation in dielectric constant between the host material and the bonding film. The thickness of Rogers 3003 sheet can be chosen at 0.010", 0.015", 0.020", and so on, while the thickness of Arlon CLTE-P ply is 0.003" originally and is around 0.0024" under the processing pressure. Bonding is accomplished by raising the lay-up temperature to 525^0-550^0F under press of 400psi, and holding for 45 minutes, and then cooling below 150^0F before removing from the press. A photo of the fabricated single-grating hologram is given in Fig.7.1, which made by 81 layers of Rogers 3003, each layer measures 6"x6" and a thickness of 0.020".

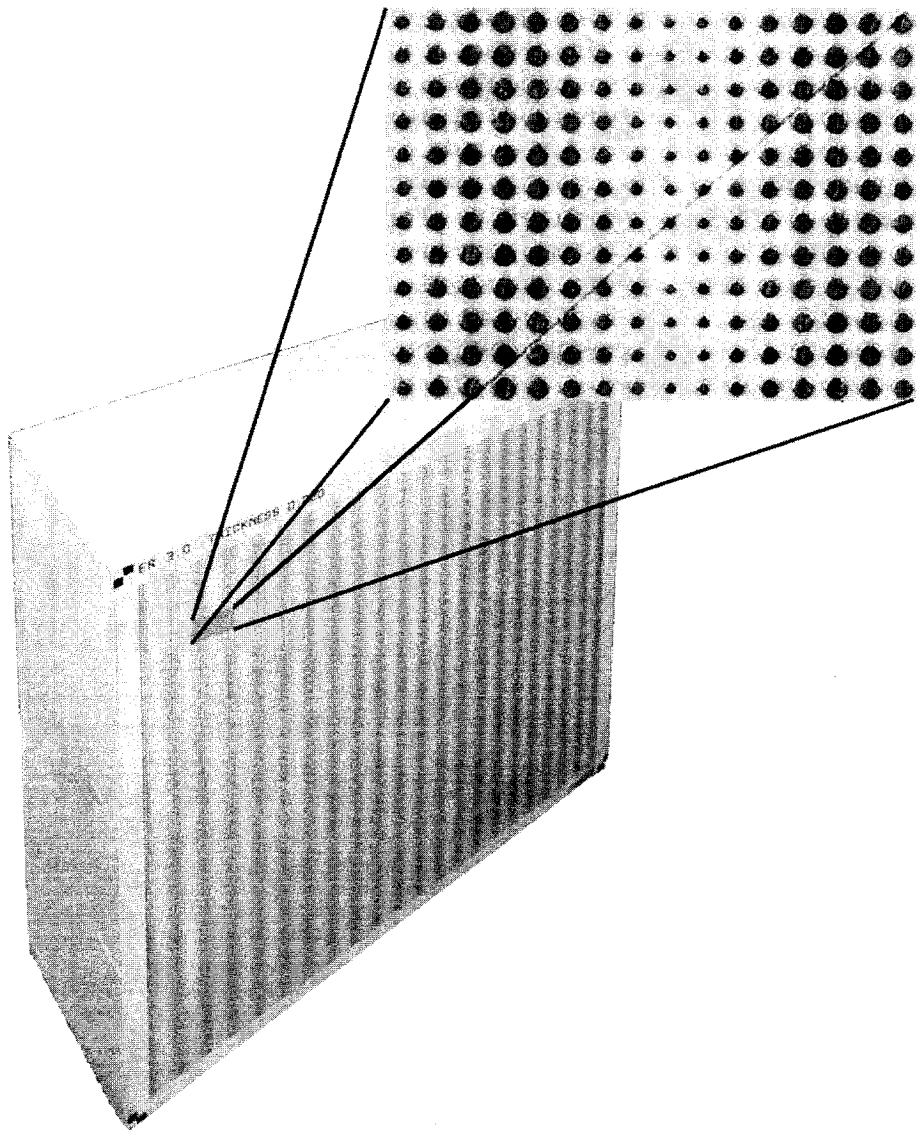

Fig.7.1 Photo of a single-grating AMVH, with the inset showing the variable-size disk lattice. (Photo courtesy of Jafar Shaker of the CRC)

7.2 Measurement system

The measurement system is a so called Quasi-Optical Test Bench [54]. The topology of the test bench is shown in Fig.7.2. It consists of two similar lenses fed by horn antennas, the latter are connected to the source and the receiver, respectively. One of the horn antennas launches a Gaussian beam, which is then refocused by the hyperbolic lens (Fig.7.2). By setting the lenses at a proper distance (twice the focal length) from each other, the Gaussian beam's waist will coincide with the mid-point between the two lenses and its wave-front becomes flat. A device under test (DUT), i.e., a volume hologram, will be placed at this beam waist location.

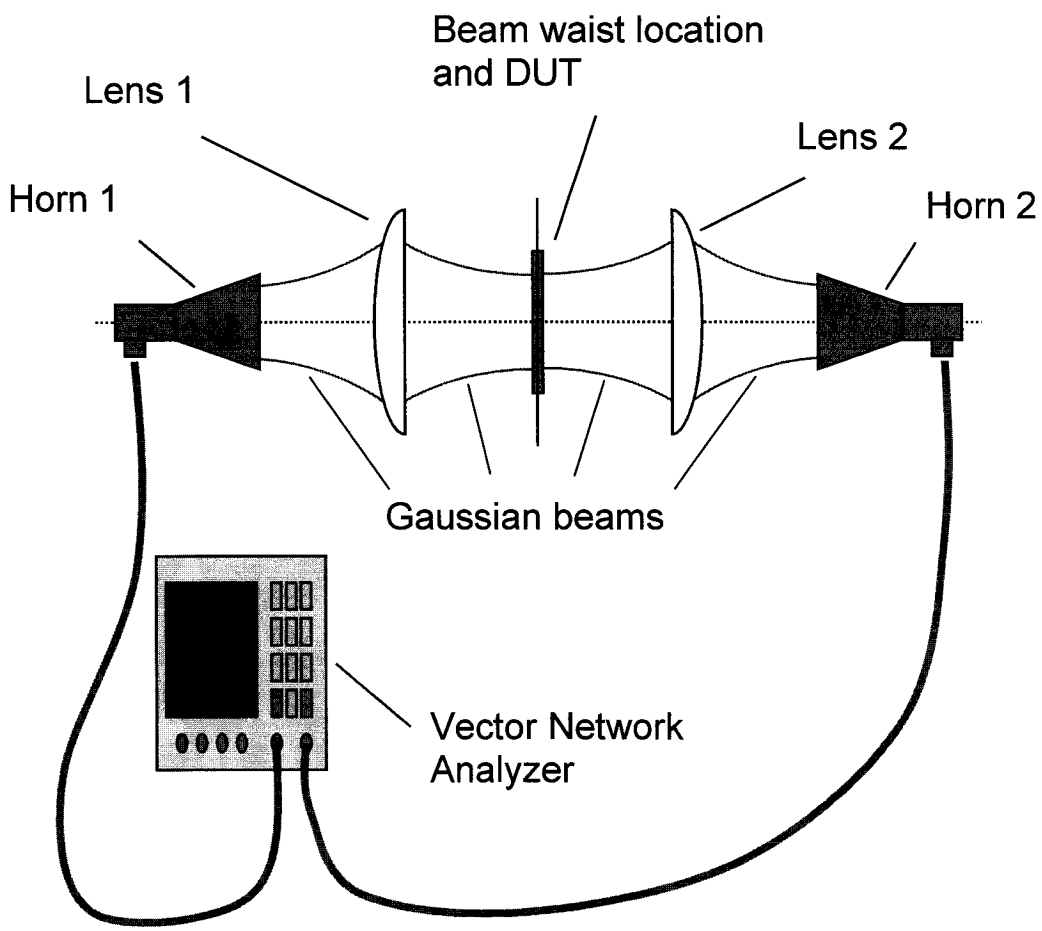

Fig. 7.2 Quasi-optical measurement system.

The transmitted beam from the DUT will be refocused by the second lens into the receiving horn antenna. A vector network analyzer was employed to gain all the scattering parameters of the two-port system. Several similar configurations were reported in [55-57]. To obtain angle scan capability, each lens and its fed horn are mounted on a metal arm, which can be rotated along a circular rail with its center being at the focus. The transmitter arm and the receiver arm can be operated independently to provide further measurement flexibility (i.e., the angle of incidence and the angle of receiving can be scanned separately). The whole system is set up on a vibration-isolated work bench for stable and reliable measurements. Figure 7.3 shows an over view of the system, where the DUT in the photo is a generic dielectric sample (not AMVH).

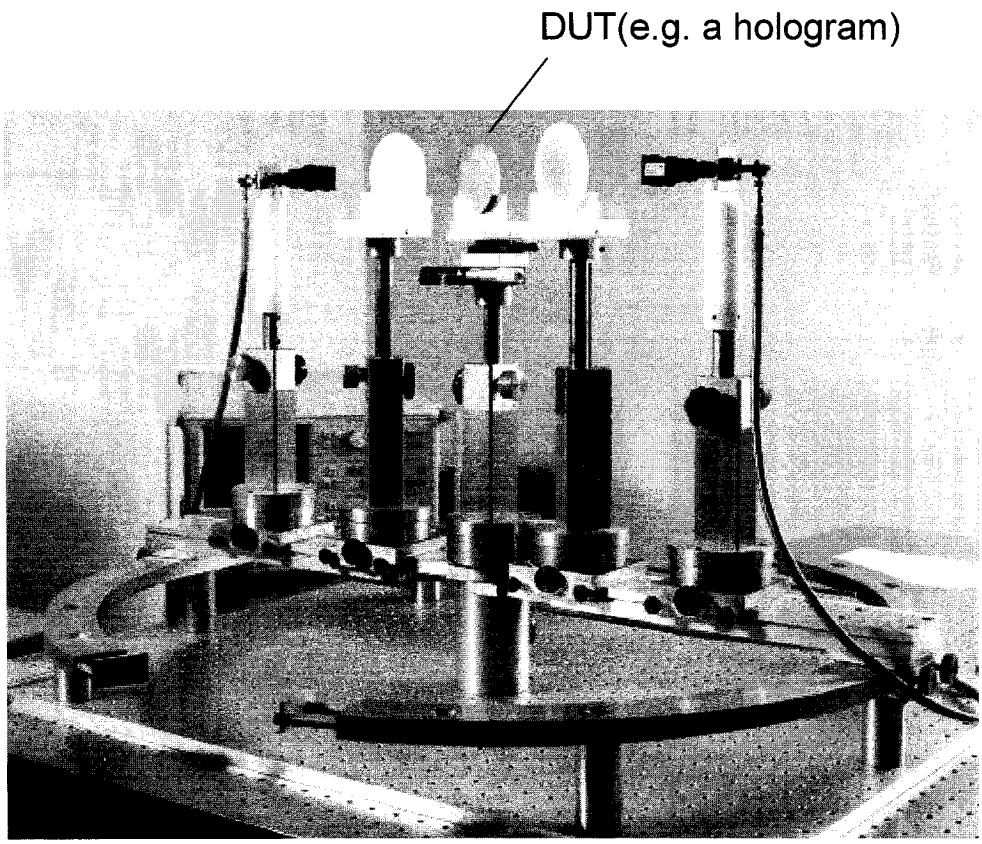

Fig.7.3 A picture showing the overview of the quasi-optical measurement system.

(Photo courtesy of Michel Cuhaci of the CRC)

Furthermore, the antenna horns and the corresponding waveguides can be rotated along their axes to achieve the required polarization direction (such as perpendicular or parallel polarization). Figure 7.4 shows a top view of the measurement system, where both the circular tracks provide an angle scan range [-64^0, $+64^0$]. The beam width at the waist between the two lenses (the focus point) is about 25mm. The following Table 7.1 presents the parameters of the Plexiglas lens [58].

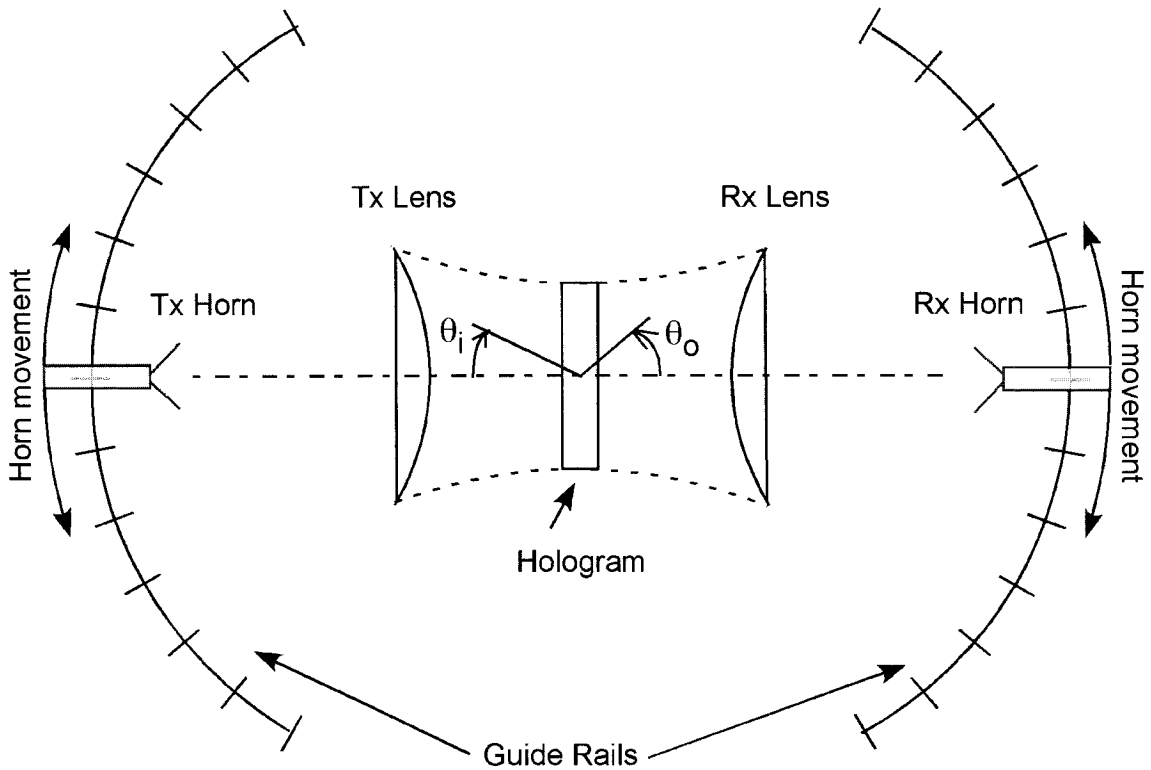

Fig.7.4 A top view of the quasi-optical measurement system.

(Diagram courtesy of Jafar Shaker of the CRC)

Table 7.1 Parameters of the Plexiglas focusing lens

Parameters	Symbol	value
Focal length (mm)	F	93
Diameter (mm)	D	89.27
Thickness (mm)	T_{lens}	14.94
Dielectric constant	ε_{lens}	2.56

Table 7.2 Parameters of fabricated AMVHs

Parameter	Single-grating AMVH	Multiplex AMVH #1	Multiplex AMVH #2
Recording beam angles	$(-55^0, +55^0)$	$(-45^0, +10^0)$, $(+45^0, -10^0)$	$(-45^0, +10^0)$, $(-45^0, -10^0)$
Lattice constants	a=b=0.6 mm, c=0.5mm	a=b=0.65 mm, c=0.5mm	a=b=0.65 mm, c=0.5mm
Period	6 mm	11.7 mm	N/a
Number of layers	N=81	N=86	N=73
Dimension	152x152x40.5 mm^3	152x152x43 mm^3	152x152x36.5 mm^3
Dielectric modulation	ε_d=0.4	ε_{d1}=ε_{d2}=0.379473	ε_{d1}=ε_{d2}=0.379473
Average dielectric	ε_a=3.6	ε_a=3.6	ε_a=3.6
Host dielectric	ε_H=3.0	ε_H=3.0	ε_H=3.0

7.3 Measured results and comparison

The first AMVH that is tested is the single-grating hologram as shown in Fig.7.1, and its parameters are given in the Table 7.2. The hologram is placed at the mid-point between the two lenses where the beam waist is located. A TE incidence beam launched from one horn antenna is used as the read-out beam, in which the *E*-field is perpendicular to the plane of incidence. The direct transmitted and diffracted waves are detected by the receiving lens and horn antenna of same polarization. Figures 7.5a and 7.5b depict the recording and reconstructing processes of the single-grating AMVH. The measured relative powers of the two propagating wave modes are plotted in Fig.7.6 in dB. Here by relative power, we mean each measured curve (power of transmitted wave mode) is normalized by its own maximum in the angle scan range. The angle of incidence has been converted with respect to the free-space (since all the angles are measured in air). The theoretical results are also plotted in the same figure in terms of relative power. As it is seen, the measured and predicted results agree very well except for the location of the minimum of the 0-order mode. This is probably due to the effect of the air-dielectric interfaces of the actual hologram (we'll look at this effect in the following chapter). It is also noted that the measured maximum for the –1-order and the minimum for the 0-order do not occur at the same angle of incidence, as in the predicted results (also see Fig.3.7a). The–1-order has less measured data than the 0-order mode because of the angle scan limit (for an incident angle of 50^0, the corresponding diffraction angle is about 64^0, which is already the end of the rail in Fig.7.4).

Then, a TM polarized read-out beam is used as the incident wave for the single-grating hologram and the receiving horn antenna is also set in the TM polarization (where the *H*-field is perpendicular to the plane of incidence). The measurement is repeated for this TM setup and the results are shown in Fig.7.7. Again, each curve is normalized by their respective maximum and the vertical axis is in dB scale. As see in the figure, the measured and predicted results show a good agreement for the –1-order diffracted mode, but they have a considerable difference on the minimum of the 0-order transmitted mode. In addition to the effect of air-dielectric interfaces, the use of Gaussian beam with a finite beam width and amplitude profile could be another cause for the deviation, since the theory assumes an infinite uniform plane wave incidence.

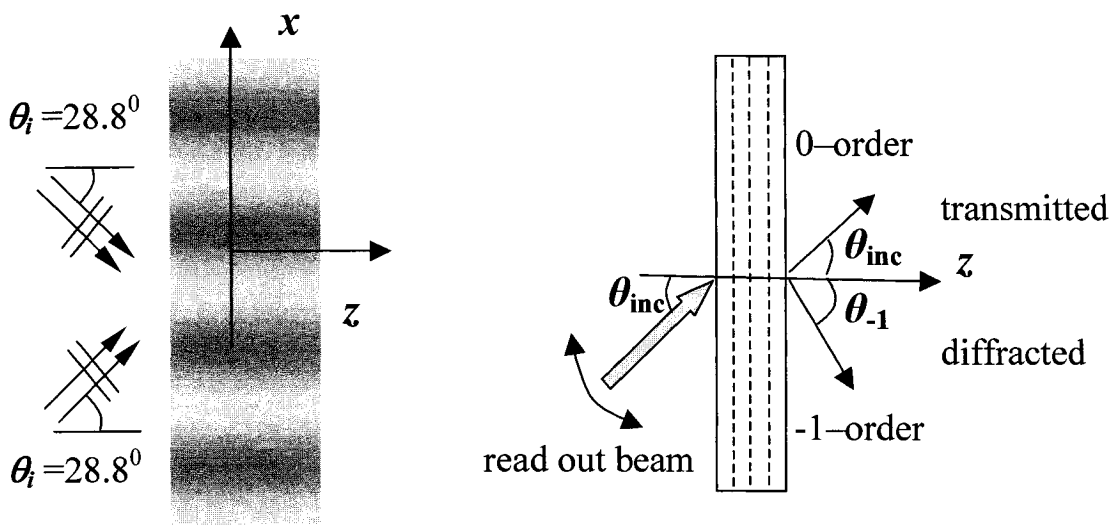

(a) recording stage (b) reconstructing stage

Fig.7.5 The measurement corresponding to the reconstruction stage (single-grating AMVH).

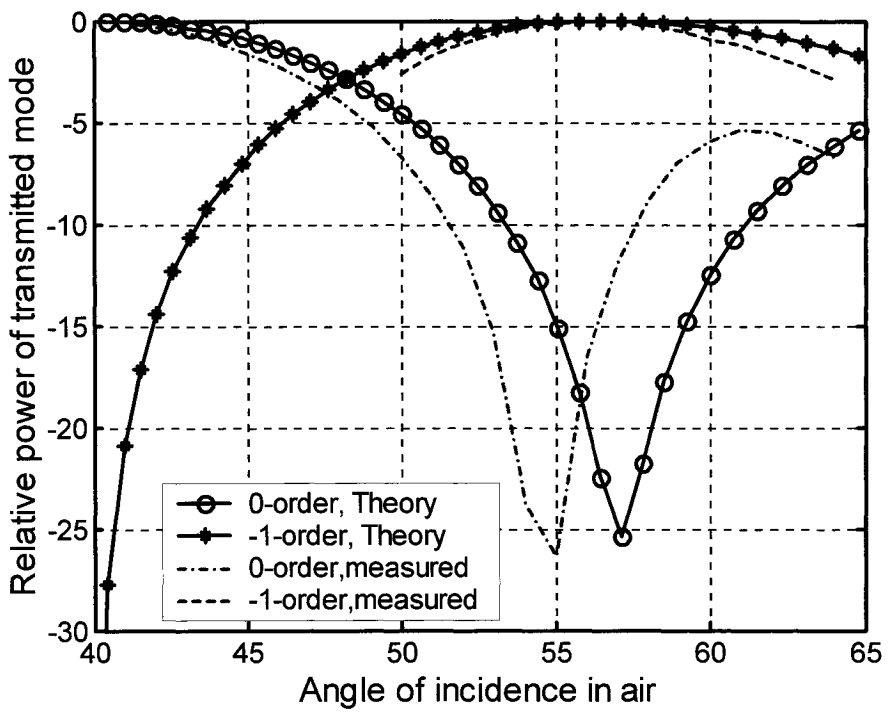

Fig.7.6 Measured relative powers (dB) of the direct transmission (0-order) and diffraction (−1-order) waves by a TE read-out beam for the single-grating AMVH.

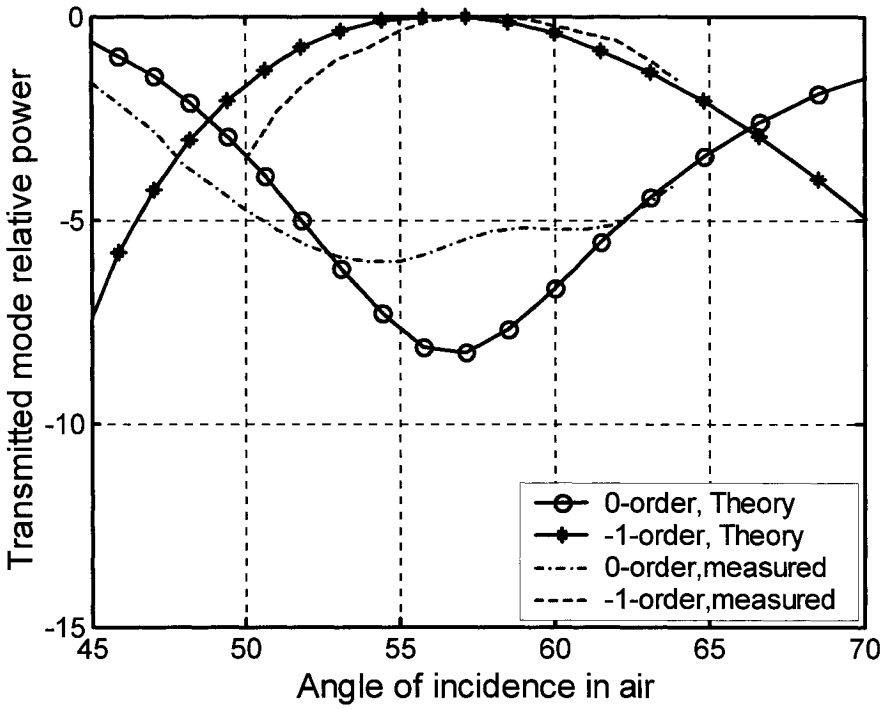

Fig.7.7 Measured relative powers (dB) of the direct transmission (0-order) and diffraction (−1-order) waves by a TM read-out beam for the single-grating AMVH.

The multiplex AMVHs fabricated are all measured under the TE incidence and receiving. The angle step is one degree in the incident angle scan (same as for the single-grating AMVH). For the first multiplex hologram (see the parameters in Table 7.2), within the angle scan range there are mainly two propagating wave modes, the 0-order and −1-order modes. The +1-order and −2-order modes appear only at a few angles close to the end of the scan range. The measured relative powers are shown in Fig.7.8 in dB scale, along with the analysis results. Again, a very good agreement between the measured and the analysis results are observed for the −1-order mode, while the trends from the measurement and analysis are consistent for the 0-order mode, though there is a deviation.

The second multiplex AMVH implemented is actually an aperiodic structure as the two holographic gratings used are not commensurate. Its parameters are given in Table 7.2. This aperiodic structure can be approximated by a periodic one as discussed in Sec.6.1.2.

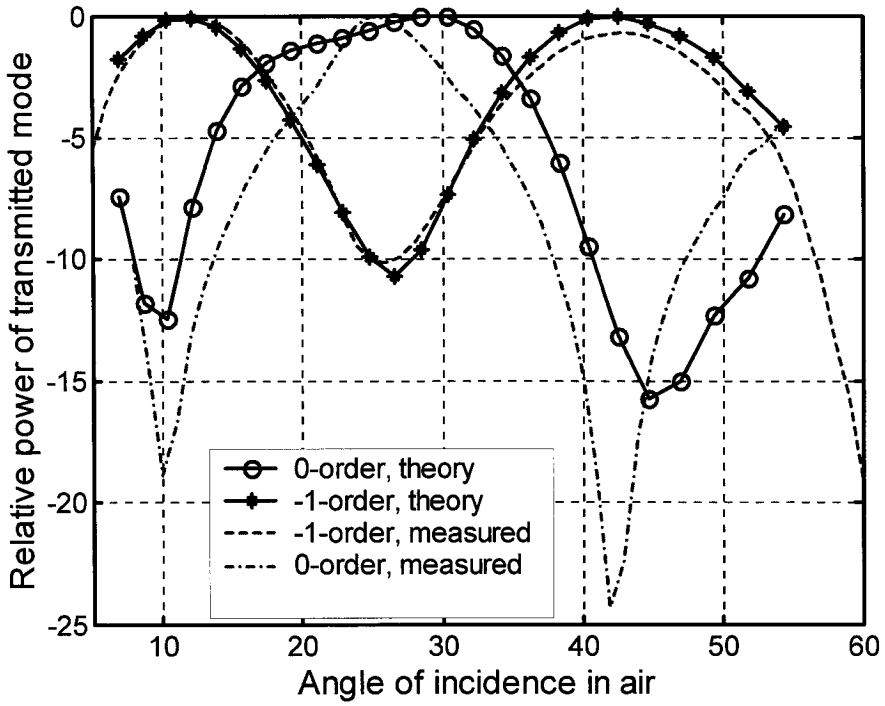

Fig.7.8 Measured relative powers (dB) of transmitted wave modes (0-order and −1-order) under a TE read-out beam incidence for the multiplex AMVH #1.

The periodic approximation has the similar recording beam configuration as in Fig.6.6, but with the following parameters

$\varphi_1 = \varphi_2 = 24.6^0$, $\varphi_{2'} = -\varphi_{1'} = 7.98^0$, $\varepsilon_a = 3.76$, $\varepsilon_{d1} = \varepsilon_{d2} = 0.38$, $\varepsilon_H = 3.0$, $f = 30\,\text{GHz}$,

Those recording beam angles that are measured in the host dielectric correspond to 46.2^0 and $\pm 13.9^0$ in air, which are the approximation of the actual recording beam angles 45^0 and $\pm 10^0$. The period will be 20.8mm and lattice constants are the same as in the example in Sec.6.1.2. By assuming the actual multiplex hologram has such periodicity, the possible propagating modes in the transmitted and reflected fields within the angle range of incidence are found to be from the −5-order to the +5 order, and their propagation directions can be determined from (6-5). Among the 11 propagating modes, the first four orders, i.e. the 0-, −1-, −2-, and +1-orders, contribute more than 90% of the total transmitted field, and are therefore measured and compared with the analysis; while the rest higher orders are insignificant.

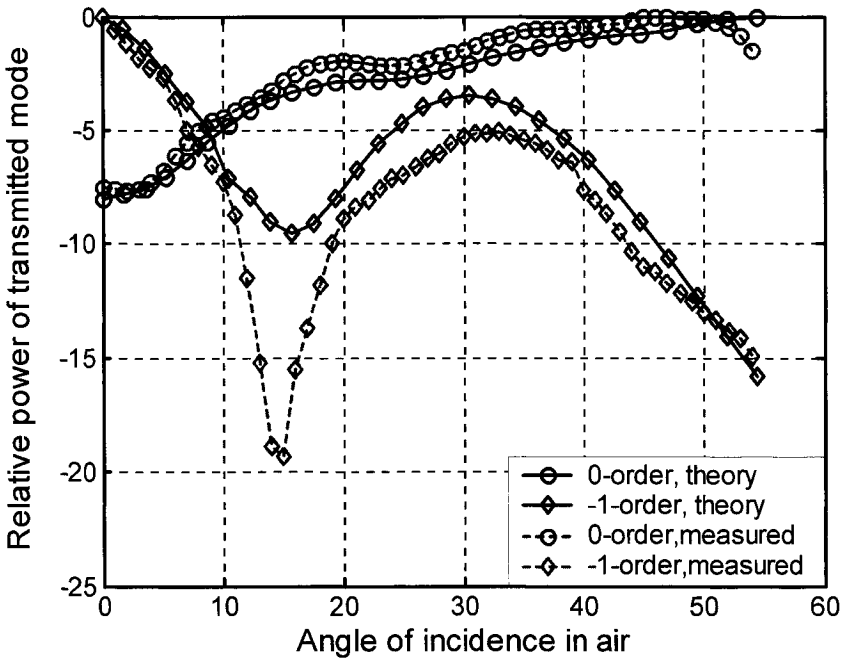

(a)

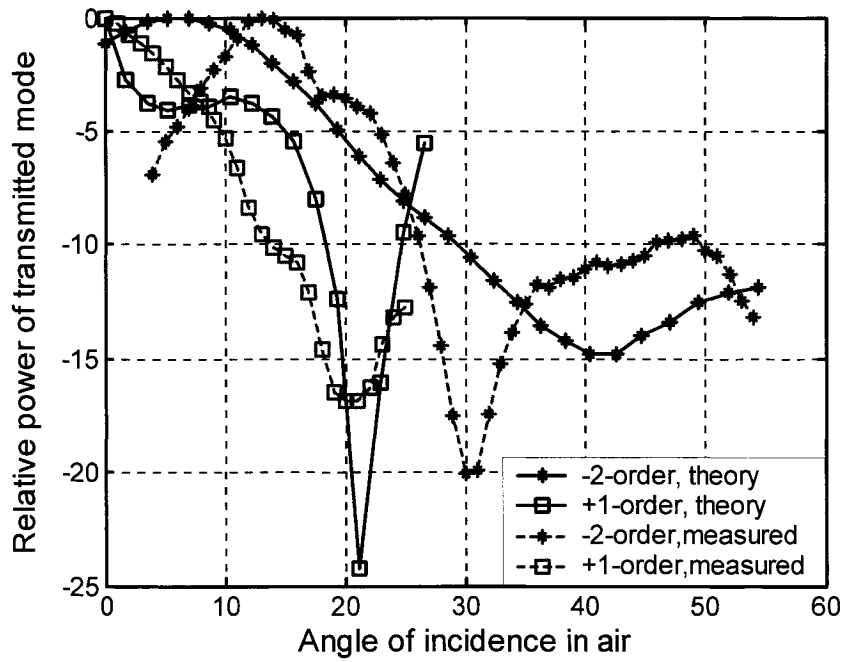

(b)

Fig.7.9 Measured relative powers (dB) of transmitted wave modes for the multiplex AMVH #2 (a) 0-order and −1-order, (b) −2-order and +1-order.

Figure 7.9 gives the measured results in terms of relative powers on the actual multiplex AMVH #2, along with the theoretical results based on the approximate periodic multiplex AMVH. Again, The higher order (+1-order) has less measured data because of the angle scan limit. As it is seen, for the lower orders (Fig.7.9a), agreement between the measurement and the analysis is quite good. As the order goes higher, the deviation between the measurement and the analysis becomes more evident (Fig.7.9b). The cause of such deviation reflects the essential difference between periodic and aperiodic structures. From Table 7.2, we see the original multiplex AMVH has Bragg angles at 45^0 and $\pm 10^0$ (the recording beam angles), while from the last paragraph the approximate (periodic) multiplex AMVH has the Bragg angles at 46.2^0 and $\pm 13.9^0$ and a period of 20.8mm. To make the approximate AMVH's Bragg angles closer to the actual AMVH's will result in a larger period and thus more propagating modes. In the limit of the approximate AMVH's Bragg angles approaching the real ones, its period tends to infinite large. In other words, the actual aperiodic AMVH can be considered as a special "periodic" AMVH, whose period is infinite large, and thus it allows an infinite number of propagating modes, which eventually comprise a continuous spectrum. In the measurement, at each angle the receiver actually picks up the modes within a small spectrum range around that angle, instead of a single order mode.

A preliminary design and measurement of a square-patch single-grating hologram have also been carried out. It consists of 51 layers with a recording beam angle of 55^0 (in air). The measurement results are given in Fig.7.10 for the 0-order wave mode, along with the predicted results. As it's seen, the designed square-patch hologram doesn't meet the expectation (in terms of attenuation of the 0-order mode at the Bragg angle). But it does better than a disk-patch hologram using same number of layers and patch sizes, according to the prediction. One of the causes for the deviation between the measured and predicted results could be the corner rounding effect during the etching process (one actually obtains a round corner with certain radius instead of a ideal sharp corner with zero radius). It is known that sharp corners contribute a good percentage of the total polarizability of the patch. Another factor is that the polarizability formula (5-10) used for square patches is valid only

for static or very low frequency cases, compared to equation (3-17) for circular patches, which is valid up to the third order of *kd*.

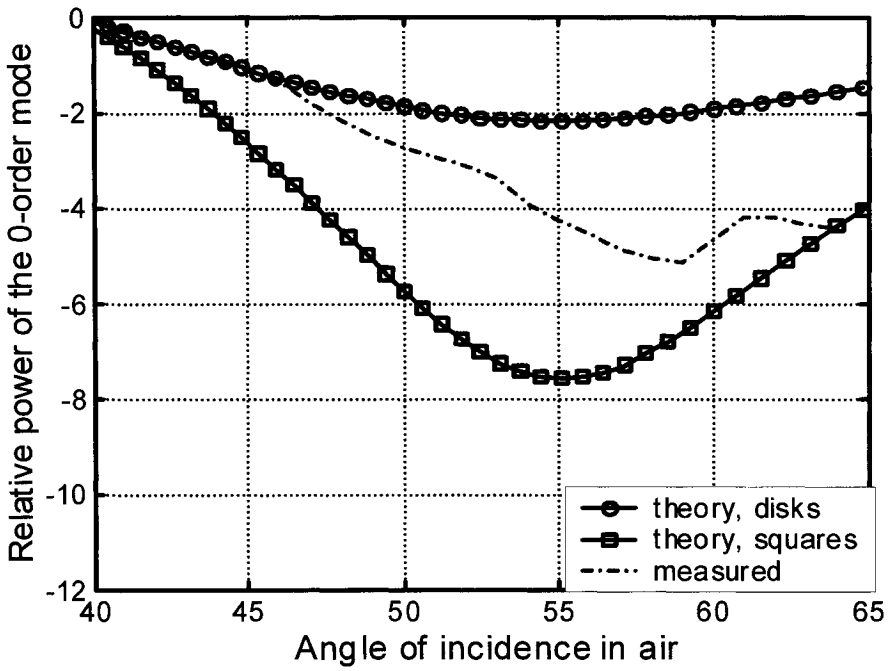

Fig.7.10 Relative power (dB) of the 0-order mode, measured and predicted. (Both predicted results use 51 layers, but with disk and square patches of same size, respectively.)

7.4 Chapter summary and remarks

There are many factors that could contribute to the deviation between the measured result and the predicted result. In general, different conditions used in the measurement and in the simulation should be the main cause for the deviations, such as (i) a Gaussian beam with a finite beam width and amplitude profile used in the measurement versus an infinite uniform plane wave used in the theory, (ii) existence of air-dielectric interfaces in the actual holograms versus infinite large host medium in the ideal AMVH models, and so on.

It is also observed during the measurements of the above AMVHs that at large angle of incidence ($>\sim 52^0$) the beam starts hitting the edge of the holograms (both the single-

grating and multiplex holograms), which may cause certain edge diffraction. If the Bragg angle of an AMVH falls in this angle region, the edge diffraction effect could become significant. Another note needs to be mentioned is that the wave-front of the incident beam may not be considered as flat if a hologram is relative thick so that the distance between the center plane and the front surface is not ignorable.

Nevertheless, the self-consistent dynamic-dipole-interaction theory (DDIT) has been, in general, confirmed by the measurements for both the single-grating and multiplex AMVHs. To eliminate the effects due to the finite beam width and the non-uniform beam profile a plane wave near-field measurement setup is proposed in chapter 10 as a suggestion for the future research.

Chapter 8

AMVHs in finite-thickness dielectric slabs: the effect of the air-dielectric interfaces

In the previous chapters, AMVHs are treated as cascades of planar conduction patch lattices in an infinite large dielectric host medium. This ideal situation eliminates the interference associated with the air-dielectric interfaces and enables us to focus on the under-line physics of AVMHs. Since in practice, AMVHs have to be made in finite-thickness dielectric slabs, we will discuss in this chapter how the theory can be extended to include the boundary effect. Numerical results will be presented in comparison with measurements and with some known results.

8.1 Transmission and reflection at interfaces: the wave matrix method

Consider the transmission and reflection problem at an interface of two dielectric half spaces of different parameters, as shown in Fig.8.1. To address the problem generally, oblique plane wave incidences from region I to region II and from region II to region I at angles of θ_1 and θ_2, respectively, are assumed, where the angles meet the Snell's law,

$$\sqrt{\varepsilon_1}\sin\theta_1 = \sqrt{\varepsilon_2}\sin\theta_2 \tag{8-1}$$

Under these incidences, all the transmitted and reflected waves in the same region will have the same direction and thus can be summed algebraically. After neglecting the phasors, the amplitudes of the waves propagating away from the interface in both sides can be written as

$$\begin{aligned} c_2 &= T_{12}c_1 + R_{21}b_2 \\ b_1 &= R_{12}c_1 + T_{21}b_2 \end{aligned} \tag{8-2}$$

Here, c_i is used for the amplitudes of right-traveling waves and b_i for the amplitudes of left-traveling waves.

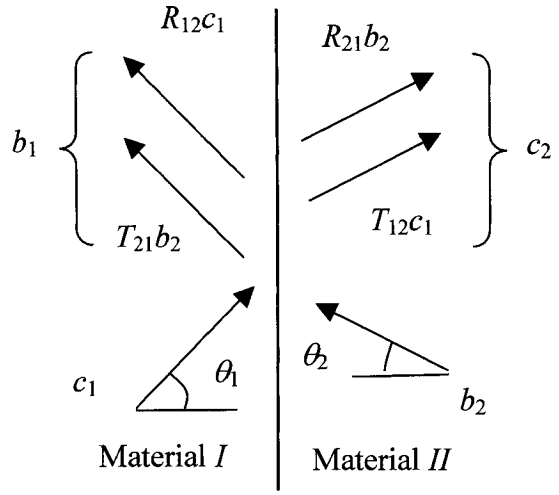

Fig.8.1 Transmission and reflection through an interface.

The transmission and reflection coefficients are given by

$$T_{12} = \frac{2Z_2}{Z_1 + Z_2}, \quad T_{21} = \frac{2Z_1}{Z_1 + Z_2}, \quad R_{12} = -R_{21} = \frac{Z_2 - Z_1}{Z_1 + Z_2}, \tag{8-3}$$

where $Z_{1,2}$ are the normalized impedances of the material I and II, respectively, by the free-space impedance at the given propagating direction. Equation (8-2) can be rewritten in a matrix format as

$$\begin{pmatrix} c_1 \\ b_1 \end{pmatrix} = \frac{1}{T_{12}} \begin{bmatrix} 1 & R_{12} \\ R_{12} & 1 \end{bmatrix} \begin{pmatrix} c_2 \\ b_2 \end{pmatrix} = \frac{1}{2} \begin{bmatrix} 1 + Z_1/Z_2 & 1 - Z_1/Z_2 \\ 1 - Z_1/Z_2 & 1 + Z_1/Z_2 \end{bmatrix} \begin{pmatrix} c_2 \\ b_2 \end{pmatrix} \tag{8-4}$$

where the wave amplitudes that are related to one material region appear only in one side of the equation. This is the key feature of the so called "wave-transmission matrix method" (or simply the "wave matrix method") proposed by Collin [20], which allows for a simple matrix product expression for cascaded multiple layer structures. Let's consider the typical case of a finite-thickness (t_2) dielectric slab in the free space (or in air), as shown in Fig.8.2. The wave amplitudes in free-space regions in both sides of the slab can be expressed as

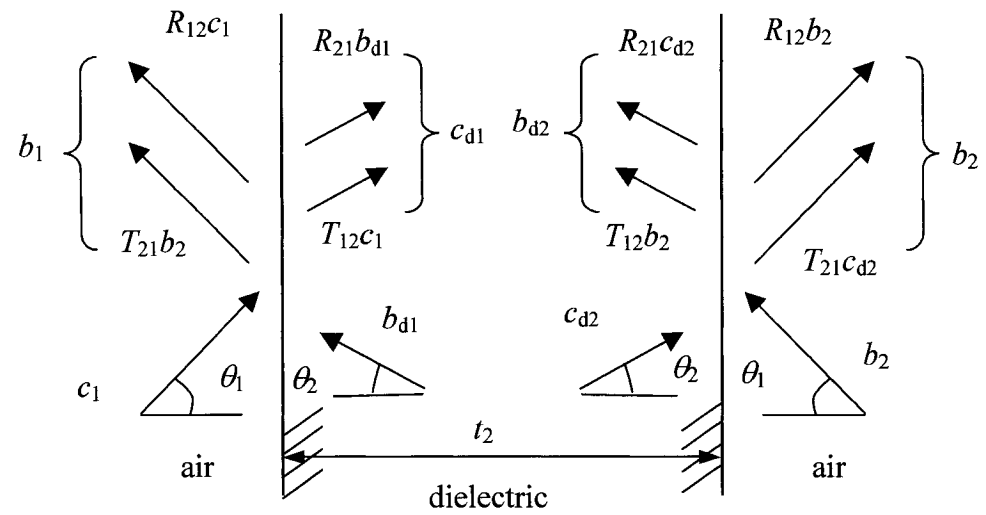

Fig.8.2 Transmission and reflection through a dielectric slab.

$$\begin{pmatrix} c_1 \\ b_1 \end{pmatrix} = \frac{1}{2}\begin{bmatrix} 1+Z_2^{-1} & 1-Z_2^{-1} \\ 1-Z_2^{-1} & 1+Z_2^{-1} \end{bmatrix}\begin{pmatrix} c_{d1} \\ b_{d1} \end{pmatrix} = \frac{1}{2}\begin{bmatrix} 1+Z_2^{-1} & 1-Z_2^{-1} \\ 1-Z_2^{-1} & 1+Z_2^{-1} \end{bmatrix}\begin{bmatrix} e^{j\delta_d} & 0 \\ 0 & e^{-j\delta_d} \end{bmatrix}\begin{pmatrix} c_{d2} \\ b_{d2} \end{pmatrix}$$
$$= \frac{1}{4}\begin{bmatrix} 1+Z_2^{-1} & 1-Z_2^{-1} \\ 1-Z_2^{-1} & 1+Z_2^{-1} \end{bmatrix}\begin{bmatrix} e^{j\delta_d} & 0 \\ 0 & e^{-j\delta_d} \end{bmatrix}\begin{bmatrix} 1+Z_2 & 1-Z_2 \\ 1-Z_2 & 1+Z_2 \end{bmatrix}\begin{pmatrix} c_2 \\ b_2 \end{pmatrix} \tag{8-5}$$

where δ_d is the electrical distance between the dielectric slab boundaries at the given propagating direction. When the external incident wave is only from left-hand side in the Fig.8.2 (i.e., $b_2 = 0$), then the classical transmission and reflection coefficients for a dielectric slab can be re-obtained from (8-5) in an explicit format,

$$T_{slab} \equiv \frac{c_2}{c_1} = \frac{1}{\cos\delta_d + j\sin\delta_d (Z_2 + Z_2^{-1})/2},$$
$$R_{slab} \equiv \frac{b_1}{c_1} = \frac{j\sin\delta_d (Z_2 - Z_2^{-1})/2}{\cos\delta_d + j\sin\delta_d (Z_2 + Z_2^{-1})/2}. \tag{8-6}$$

with $\delta_d = t_2 k_2 \cos\vartheta_2$.

The wave matrix method can also be used in other types of cascade connections, such as transmission lines, waveguides, etc. It is not difficult to find out the relations of the wave matrix with other matrices such as the scattering matrix.

8.2 Multi-mode wave matrix method

The original wave matrix method can only be applied to cascades of uniform sections with single mode propagation and evanescent modes being ignored. Effort has been made to extend the method to the cases of multiple-layer disk lattices by equating each planar lattice of uniform disks to a shunt impedance in terms of the transmission line theory [59-61]. However, this extension still requires successive lattice planes being apart far enough to exclude the effects of evanescent modes. This is, unfortunately, not the case for the artificial microwave volume holograms (AMVHs) discussed in this thesis, where the spacing of any two successive planar lattice planes is much smaller than the wavelength used, and thus the interactions of evanescent modes have to be considered.

In the following discussion, we'll consider an AMVH as an entire structure instead of individual disk lattice planes. In this way, the interactions of evanescent modes have automatically been taken care of by the self-consistent dynamic-dipole-interaction-theory as part of the internal interactions of the AMVH structure. Then, the interaction between the entire AMVH structure and the external world will be described by the wave matrices. In order to do so, it is required that the AMVH structure be characterized by the wave matrices as a whole. This can be done by examining the scattered far fields of the AMVH as in Sub-sec.3.2.3 and (3-18). Let's consider for simplicity the single-grating AMVH case, where only two propagating modes exist in the scattered far fields, i.e., the 0-order and –1-order modes, as shown in Fig.8.3. The wave mode amplitudes are denoted by $c_{n,m}$ and $b_{n,m}$, with the first subscript representing the terminal plane number and the second, the mode number. By analogy with and following the convention of the wave matrix method for the single wave case as seen in the previous section, we can write down the following relations

$$
\begin{aligned}
c_{2,1} &= T_{11}e^{-j\delta_1}c_{1,1} + R_{11}b_{2,1} + T_{12}e^{-j\delta_1}c_{1,2} + R_{12}b_{2,2} \\
b_{1,1} &= R_{11}c_{1,1} + T_{11}e^{-j\delta_1}b_{2,1} + R_{12}c_{1,2} + T_{12}e^{-j\delta_1}b_{2,2} \\
c_{2,2} &= T_{21}e^{-j\delta_2}c_{1,1} + R_{21}b_{2,1} + T_{22}e^{-j\delta_2}c_{1,2} + R_{22}b_{2,2} \\
b_{1,2} &= R_{21}c_{1,1} + T_{21}e^{-j\delta_2}b_{2,1} + R_{22}c_{1,2} + T_{22}e^{-j\delta_2}b_{2,2}
\end{aligned}
\qquad \text{(8-7a,b,c,d)}
$$

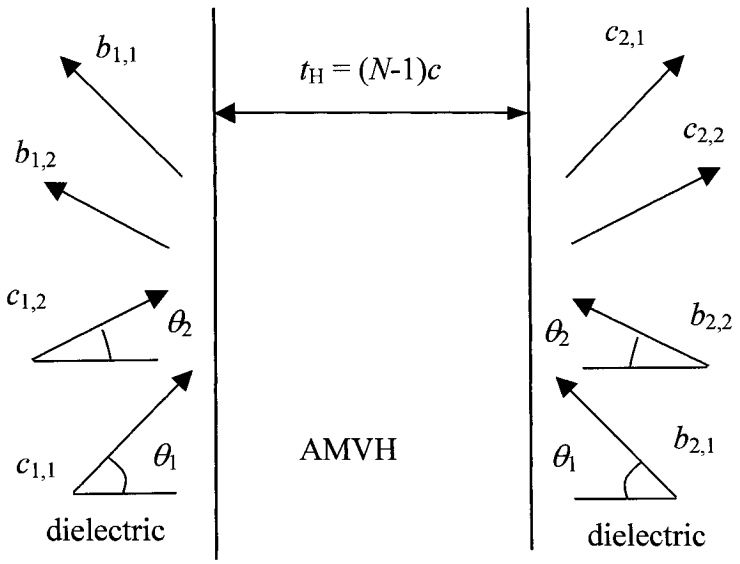

Fig.8.3 The forward- and backward- scattered waves by an AMVH, a case with two propagating modes.

where T_{mm} and R_{mm} are the respective transmission and reflection coefficients of the mth mode, T_{mn} and R_{mn} ($m \neq n$) are the respective forward- and backward- diffraction coefficients from the nth mode to the mth mode, and δ_m is the electrical distance for the mth mode to travel through the hologram. Expression for those coefficients can be found from (3-18) of Sub-sec.3.2.3. Use has also been made of the reciprocity principle [53] to obtain relations (8-7). From (8-7a) and (8-7c), we can solve for $c_{1,1}$ and $c_{1,2}$ as

$$\begin{pmatrix} c_{1,1} \\ c_{1,2} \end{pmatrix} = \begin{bmatrix} \overline{T}_{11} & \overline{T}_{12} \\ \overline{T}_{21} & \overline{T}_{22} \end{bmatrix}^{-1} \left(\begin{pmatrix} c_{2,1} \\ c_{2,2} \end{pmatrix} - \begin{bmatrix} R_{11} & R_{12} \\ R_{21} & R_{22} \end{bmatrix} \begin{pmatrix} b_{2,1} \\ b_{2,2} \end{pmatrix} \right),$$

with (8-8)

$$\overline{T}_{mn} = T_{mn} e^{-j\delta_m}.$$

Equations (8-7b) and (8-7d) can be expressed as

$$\begin{pmatrix} b_{1,1} \\ b_{1,2} \end{pmatrix} = \begin{bmatrix} R_{11} & R_{12} \\ R_{21} & R_{22} \end{bmatrix} \begin{pmatrix} c_{1,1} \\ c_{1,2} \end{pmatrix} + \begin{bmatrix} \overline{T}_{11} & \overline{T}_{12} \\ \overline{T}_{21} & \overline{T}_{22} \end{bmatrix} \begin{pmatrix} b_{2,1} \\ b_{2,2} \end{pmatrix}, \quad (8\text{-}9)$$

From (8-9) and (8-8), equation (8-7) can be rewritten in a matrix format as

$$\begin{bmatrix} c_{1,1} \\ c_{1,2} \\ b_{1,1} \\ b_{1,2} \end{bmatrix} = \begin{bmatrix} [\bar{T}]^{-1} & -[\bar{T}]^{-1}[R] \\ [R][\bar{T}]^{-1} & [\bar{T}]-[R][\bar{T}]^{-1}[R] \end{bmatrix} \begin{bmatrix} c_{2,1} \\ c_{2,2} \\ b_{2,1} \\ b_{2,2} \end{bmatrix},$$

with (8-10)

$$[\bar{T}] = \begin{bmatrix} \bar{T}_{11} & \bar{T}_{12} \\ \bar{T}_{21} & \bar{T}_{22} \end{bmatrix}, \quad [R] = \begin{bmatrix} R_{11} & R_{12} \\ R_{21} & R_{22} \end{bmatrix}.$$

Equation (8-10) is a generalized two-wave version of the original wave matrix expression of (8-5), and is a wave matrix representation of an AMVH structure that supports two propagating modes. It is noted that the wave amplitudes in both sides of the equation are measured within the host dielectric medium of the AMVH at the locations of the first and last lattice planes. At the boundaries (=air-dielectric interfaces) of the AMVH, these amplitudes then need to be converted into those corresponding to the free-space by using the wave matrix relation similar to (8-2). Assuming the left boundary (interface) has a distance of t_L to the first lattice plane and the right boundary (interface) has a distance of t_R to the last lattice plane (they are also called the "buffer" hereafter). The wave matrix representation of the interfaces for the two modes can be written as

$$\begin{pmatrix} c_i^L \\ b_i^L \end{pmatrix} = \frac{1}{T_{a,d}^i} \begin{bmatrix} 1 & R_{a,d}^i \\ R_{a,d}^i & 1 \end{bmatrix} \begin{bmatrix} e^{j\delta_L^i} & 0 \\ 0 & e^{-j\delta_L^i} \end{bmatrix} \begin{pmatrix} c_{1,i} \\ b_{1,i} \end{pmatrix}, \quad i = 1,2 \tag{8-11}$$

for the left interface and

$$\begin{pmatrix} c_{2,i} \\ b_{2,i} \end{pmatrix} = \frac{1}{T_{d,a}^i} \begin{bmatrix} e^{j\delta_R^i} & 0 \\ 0 & e^{-j\delta_R^i} \end{bmatrix} \begin{bmatrix} 1 & R_{d,a}^i \\ R_{d,a}^i & 1 \end{bmatrix} \begin{pmatrix} c_i^R \\ b_i^R \end{pmatrix}, \quad i = 1,2 \tag{8-12}$$

for the right interface. In the above equations, $T_{a,d}^i$ and $R_{a,d}^i$ ($T_{d,a}^i$ and $R_{d,a}^i$) are the corresponding transmission and reflection coefficients for the ith wave mode propagating from the air to the host dielectric (from the host dielectric to the air), and δ_L^i and δ_R^i are the corresponding ith mode's electrical distances of the left and righter buffers. Equations (8-11) and (8-12) can also be expressed in 4x4 matrix format

$$\begin{bmatrix} c_1^L \\ c_2^L \\ b_1^L \\ b_2^L \end{bmatrix} = \begin{bmatrix} \frac{e^{j\delta_L^1}}{T_{a,d}^1} & 0 & \frac{R_{a,d}^1}{T_{a,d}^1} e^{-j\delta_L^1} & 0 \\ 0 & \frac{e^{j\delta_L^2}}{T_{a,d}^2} & 0 & \frac{R_{a,d}^2}{T_{a,d}^2} e^{-j\delta_L^2} \\ \frac{R_{a,d}^1}{T_{a,d}^1} e^{j\delta_L^1} & 0 & \frac{e^{-j\delta_L^1}}{T_{a,d}^1} & 0 \\ 0 & \frac{R_{a,d}^2}{T_{a,d}^2} e^{j\delta_L^2} & 0 & \frac{e^{-j\delta_L^2}}{T_{a,d}^2} \end{bmatrix} \begin{bmatrix} c_{1,1} \\ c_{1,2} \\ b_{1,1} \\ b_{1,2} \end{bmatrix}, \tag{8-13}$$

and

$$\begin{bmatrix} c_{2,1} \\ c_{2,2} \\ b_{2,1} \\ b_{2,2} \end{bmatrix} = \begin{bmatrix} \frac{e^{j\delta_R^1}}{T_{d,a}^1} & 0 & \frac{R_{d,a}^1}{T_{d,a}^1} e^{j\delta_R^1} & 0 \\ 0 & \frac{e^{j\delta_R^2}}{T_{d,a}^2} & 0 & \frac{R_{d,a}^2}{T_{d,a}^2} e^{j\delta_R^2} \\ \frac{R_{d,a}^1}{T_{d,a}^1} e^{-j\delta_R^1} & 0 & \frac{e^{-j\delta_R^1}}{T_{d,a}^1} & 0 \\ 0 & \frac{R_{d,a}^2}{T_{d,a}^2} e^{-j\delta_R^2} & 0 & \frac{e^{-j\delta_R^2}}{T_{d,a}^2} \end{bmatrix} \begin{bmatrix} c_1^R \\ c_2^R \\ b_1^R \\ b_2^R \end{bmatrix}, \tag{8-14}$$

Now, one can cascade equations (8-13), (8-10), and (8-14) to obtain the final wave matrix equation relating the wave amplitudes in the left-side free space (air) of the AMVH to those in the right-side free space (air)

$$\begin{bmatrix} c_1^L \\ c_2^L \\ b_1^L \\ b_2^L \end{bmatrix} = \begin{bmatrix} [T_{a,d}^+] & [RT_{a,d}^-] \\ [RT_{a,d}^+] & [T_{a,d}^-] \end{bmatrix} \begin{bmatrix} [\bar{T}]^{-1} & -[\bar{T}]^{-1}[R] \\ [R][\bar{T}]^{-1} & [\bar{T}]-[R][\bar{T}]^{-1}[R] \end{bmatrix} \begin{bmatrix} [T_{d,a}^+] & [RT_{d,a}^+] \\ [RT_{d,a}^-] & [T_{d,a}^-] \end{bmatrix} \begin{bmatrix} c_1^R \\ c_2^R \\ b_1^R \\ b_2^R \end{bmatrix},$$

with $[T_{\alpha,\beta}^{\pm}] = \begin{bmatrix} \frac{e^{\pm j\delta_\gamma^1}}{T_{\alpha,\beta}^1} & 0 \\ 0 & \frac{e^{\pm j\delta_\gamma^2}}{T_{\alpha,\beta}^2} \end{bmatrix}$, $[RT_{\alpha,\beta}^{\pm}] = \begin{bmatrix} \frac{R_{\alpha,\beta}^1}{T_{\alpha,\beta}^1} e^{\pm j\delta_\gamma^1} & 0 \\ 0 & \frac{R_{\alpha,\beta}^2}{T_{\alpha,\beta}^2} e^{\pm j\delta_\gamma^2} \end{bmatrix}$, (8-15)

$(\alpha,\beta,\gamma) = (a,d,L),(d,a,R).$

The above equation is a general form wave matrix equation including all possible incidences, transmissions and reflections. In practice, there is usually one incidence wave, say, from left side, impinging on an AMVH within a finite-thickness dielectric slab, and it is required to calculate all possible transmissions and reflections. In this case, we have

$$\begin{pmatrix} b_1^R \\ b_2^R \end{pmatrix} = \begin{pmatrix} 0 \\ 0 \end{pmatrix}, \quad \begin{pmatrix} c_1^L \\ c_2^L \end{pmatrix} = \begin{pmatrix} 1 \\ 0 \end{pmatrix} \tag{8-16a,b}$$

The general equation (8-15) then reduces to

$$\begin{pmatrix} 1 \\ 0 \end{pmatrix} = ([T_{a,d}^+][W_1] + [RT_{a,d}^-][W_2]) \begin{pmatrix} c_1^R \\ c_2^R \end{pmatrix},$$
$$\begin{pmatrix} b_1^L \\ b_2^L \end{pmatrix} = ([RT_{a,d}^+][W_1] + [T_{a,d}^-][W_2]) \begin{pmatrix} c_1^R \\ c_2^R \end{pmatrix}, \tag{8-17a,b}$$

where

$$[W_1] = [\bar{T}]^{-1}[T_{d,a}^+] - [\bar{T}]^{-1}[R][RT_{d,a}^-],$$
$$[W_2] = [R][\bar{T}]^{-1}[T_{d,a}^+] - ([\bar{T}] - [R][\bar{T}]^{-1}[R])[RT_{d,a}^-].$$

From (8-17), the transmission coefficients c_1^R, c_2^R and reflection coefficients b_1^L, b_2^L corresponding to the two wave modes can be determined.

8.3 Numerical results and comparison

First, to verify the formulism derived in the preceding section, we apply the method (equations (8-17)) to a case where a single planar lattice of small disks is embedded in a dielectric slab in free space. Because of the small disk sizes and only one planar lattice included in the slab, the results on transmission and reflection should be close to that obtained from (8-6) at f=30GHz for a pure dielectric slab in free space. Figure 8.4 shows the transmission and reflection coefficients versus the angle of incidence for a dielectric slab of 40.5mm with the planar disk lattice at the middle plane. As is seen, the results from the original wave matrix method and from the generalized wave matrix method overlap each other. The total energy efficiency calculated by either method is seen to be equal to one, which is the incident energy efficiency.

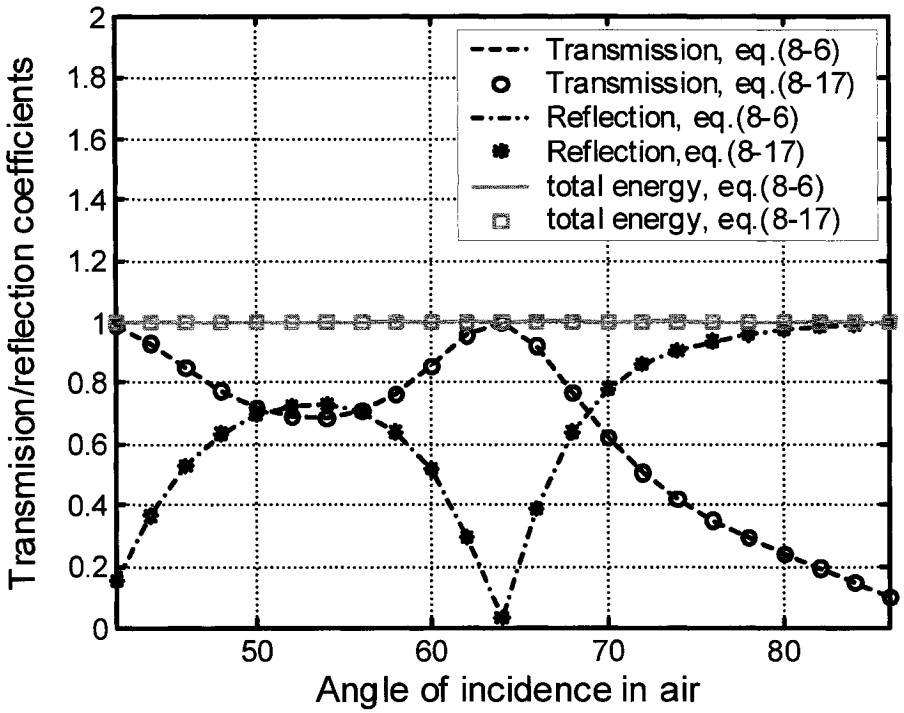

Fig.8.4 Comparison of transmission/reflection coefficients obtained using the original wave matrix method (8-6) and the generalized wave matrix method (8-17).

Then, we consider the single-grating AMVH discussed in Sec.3.4 as well as in Sec.7.3, but instead of an infinite host medium, consider it embedded in a finite dielectric slab with $0.02c$ and $1.0c$ left and right buffer distances (c=lattice layer thickness). Let a plane wave impinge on the AMVH slab from the left side free space at f=30GHz. The transmission and reflection mode amplitudes are calculated at each angle of incidence (in free space) and are plotted in Fig.8.5a,b. Compare Fig.8.5a with Fig.3.7a, it is seen the air-dielectric and dielectric-air interfaces do have some effect on the transmitted wave modes, but the main trend remains essentially the same, i.e., around the Bragg angle (55^0) the forward-scattered field is dominated by the diffraction (–1-order) mode. From Figs.8.5b and 8.4, the reflection is seen basically caused by the interfaces as the two cases used the same slab thickness, while the existence of the AMVH structure actually reduces the reflection somehow. Figure 8.6 presents the calculated energy efficiencies of various scattered waves, showing the total energy efficiency equal to one, the normalized energy efficiency of incident wave.

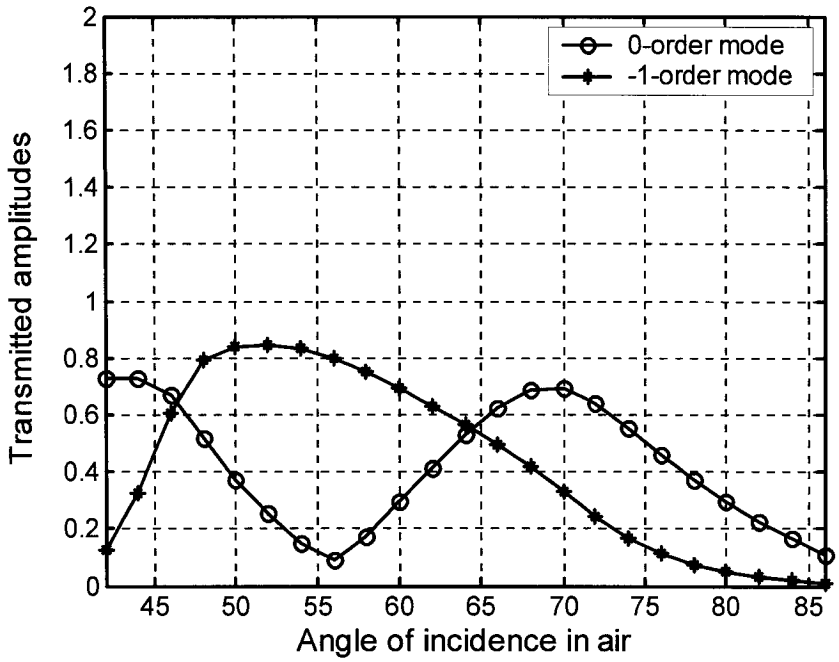

(a) Transmission

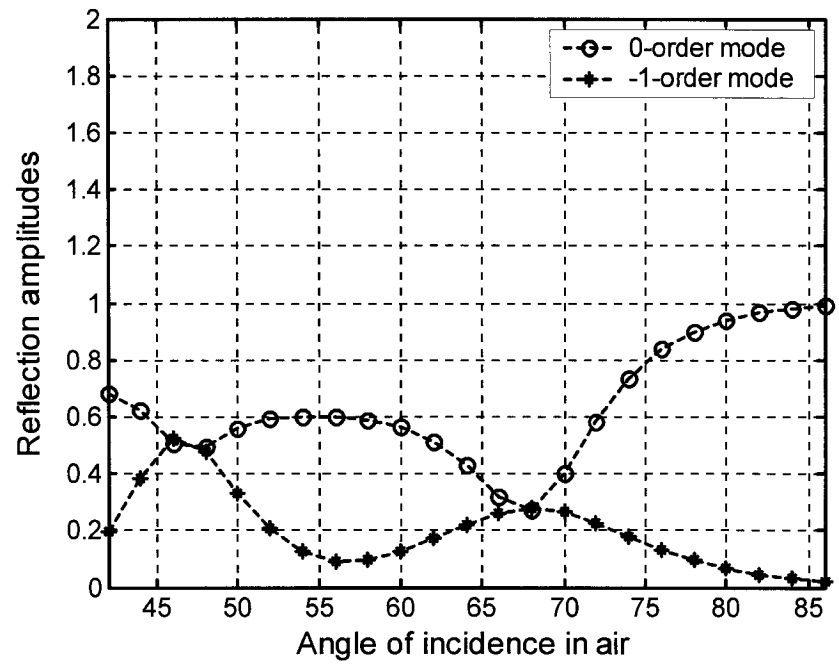

(b) Reflection

Fig.8.5 Transmission (a) and reflection (b) coefficients obtained by combining the dynamic-dipole-interaction-theory and the generalized wave matrix method (8-17).

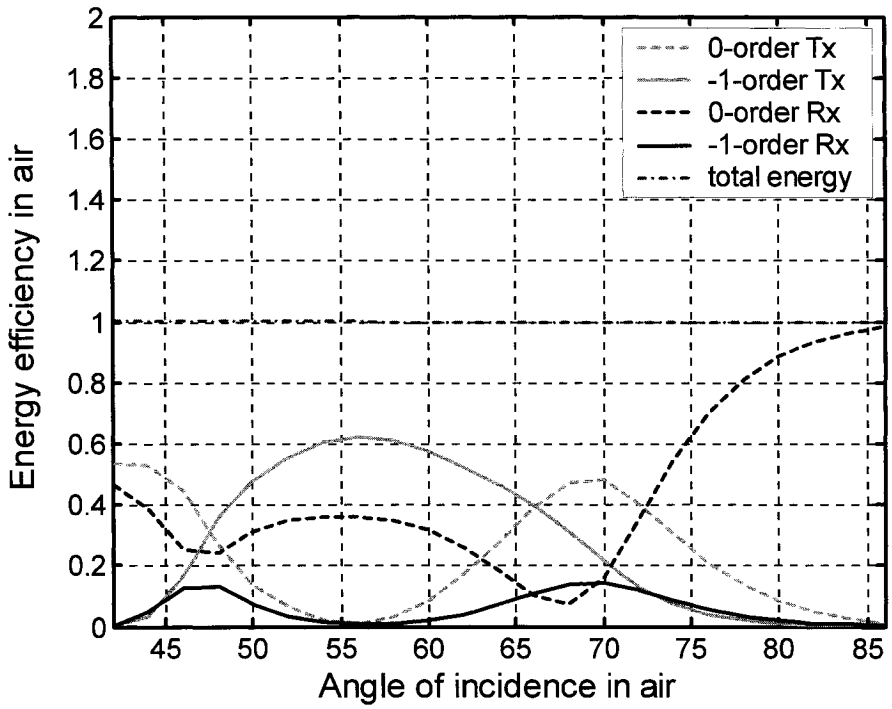

Fig.8.6 Energy efficiencies of the transmitted and the reflected waves from a finite-slab AMVH, under a TE plane wave incidence.

In figure 8.7, the calculated wave mode powers are re-plotted in dB scale and normalized by their respective maximum values. For comparison, the measurement results for the single-grating AMVH under TE incidence, which have been shown in Fig.7.6, are also re-plotted in the same figure. As is seen, by including the air-dielectric interfaces in the analysis, the predicted minima location for the 0-order mode is closer to the measured location, though the predicted minimum value (normalized) is somehow larger than the measured one. In general, the simulated results using the generalized wave matrix method show a better match with the measurement results on both curves (0-order and –1-order).

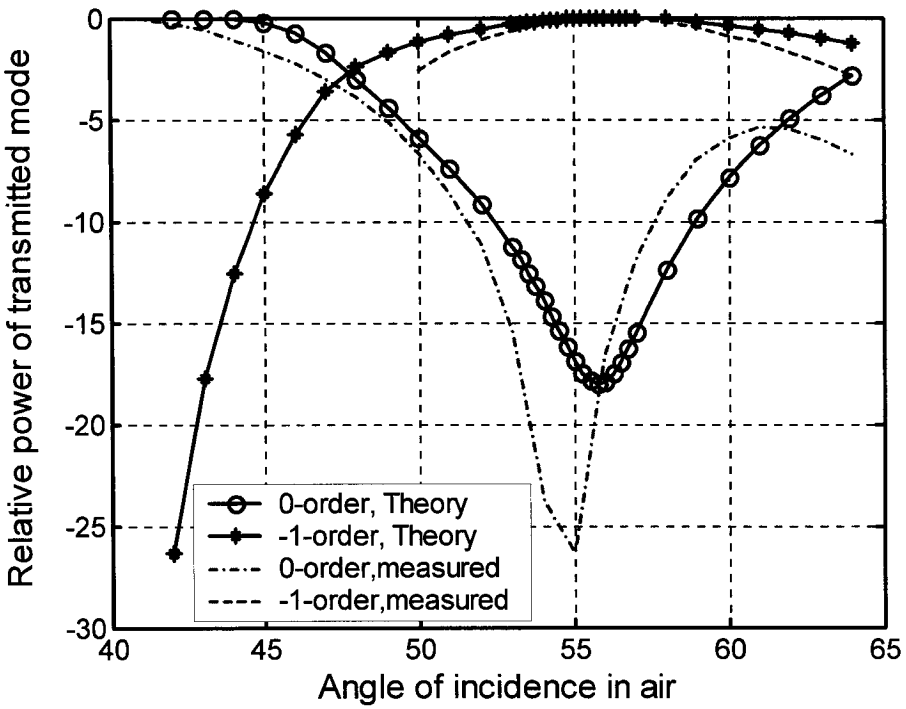

Fig.8.7 Measured and predicted relative powers of the forward-scattered beams (0-order and 1-order) by the single-grating AMVH using a TE read-out beam.

8.4 Chapter summary and remarks

A general multi-mode wave matrix method has been presented in this chapter to deal with the interface problems that occur when modeling the actual AMVHs using the DDIT. It can handle not only the air-dielectric interface, but also the dielectric-dielectric and the dielectric-conductor interfaces. The formulation is derived for the case of two-mode propagation within an AMVH, but can be readily extended to the general N-mode case. It should be noted that the method (as well as the conventional wave matrix method) is based on the homogeneous plane wave propagation, whereas, in the measurements, we face the problem of multiple reflections from the interfaces under context of Gaussian beam propagation. These different conditions may still cause the deviation between the measured and predicted results.

Chapter 9

Full-wave finite element verification of the self-consistent dynamic-dipole interaction theory

To further verify the theory described in the previous chapters for AMVHs, a full-wave finite element code, HFSS, is employed to simulate the multi-layer lattice structures of conducting patches, and to compare the results with those from this theory. The FEM simulation also tests the small-obstacle assumption used in the theory, and therefore provides a valid range of patch sizes where the assumption is not violated, or the application limit of the theory. In frequency domain FEM, although only a unit cell needs to be analyzed to simulate a 3D periodic structure, it is still a time-consuming process to model any of the AMVHs that have been designed previously, because of the large amount of patches contained in one unit cell. Thus, in this chapter, some simplified multi-layer lattice structures with less layers and uniform patch size are considered, for which the computer times of HFSS simulation are practically acceptable. These periodical structures are actually special cases of general AMVHs and can also be analyzed by our theory.

9.1 Numerical results on Electromagnetic Band-gap Structures (EBG)

When all patches in an AMVH become uniform, the hologram degenerates into a conventional multi-layer disk lattice structure, such as multi-layer FSSs, or electromagnetic band-gap structures (EBGs). First, consider an EBG structure consisting of multiple 2D rectangular lattices of uniform conducting disks. Its unit cell is shown in Fig.9.1, which has all the similar parameter definitions as in Fig.3.1, but with $I = 1$ for this case. The 3D disk array stands in free space and is excited by a plane wave normal incidence. In the HFSS simulation, we set a=b=1.2mm, c=2.6mm, d=0.56mm, N=30 (number of layers). A frequency sweeping of 40-80GHz at a step 0.5GHz is carried out, and the transmission and

reflection coefficients (or S parameters) are calculated. The results are plotted in Fig.9.2a,b against the dimensionless frequency (*kd*), along with the results from this theory.

As seen, the results from this theory (DDIT) match very well with those from HFSS simulation for this case. The transmission plot shows a typical band gap structure, where the reflection reaches its maximum. It is found from a parametric calculation that the depth of the band gap depends on the number of layers used, i.e., the more the layers, the deeper the band gap. It is also found changing the lattice plane spacing (or layer thickness) will result in the band gap position moving.

Next, we replace the disk patches in the above example by square patches of same size (edge length = *d*), meanwhile keep the lattice constants the same. Since square patch can provide high polarizability value (Chapter 5), it's expected that the same band-gap depth can be realized with fewer layers of square-patch lattices.

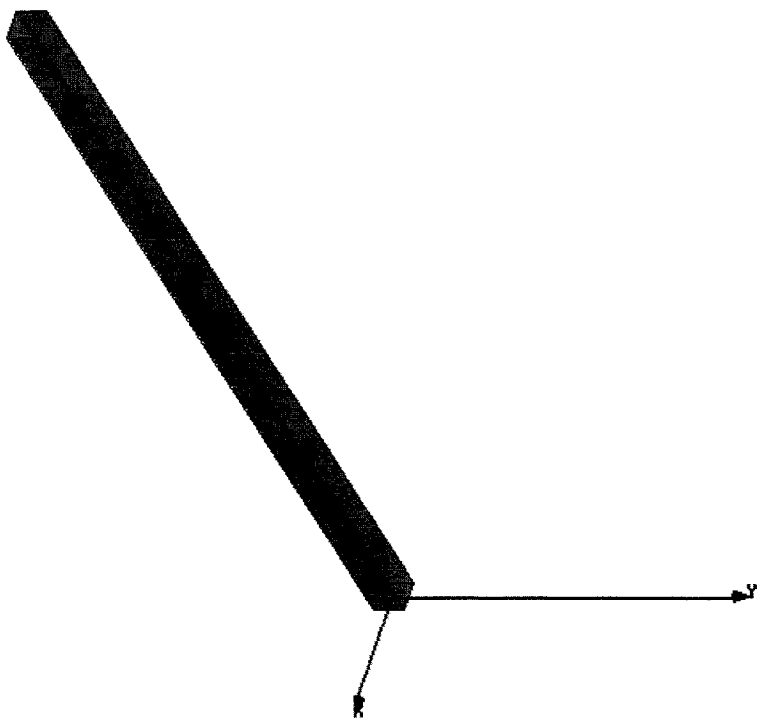

Fig.9.1 Unit cell of an EBG structure with disk patches.

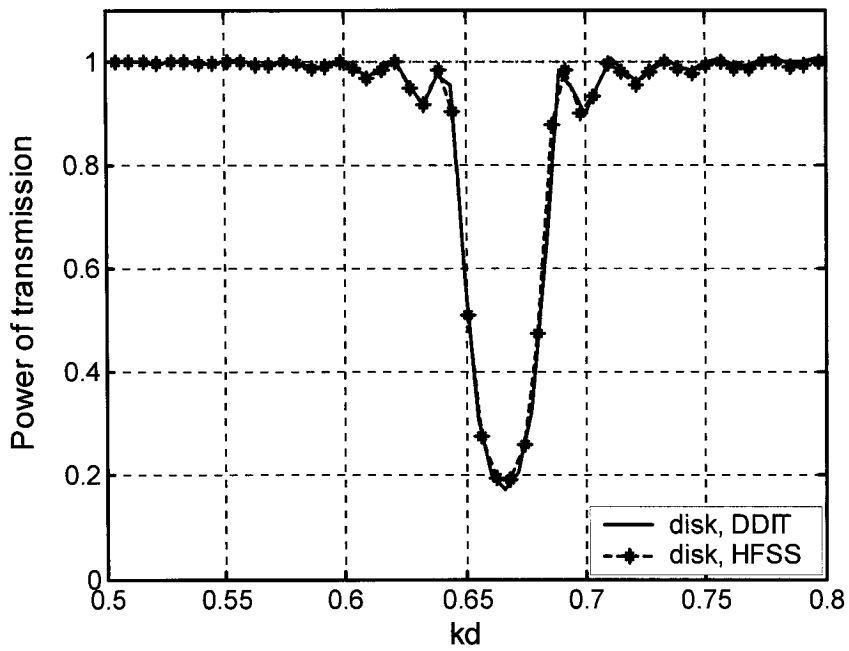

(a) transmission

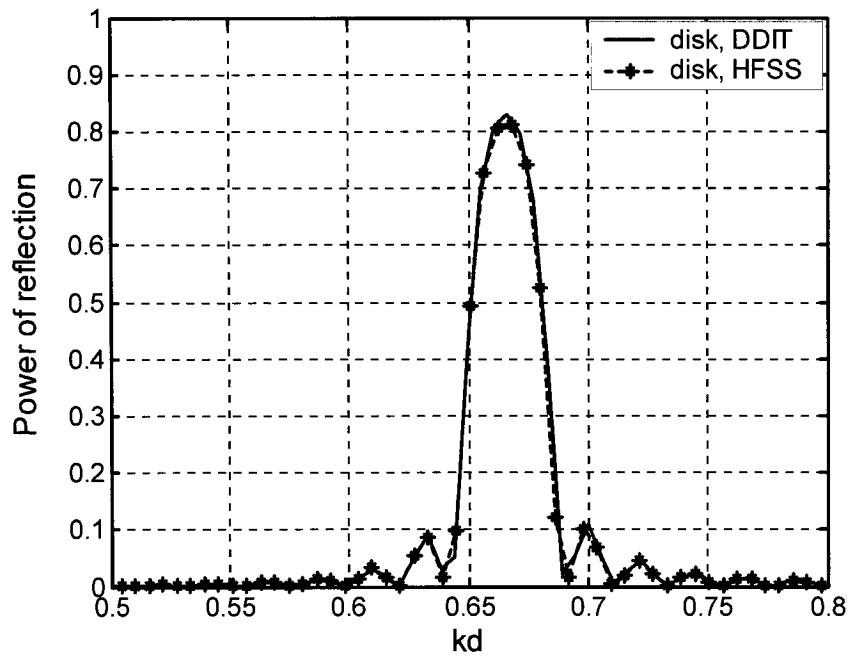

(b) reflection

Fig.9.2 Comparison of the results from HFSS and this theory for the coefficient squares of (a) transmission and (b) reflection.

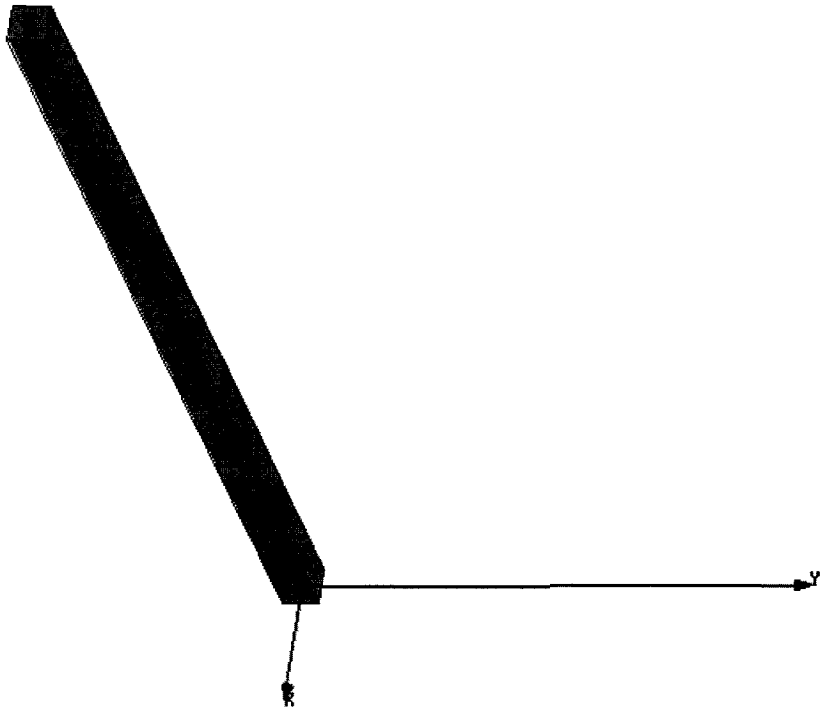

Fig.9.3 Unit cell of an EBG structure with square patches.

The unit cell of the EBG structure with square patches is given in Fig.9.3. Now the number of layers is set to N=20, instead of 30 as for the disk structure. The calculation results from DDIT and HFSS are shown in Fig.9.4, with the disk EBG results (Fig.9.2) re-plotted in the same figure for comparison. The agreement between the results from these two methods is fairly good, there is a notable difference in band gap region. Also at high frequencies, the transmission coefficient from DDIT is slightly beyond one. It should be mentioned that the polarizability formula (5-10) for square patches used in DDIT is valid only for static or very low frequency, in contrast to equation (3-17) for disk patches, which is valid up to the third order of kd. It is seen from the figure that the 20-layer square patch EBG provides deeper band gap than the 30-layer disk patch EBG. The efficiency of square patch in EBG structures is evident, at least from the simulated results. The computing times for the examples by using DDIT are less than 1/100 of those by using HFSS.

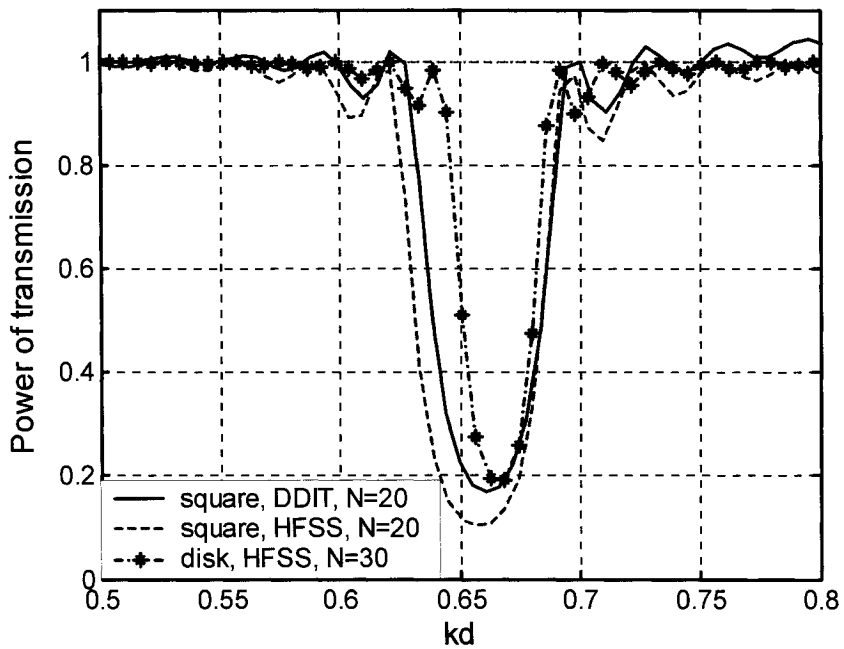

(a) transmission

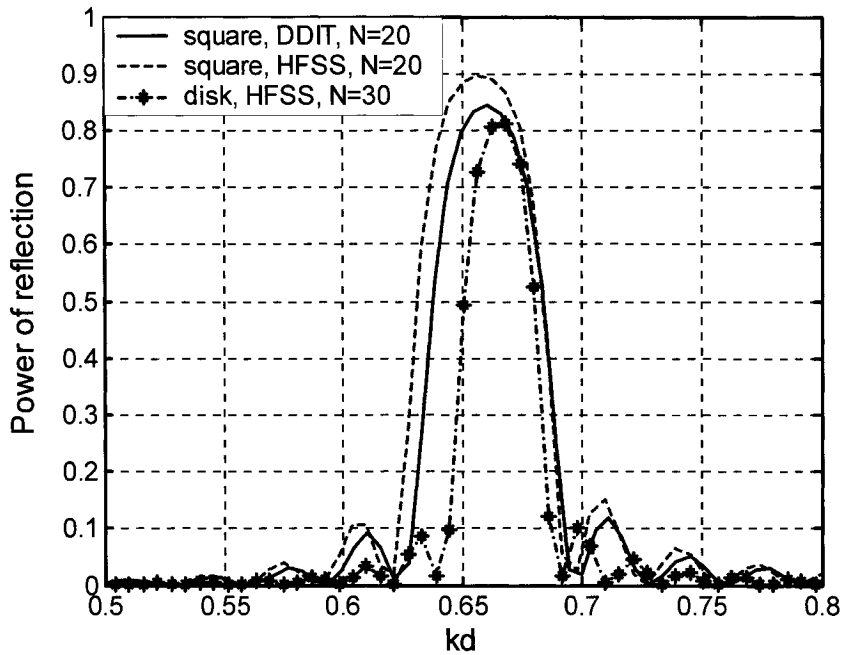

(b) reflection

Fig.9.4 (a) Transmission and (b) reflection of an EBG structure using square patches, result comparison between this theory and HFSS.

9.2 Quantification of small-obstacle assumption

For the same EBG structure using disk patches in the above section, as the frequency increases to certain value, the DDIT starts losing the accuracy. Figure 9.5a shows the extended results of Fig.9.2a by increasing the frequency to kd = 0.94. The predicted transmission coefficient from DDIT gradually exceeds one, the incident wave amplitude, from about kd = 0.85. This indicates that the first basic assumption introduced in the beginning of Chapter 3 (page 13) is violated. The violation becomes worse when the disk spacing (lattice constants) decreases, as shown in Fig.9.5b, where the transmission coefficient exceeds one from about kd = 0.8 for the ratio d/a = 0.7. Ratio d/a is related to the 3rd basic assumption introduced in the beginning of Chapter 3 and should be kept small to satisfy the assumption.

Consider a third EBG example with a different set of lattice parameters: a=b=0.7mm, c=2.4mm, d=0.56mm, N=10. Both the simulation results by using DDIT and HFSS are given in Fig.9.6. As seen, the DDIT result starts deviating at around kd = 0.84. All the examples of EBG structures so far considered are free-standing multi-layer disk lattices. The final example to be presented is an EBG with disk patches printed on dielectric substrates. The lattice parameters are a=b=0.6mm, c=1.714mm, d=0.48mm, N=2, substrate ε_r = 2.2. The transmission coefficients at normal plane wave incidence from free space are shown in Fig.9.7, where the air-dielectric interfaces are considered by both methods. The good agreement between the two simulations is observed up till kd = 0.7 (k is the wave number of the free space), or $k_s d$ = 1.0, if using the wave number k_s in the dielectric. More examples with different parameters are calculated and they show the similar results, thus will not be repeated here.

In conclusion, the full-wave numerical analysis reveals that the small-obstacle assumption becomes invalid when kd increases up to some value between 0.8 and 1.0 (k is the wave number of the host medium). Therefore, the threshold for the assumption to hold or for the DDIT method to be applicable is kd = 0.8, or d/λ = 0.127.

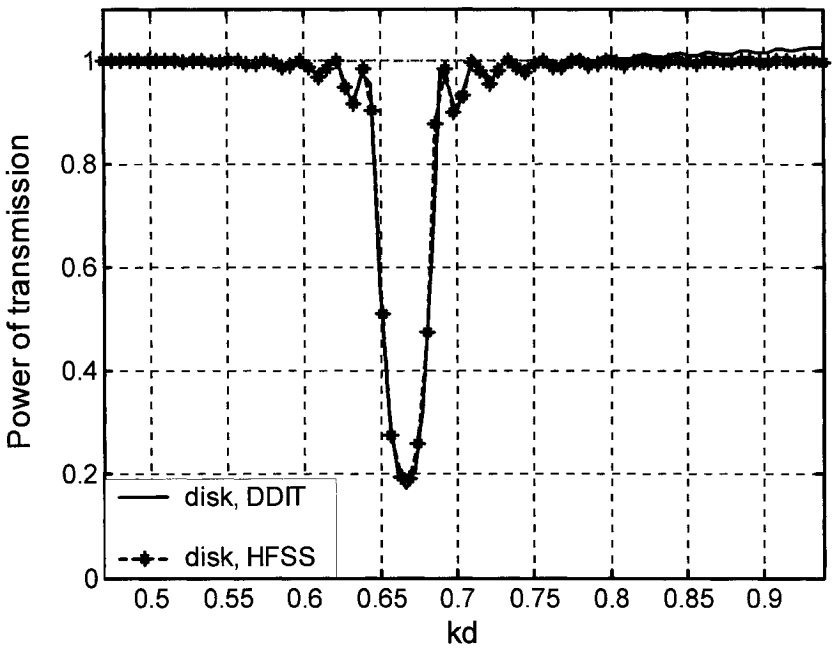

(a) $d/a = 0.467$

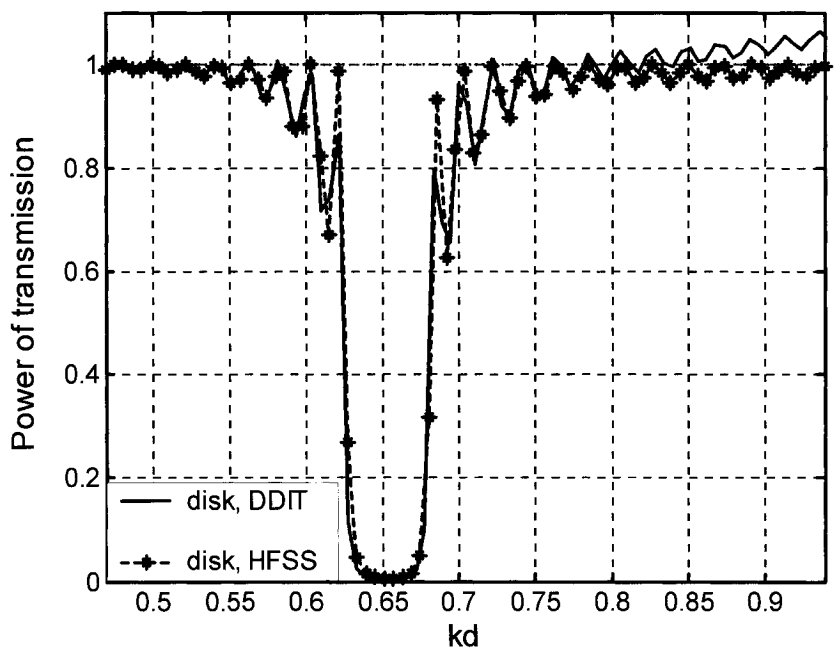

(b) $d/a = 0.7$

Fig.9.5 Transmission coefficient of the EBG used in Fig.9.2, showing the DDIT becomes inaccurate at high frequencies, (a) $d/a = 0.467$ and (b) $d/a = 0.7$.

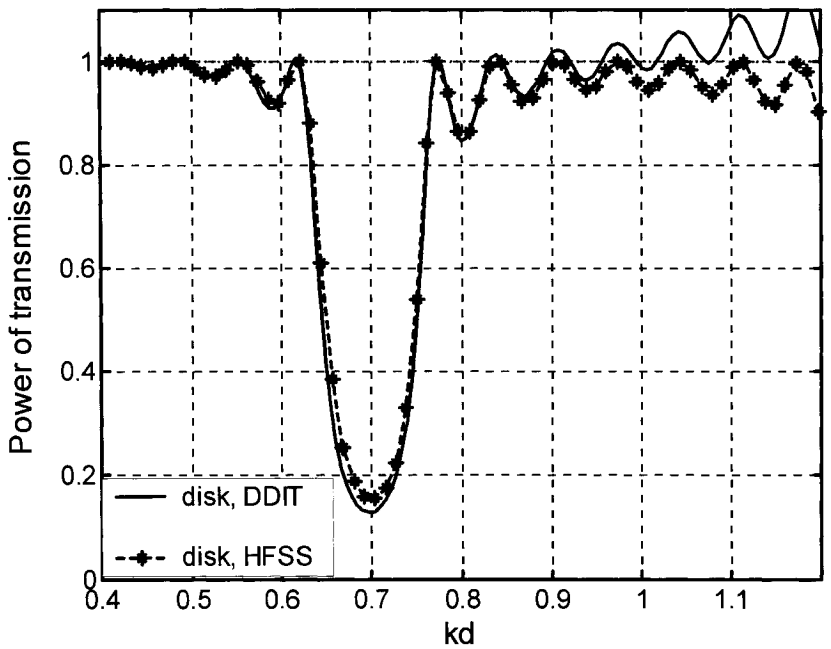

Fig.9.6 Transmission coefficient of the third EBG using disk patches.

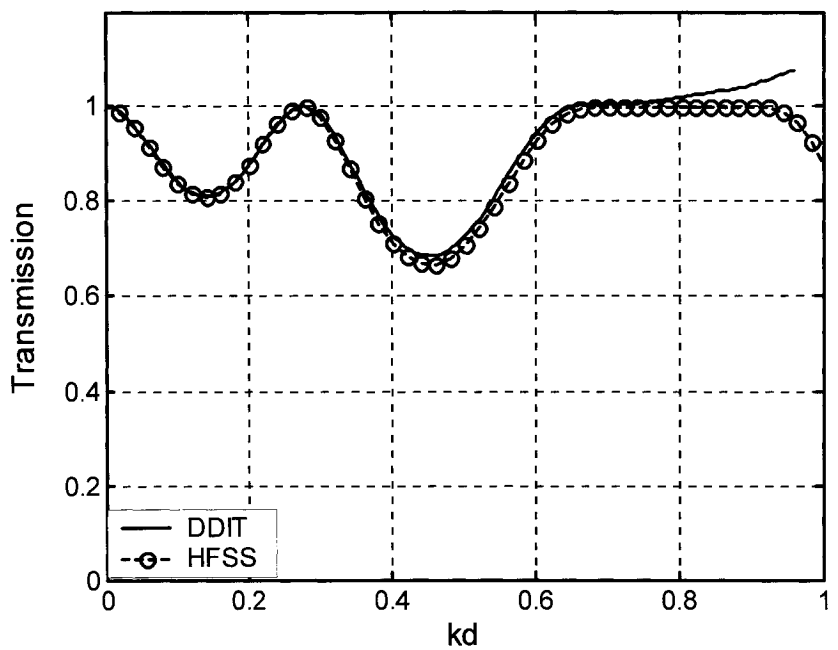

Fig.9.7 Transmission coefficient of the 4th EBG using disk patches on dielectric substrates.

Chapter 10

Concluding remarks and future work

It has been demonstrated through this research that microwave field patterns can be recorded and reproduced by using the proposed artificial microwave volume hologram technique. The AMVH structure consists of cascaded planar lattices of metallic patches with varying size and can be easily fabricated using printed circuit board (PCB) technology. Although this is an off-line recording method for known field intensity patterns, it does open a window to a new, rarely explored area of microwave holographic devices and provides many application opportunities. With this approach, many interesting techniques developed in optical holography can be migrated into microwave and antenna regime.

The central issue in artificial microwave volume holograms is the reconstruction of the required wave beam fields. In their optical counterparts, which are analogue holograms, the reconstruction of required wave fields is automatically realized through the naturally patterned emulsions. In AMVHs, however, this process has to be done manually, as holographic patterns can't be obtained naturally or automatically. The discrete-patch implementation of a holographic pattern results in a large group of varying-size patches distributed in three dimensions, which is difficult to analyze. Furthermore, like most discretization processes, quantization noise will be created as well as resolution loss. Modeling of such complex 3D systems that contain thousands or tens of thousands of discrete elements still remains a challenge, even for current powerful numerical packages.

The research work presented in this dissertation attempted to address this challenge by developing an analytical method to predict the behaviors of AMVHs for a given read out beam. It covers both the theoretical modeling of the interaction between the structure and waves and the fundamental understanding of the artificial microwave volume holograms. It also demonstrated the design guideline, measurement procedure, and application potentials of AMVHs.

10.1 Summary of the thesis work

An analysis technique, i.e., the self-consistent dynamic-dipole-interaction theory (DDIT), has been developed and applied in AMVHs' simulation and design. The method takes into account the interaction between structures and waves and predicts output results. The method has been verified by the rigorous coupled-wave theory, and its validity has been examined and confirmed by a full-wave FEM simulation. It can deal with single and multiplex AMVHs, and can treat both the TE and TM cases. It has also been extended to include the air-dielectric interface effects and therefore can be applied to AMVHs made in finite-thickness dielectric slabs. At the low frequency limit, the DDIT degenerates into the static-dipole-interaction theory (SDIT), the latter can be used to calculate effective permittivity modulations of AMVHs. Furthermore, it is possible to apply this theory to other structures, such as frequency selective surfaces (FSSs), electromagnetic band-gap structures (EBGs), and reflectarrays, as long as it consists of conducting patch elements and their sizes satisfy the small-obstacle assumption.

Multiplex AMVHs have been presented by analogy to optical multiplex holograms. Their flexibility and application potentials are illustrated through a number of examples such as multi-beam antennas, shared apertures, and beam splitting and combining. Various configurations of AMVHs are explored along with a parametric study for increased understanding. New phenomena encountered during beam reproduction are investigated, such as the effects of high order modes and the layer thickness.

Experimental validation of the self-consistent dynamic-dipole-interaction theory has been carried out on several fabricated AMVHs. Comparison between the predicted and measured results has been made and good agreement has been observed in general, though some discrepancies do exist due to various practical factors. A procedure for measuring each individual mode instead of the total field is also presented.

Finally, a new patch geometry, a square patch, has been proposed and analyzed for the application in AMVHs. It is found that a square patch can provide 50% higher electric polarizability compared to a disk patch of same size. This finding leads to a reduction in the number of layers required for making AMVHs or EBG structures without compromising

their performance. The new patch makes AMVHs or similar structures more compact and cost efficient.

10.2 Suggestions for future research

Artificial microwave volume hologram is a relative new topic. There are many unsolved problems and unexplored aspects. One of the interesting theoretical aspects is the multi-pole interaction among the patches. This is a natural extension of the dipole interaction theory and would be useful for high frequency analyses where the multi-pole interaction could not be neglected. Another benefit of developing the multi-pole interaction theory is that it can help design more compact AMVH devices, as patches can be located closer to each other.

It is noted that AMVHs can also be used for wave front modification like optical holograms. A typical case is converting a plane wave beam into a spherical wave converged at certain point outside the hologram, or vice versa, by properly designing an AMVH. This will be an interesting and important application as the AMVH works like a microwave lens. Because the interference pattern formed by a uniform plane wave and a spherical wave is no longer periodical in this case, the resulting holographic grating function and therefore the corresponding patch size modulation will be aperiodic. The DDIT can still be applied to this case, but instead of considering one period and taking advantage of the periodical condition, it has to include all dipole contributions from all patches. The computing time is expected to be much longer, though in principle it can be done. Furthermore, by applying the multiplexing hologram procedure, one may achieve a multiplex AMVH with multiple focus points corresponding to multiple beams.

To eliminate the effect due to the finite beam width and the non-uniform beam profile as described in Chapter 7, a plane wave measurement setup is necessary for studying AMVHs. Here, we have proposed an experiment procedure that uses infinite uniform plane wave incidence, as shown in Fig.10.1. A point source (say, a dipole antenna) is placed far away from an absorbing surface to obtain a uniform plane wave incidence at the surface. A rectangular aperture is cut on the surface with its dimensions being much larger than the wavelength used so that the field through the aperture is dominant by the incident plane

wave. The hologram to be tested is placed right behind the aperture with its area larger than the aperture area so that it seals the aperture. The incident plane wave, that passes through the aperture and impinges on the hologram, will be scattered by the effective dielectric grating(s) inside the hologram. Then the transmitted and the diffracted waves are detected by a probe antenna, which can be scanned mechanically over the back surface of the hologram. Finally, the recorded field distribution on the back surface for each given angle of incidence is Fourier transformed to abstract the transmitted and diffracted beams.

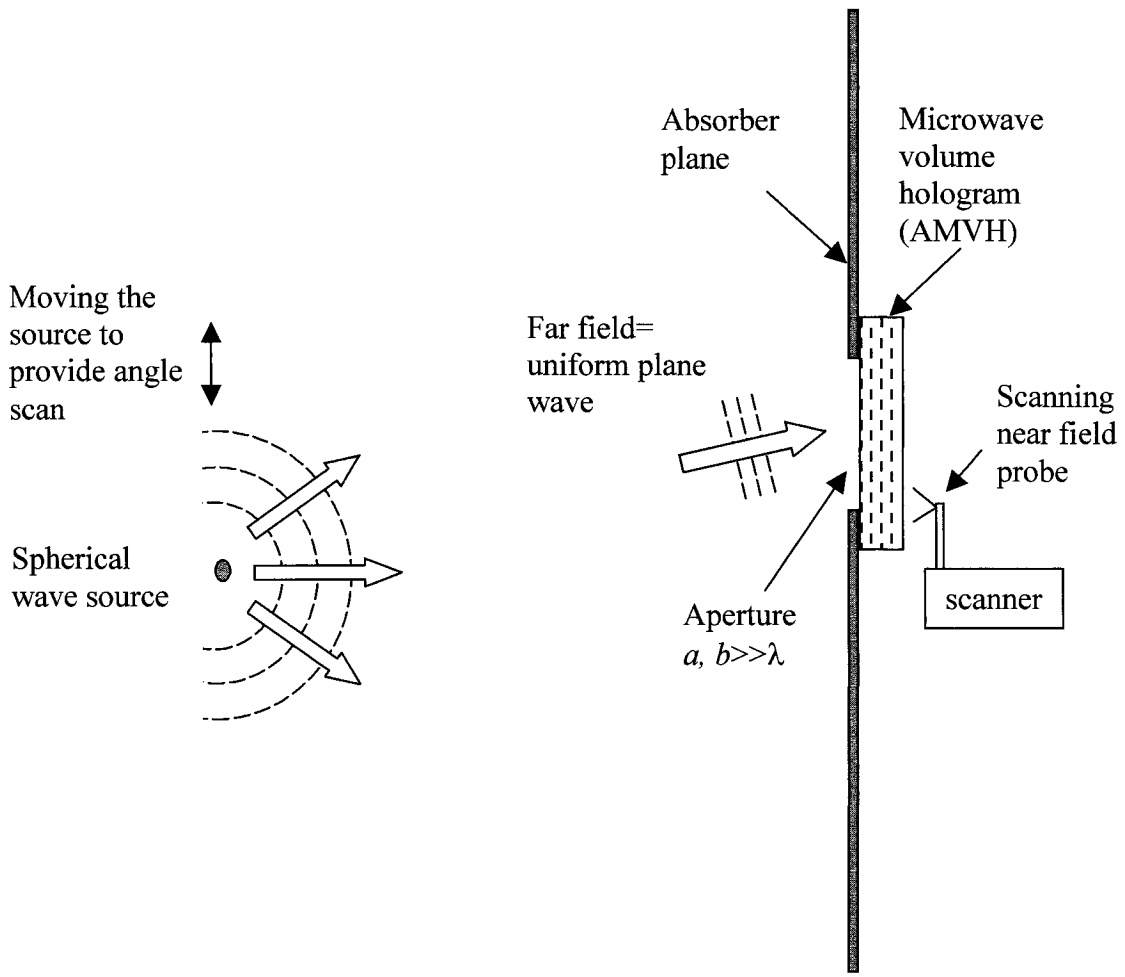

Fig.10.1 Scheme of uniform plane wave measurement setup.

Usually, the recorded data is a convolution of the original field and the aperture function of the receiving antenna. Therefore, a de-convolution process is also needed to recover the original field before the spatial FFT is applied. The incident angle scan can be achieved by transversely moving the source antenna with respect to the aperture. Some absorbing material can be attached around the edges of the aperture to reduce the edge diffraction. The system should be setup in a far-field anechoic chamber to avoid all possible reflections.

Appendix A

Limit and asymptotic analyses

In this appendix, the limitation and asymptotic operations used in Chapter 3 to obtain equations (3-13) to (3-15) are described in details. Because of the massive formulism, only the portion related to the electric dipoles under the TE incidence is demonstrated as an example. For those related to the magnetic dipoles under TE incidence and the electric dipoles under the TM incidence, the limitation and asymptotic analyses can be carried out in a similar way.

Consider equation (3-8a), as the field point $\boldsymbol{r}$ approaching a disk center at $x=i'a$, $z=n'c$, $y=0$. The contribution from the electric dipole with the indices (n', i') should be subtracted from (3-8a). Also, one needs to exam the convergence or divergence of the series over m in the first term in (3-8a) at a disk center.

Let's first consider the subtracted part. Equation (3-2) can be rewritten, for the y component of the electric field, as

$$E^{y,e} = \frac{1}{j\omega\mu\varepsilon}[k^2 + \frac{\partial^2}{\partial y^2}]A_y \qquad \text{(A-1)}$$

From (3-5a) and (A-1), after subtracting the contribution of the dipole (n', i'), equation (3-8a) can be rewritten as

$$\begin{aligned} E^{y,e}_{n'i'} &= E^{y,e}(x \to i'a, y = 0, z \to n'c) = \\ &= \frac{1}{2\pi\varepsilon b}\{\frac{\pi k^2}{Ia}\sum_{n=0}^{N-1}\sum_{i=0}^{I-1} p_{ni} e^{jk_x ia} \sum_{m=-\infty}^{\infty} \frac{1}{v_m} e^{j2\pi mi/I} e^{-v_m|z-nc|-ju_m x} - k^2 p_{n'i'} \lim_{\rho\to 0} K_0(jk\rho) \\ &\quad - 2\gamma_1^2 \cos(\frac{2\pi y}{b})[\sum_{n=0}^{N-1}\sum_{i=0}^{I-1} p_{ni} \sum_{m=-\infty}^{\infty} e^{-jk_x mIa} K_0(\gamma_1 r^n_{mi}) - p_{n'i'} K_0(\gamma_1 r^{n'}_{0i'})]\} + E^y_{imag}, \end{aligned} \qquad \text{(A-2)}$$

where E^{y}_{imag} is the total contribution from the electric dipoles at $x=i'a$, $z=n'c$, $y=\pm mb$ (keep in mind that when removing one dipole in Fig.3.3a, we actually remove an 1D dipole array due to the periodic condition in the y-direction). These dipoles are the images of the dipole at $x=i'a$, $z=n'c$, $y=0$, and their total contribution can be expressed as (from the well known single dipole field in a free space)

$$E^{y}_{imag} = \lim_{r\to 0}(k^2 + \frac{\partial^2}{\partial y^2})[\frac{p_{n'i'}}{4\pi\varepsilon}\sum_{\substack{s=-\infty \\ s\neq 0}}^{\infty}\frac{\exp(jk\sqrt{x^2+z^2+(mb-y)^2})}{\sqrt{x^2+z^2+(mb-y)^2}}], \quad r=\sqrt{x^2+z^2+y^2} \quad \text{(A-3)}$$

After carrying out the operation included in the round brackets and then completing the limitation operation, we obtain

$$E^{y}_{imag} = \frac{p_{n'i'}}{4\pi\varepsilon b^3}\sum_{\substack{s=-\infty \\ s\neq 0}}^{\infty}\exp(-jkb|s|)[\frac{2jkb}{|s|^2}+\frac{2}{|s|^3}] \quad \text{(A-4)}$$

The two series in (A-4) are readily summed by standard methods [20] and (A-4) can be expressed as

$$E^{y}_{imag} = \frac{p_{n'i'}}{\pi\varepsilon b^3}[1.202+\frac{(\overline{kb})^2}{2}(\frac{1}{2}-\ln\overline{kb})+\frac{(\overline{kb})^4}{96}+j\frac{(\overline{kb})^2}{4}(\frac{2}{3}\overline{kb}-\pi)], \quad \text{(A-5)}$$

From the asymptotic properties of Bessel function [62], we have

$$\lim_{r\to 0} K(jkr) = -[\gamma + \ln(jkr/2)], \quad \text{with Eular's constant } \gamma = 0.577 \quad \text{(A-6)}$$

Next, consider the infinite summation over m in the first term of (A-2). For large m,

$$\frac{1}{v_m} = \frac{1}{\sqrt{u_m^2 - k^2}} = \frac{1}{\sqrt{(2\pi m/Ia + k_x)^2 - k^2}} = \frac{Ia}{2\pi|m|} + 0[\frac{1}{m^2}], \quad \text{(A-7)}$$

The series over m in the first term in (3-8a) can be rewritten as

$$e^{jk_x i'a}\sum_{m=-\infty}^{\infty}\frac{1}{v_m}e^{j2\pi mi'/I}e^{-v_m|z-n'c|-ju_m x}=e^{-jk_x(x-i'a)}\{\frac{e^{-jk_z|z-n'c|}}{jk_z}+\sum_{\substack{m=-\infty\\m\neq 0}}^{\infty}\frac{1}{v_m}e^{-v_m|z-n'c|-j2\pi m(x-i'a)/Ia}\}=$$

$$=e^{-jk_x(x-i'a)}\{\frac{e^{-jk_z|z-n'c|}}{jk_z}+\sum_{\substack{m=-\infty\\m\neq 0}}^{\infty}[\frac{1}{v_m}e^{-v_m|z-n'c|-j2\pi m(x-i'a)/Ia}-\frac{Ia}{2\pi|m|}e^{-2\pi[|m||z-n'c|-jm(x-i'a)]/Ia}]$$
$$+\sum_{\substack{m=-\infty\\m\neq 0}}^{\infty}\frac{Ia}{2\pi|m|}e^{-2\pi[|m||z-n'c|-jm(x-i'a)]/Ia}, \tag{A-8}$$

where the last series is readily summed in a usual way to give

$$\sum_{\substack{m=-\infty\\m\neq 0}}^{\infty}\frac{Ia}{2\pi|m|}e^{-2\pi[|m||z-n'c|-jm(x-i'a)]/Ia}=$$
$$=\frac{Ia}{2\pi}\{-\ln[2\sinh\pi\frac{|z-n'c|+j(x-i'a)}{Ia}]+\pi\frac{|z-n'c|+j(x-i'a)}{Ia}$$
$$-\ln[2\sinh\pi\frac{|z-n'c|-j(x-i'a)}{Ia}]+\pi\frac{|z-n'c|-j(x-i'a)}{Ia}\} \tag{A-9}$$
$$=|z-nc|-\frac{Ia}{2\pi}\{\ln[4\sinh\pi\frac{|z-n'c|+j(x-i'a)}{Ia}\sinh\pi\frac{|z-n'c|-j(x-i'a)}{Ia}]\}$$
$$\to\frac{Ia}{\pi}[-\ln\frac{jkr}{2}+\ln(jk\frac{Ia}{4\pi})],\ \text{as}\ x\to i'a, y\to n'c, (\text{or}\ r\to 0)$$

Comparing (A-9) with (A-6), one can see that the logarithmic singularity due to the Bessel function in (A-2) is cancelled by the logarithmic singularity arising from the divergent part of the series in the first term in (A-2). The first series in (A-8) reduces to, after the limiting operation is completed,

$$\sum_{\substack{m=-\infty\\m\neq 0}}^{\infty}[\frac{1}{v_m}-\frac{Ia}{2\pi|m|}],$$

which is obviously convergent. Finally, from (A-5), (A-6), and (A-8), the y component of the electric field (A-2) at the lattice node of (n', i') can be obtained as

$$
\begin{aligned}
E^{y,e}_{n'i'} / E_0 &= E^{y,e}(x \to i'a, y = 0, z \to n'c) / E_0 = \\
&= \frac{(\bar{k}\bar{b})^2}{2I} \sum_{n=0}^{N-1} \sum_{i=0}^{I-1} \bar{p}_{ni} e^{j\bar{k}_x (i-i')} \left[\frac{e^{-j\bar{k}_z |n-n'|\bar{c}}}{j\bar{k}_z} + \sum_{\substack{m=-\infty \\ m \neq 0}}^{\infty} \left(\frac{e^{-\bar{\nu}_m |n-n'|\bar{c} - j2\pi m(i'-i)/I}}{\bar{\nu}_m} - \frac{I}{2\pi |m|} \delta_{ii'} \delta_{nn'} \right) \right] \\
&\quad - \frac{(\bar{\gamma}_1 \bar{b})^2}{\pi} \left[\sum_{n=0}^{N-1} \sum_{i=0}^{I-1} \bar{p}_{ni} K_0(\bar{\gamma}_1 \bar{r}_0) \Big|_{\bar{r}_0 \neq 0} + \sum_{n=0}^{N-1} \sum_{i=0}^{I-1} \bar{p}_{ni} \sum_{\substack{m=-\infty \\ m \neq 0}}^{\infty} e^{-j\bar{k}_x mI} K_0(\bar{\gamma}_1 \bar{r}_m) \right] \\
&\quad + \frac{\bar{p}_{n'i'}}{\pi} \left[1.202 + \frac{(\bar{k}\bar{b})^2}{2} \left(\gamma + 0.5 + \ln \frac{I}{4\pi\bar{b}} \right) + \frac{(\bar{k}\bar{b})^4}{96} + j \frac{(\bar{k}\bar{b})^3}{6} \right],
\end{aligned}
\tag{A-10}
$$

where use has been made of (3-12) for the dimensionless quantities.

In a similar manner, the other components of electric and magnetic fields in (3-8b), (3-9a), and (3-9b) can be obtained at the lattice node of (n', i') as well.

Appendix B

Solution of second-order coupled-wave equations

In this appendix, the solution of the second-order two-mode coupled-wave equations (4-10) in Chapter 4 is derived. The solutions within the effective continuous hologram slab and outside the slab (homogeneous dielectric half-spaces) are obtained simultaneously by applying the field-continuity condition at the interfaces. Here, we only consider the TE propagations with the electric field along the *y*-direction (out of the plan in Fig.4.5). Results for the TM propagations with the magnetic field along the *y*-direction can be derived in a similar way.

Consider equation (4-10) in Chapter 4, which can be rewritten in a matrix format as

$$\begin{bmatrix} 1 & 0 \\ 0 & 1 \end{bmatrix}\begin{bmatrix} f_0'' \\ f_{-1}'' \end{bmatrix}+\begin{bmatrix} k_2^2-k_{0x}^2 & k_2^2\varepsilon_d \\ k_2^2\varepsilon_d & k_2^2-k_{-1x}^2 \end{bmatrix}\begin{bmatrix} f_0 \\ f_{-1} \end{bmatrix}=\begin{bmatrix} 0 \\ 0 \end{bmatrix},\quad \text{with } \varepsilon_d=\frac{\Delta\varepsilon}{2},\ ()'=\frac{d()}{dz} \qquad \text{(B-1)}$$

where k_2 is the wave-number in the hologram slab if the dielectric modulation ($\Delta\varepsilon$) doesn't exist, k_{0x} and k_{-1x}, the mode propagation number in the x-direction as defined in (4-8), and the f_0 and f_{-1} are the 0– and -1–order coefficients of the mode expansion (4-8), and are functions of only z. Introducing a pair of new unknowns by

$$\begin{bmatrix} g_1 \\ g_2 \end{bmatrix}=[C]\begin{bmatrix} f_0 \\ f_{-1} \end{bmatrix}\equiv\begin{bmatrix} 1 & -\alpha_1 \\ 1 & -\alpha_2 \end{bmatrix}\begin{bmatrix} f_0 \\ f_{-1} \end{bmatrix},$$

$$\text{then, } \begin{bmatrix} f_0 \\ f_{-1} \end{bmatrix}=[C]^{-1}\begin{bmatrix} g_1 \\ g_2 \end{bmatrix}\equiv\frac{1}{\alpha_2-\alpha_1}\begin{bmatrix} \alpha_2 & -\alpha_1 \\ 1 & -1 \end{bmatrix}\begin{bmatrix} g_1 \\ g_2 \end{bmatrix}, \qquad \text{(B-2a,b)}$$

where α_i are constants to be determined. Substituting f_0 and f_{-1} in (B-1) with (B-2b) and multiplying both sides of the equation by $[C]$ gives,

$$\begin{bmatrix}1 & 0\\ 0 & 1\end{bmatrix}\begin{bmatrix}g_1''\\ g_2''\end{bmatrix}+\frac{1}{\alpha_2-\alpha_1}\begin{bmatrix}1 & -\alpha_1\\ 1 & -\alpha_2\end{bmatrix}\begin{bmatrix}k_2^2-k_{0x}^2 & k_2^2\varepsilon_d\\ k_2^2\varepsilon_d & k_2^2-k_{-1x}^2\end{bmatrix}\begin{bmatrix}\alpha_2 & -\alpha_1\\ 1 & -1\end{bmatrix}\begin{bmatrix}g_1\\ g_2\end{bmatrix}=\begin{bmatrix}0\\ 0\end{bmatrix}, \quad \text{(B-3)}$$

The matrix product in the second term in (B-3) results in a simple diagonal matrix, if we choose the constants so that

$$(\alpha_i^2-1)k_2^2\varepsilon_d+\alpha_i(k_{0x}^2-k_{-1x}^2)=0, \qquad i=1,2$$
$$\text{or,}\quad \alpha_{1,2}=\frac{(k_{-1x}^2-k_{0x}^2)\pm\sqrt{(k_{-1x}^2-k_{0x}^2)^2+(2\varepsilon_d k_2^2)^2}}{2\varepsilon_d k_2^2} \quad \text{(B-4)}$$

Then, the equation (B-3) becomes

$$\begin{bmatrix}1 & 0\\ 0 & 1\end{bmatrix}\begin{bmatrix}g_1''\\ g_2''\end{bmatrix}+\begin{bmatrix}k_2^2-k_{0x}^2-\alpha_1\varepsilon_d k_2^2 & 0\\ 0 & k_2^2-k_{0x}^2-\alpha_2\varepsilon_d k_2^2\end{bmatrix}\begin{bmatrix}g_1\\ g_2\end{bmatrix}=\begin{bmatrix}0\\ 0\end{bmatrix}, \quad \text{(B-5)}$$

which is de-coupled about the new unknowns. The solution of equation (B-5) is readily found to be

$$\begin{bmatrix}g_1(z)\\ g_2(z)\end{bmatrix}=\begin{bmatrix}A_1e^{-jv_1z}+B_1e^{jv_1z}\\ A_2e^{-jv_2z}+B_2e^{jv_2z}\end{bmatrix}, \quad \text{with}\quad v_i=\sqrt{(1-\alpha_i\varepsilon_d)k_2^2-k_{0x}^2} \quad \text{(B-6)}$$

From (B-2b), we have

$$\begin{bmatrix}f_0\\ f_0'\\ f_{-1}\\ f_{-1}'\end{bmatrix}=\frac{1}{\alpha_2-\alpha_1}\begin{bmatrix}\alpha_2e^{-jv_1z} & \alpha_2e^{jv_1z} & -\alpha_1e^{-jv_2z} & -\alpha_1e^{jv_2z}\\ -jv_1\alpha_2e^{-jv_1z} & jv_1\alpha_2e^{jv_1z} & jv_2\alpha_1e^{-jv_2z} & -jv_2\alpha_1e^{jv_2z}\\ e^{-jv_1z} & e^{jv_1z} & -e^{-jv_2z} & -e^{jv_2z}\\ -jv_1e^{-jv_1z} & jv_1e^{jv_1z} & jv_2e^{-jv_2z} & -jv_2e^{jv_2z}\end{bmatrix}\begin{bmatrix}A_1\\ B_1\\ A_2\\ B_2\end{bmatrix} \quad \text{(B-7)}$$

For the TE case, the continuity condition for the tangential fields requires E_y and H_x (or $\partial E_y/\partial z$, as $\omega\mu$ is same for all regions) to be continuous across an interface. Under homogeneous plane wave incidence with unit amplitude, the field in the left half-space in Fig.4.5 ($z < 0$) can be expressed as

$$E_y^L = e^{-j(k_{0x}x+k_{0z}z)} + R_0 e^{-j(k_{0x}x-k_{0z}z)} + R_{-1} e^{-j(k_{0x}x-k_{0z}z)}, \quad H_x^L = \frac{1}{j\omega\mu}\frac{\partial E_y^L}{\partial z},$$
$$k_{0z} = k_1 \cos\vartheta_{in}, \quad k_{-1z} = \sqrt{k_1^2 - k_{-1x}^2} \tag{B-8}$$

while, the field in the right half-space in Fig.4.5 ($z > t$) can be written as

$$E_y^R = T_0 e^{-j[k_{0x}x+k_{0z}(z-t)]} + T_{-1} e^{-j[k_{0x}x+k_{0z}(z-t)]}, \quad H_x^R = \frac{1}{j\omega\mu}\frac{\partial E_y^R}{\partial z} \tag{B-9}$$

The phase match condition at interface requires each mode satisfying the continuity condition independently.

$$\begin{bmatrix} E_{0y} \\ \omega\mu H_{0x} \\ E_{-1y} \\ \omega\mu H_{-1x} \end{bmatrix}_{z=0} = \begin{bmatrix} E_{0y}^L \\ \omega\mu H_{0x}^L \\ E_{-1y}^L \\ \omega\mu H_{-1x}^L \end{bmatrix}_{z=0}, \quad \begin{bmatrix} E_{0y} \\ \omega\mu H_{0x} \\ E_{-1y} \\ \omega\mu H_{-1x} \end{bmatrix}_{z=t} = \begin{bmatrix} E_{0y}^R \\ \omega\mu H_{0x}^R \\ E_{-1y}^R \\ \omega\mu H_{-1x}^R \end{bmatrix}_{z=t}. \tag{B-10}$$

From (B-10) and (B-7), we obtain

$$\begin{bmatrix} \alpha_2 & \alpha_2 & -\alpha_1 & -\alpha_1 \\ -v_1\alpha_2 & v_1\alpha_2 & v_2\alpha_1 & -v_2\alpha_1 \\ 1 & 1 & -1 & -1 \\ -v_1 & v_1 & v_2 & -v_2 \end{bmatrix} \begin{bmatrix} \alpha_2 e^{-jv_1 t} & \alpha_2 e^{jv_1 t} & -\alpha_1 e^{-jv_2 t} & -\alpha_1 e^{jv_2 t} \\ -v_1\alpha_2 e^{-jv_1 t} & v_1\alpha_2 e^{jv_1 t} & v_2\alpha_1 e^{-jv_2 t} & -v_2\alpha_1 e^{jv_2 t} \\ e^{-jv_1 t} & e^{jv_1 t} & -e^{-jv_2 t} & -e^{jv_2 t} \\ -v_1 e^{-jv_1 t} & v_1 e^{jv_1 t} & v_2 e^{-jv_2 t} & -v_2 e^{jv_2 t} \end{bmatrix}^{-1} \begin{bmatrix} T_0 \\ -T_0 k_{0z} \\ T_{-1} \\ -T_{-1} k_{-1z} \end{bmatrix}$$
$$= \begin{bmatrix} R_0 + 1 \\ (R_0 - 1)k_{0z} \\ R_{-1} \\ R_{-1} k_{-1z} \end{bmatrix}, \tag{B-11}$$

Equation (B-11) can be re-arranged to become a standard linear equation system, and it can be readily solved by a standard method for the unknowns R_0, R_{-1}, T_0, and T_{-1}, i.e., the reflection and transmission coefficients for the two propagation modes.

Appendix C

Closed form element integration in the Method of Moments formulation

In this appendix, the 2-D integration over a triangular area in equation (5-8) in Chapter 5 is completed explicitly. Consider an arbitrary triangle in the *x*-*y* plane with the three corners labeled as ①, ②, and ③, counterclockwise as shown in Fig.C-1a. We define the following coordinates transform, which maps the triangle in the physical plane to the standard triangle in the ξ-η plane (Fig.C-1b). The standard triangle has its right-angle node located at the origin, and each edge connected to the node has unit length.

$$\begin{aligned} x &= (x_1 - x_3)\xi + (x_2 - x_3)\eta + x_3, \\ y &= (y_1 - y_3)\xi + (y_2 - y_3)\eta + y_3 \end{aligned} \tag{C-1}$$

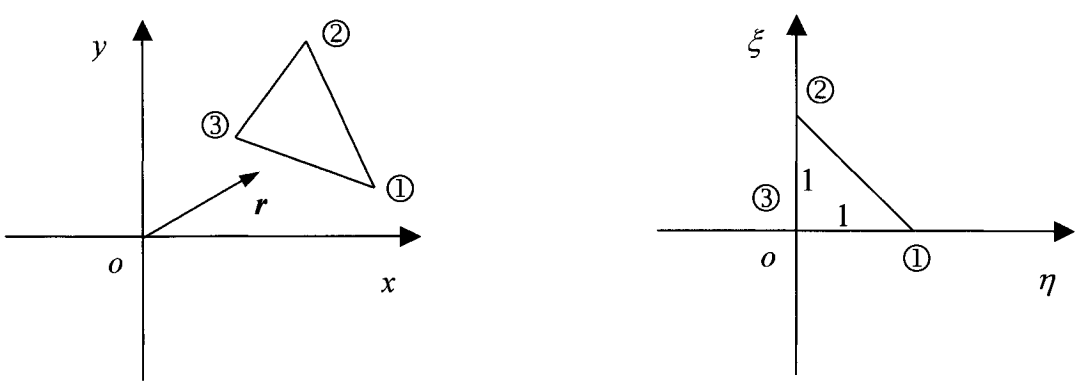

(a) (b)

Fig.C-1 Coordinate transformation, (a) physical plane, and (b) transformed plane.

Under this transformation, the integral in eq.(5-8) can be rewritten as

$$\iint_{\Omega_e} \frac{dx'\,dy'}{|\mathbf{r}'-\mathbf{r}|} = \iint_{\Omega_e} \frac{\partial(x,y)}{\partial(\xi,\eta)} \frac{d\xi d\eta}{R} = 2\Delta_e \iint_{\Omega'_e} \frac{d\xi d\eta}{R} \tag{C-2}$$

where, Δ_e is the area of the triangle in the physical plane, determined by

$$2\Delta_e = \frac{\partial(x,y)}{\partial(\xi,\eta)} = \begin{vmatrix} x_1 - x_3 & x_2 - x_3 \\ y_1 - y_3 & y_2 - y_3 \end{vmatrix}, \tag{C-3}$$

and R can be expressed as

$$\begin{aligned} R &= |\mathbf{r}'-\mathbf{r}| = |(\mathbf{r}_1 - \mathbf{r}_3)\xi + (\mathbf{r}_2 - \mathbf{r}_3)\eta + (\mathbf{r}_3 - \mathbf{r})| \\ &= \sqrt{[(x_1 - x_3)\xi + (x_2 - x_3)\eta + (x_3 - x)]^2 + [(y_1 - y_3)\xi + (y_2 - y_3)\eta + (y_3 - y)]^2} \\ &= \sqrt{A + B\eta + C\eta^2}, \end{aligned} \tag{C-4}$$

where, $A = A(\xi) = |(\mathbf{r}_1 - \mathbf{r}_3)\xi + (\mathbf{r}_3 - \mathbf{r})|^2$,

$B = B(\xi) = 2(\mathbf{r}_2 - \mathbf{r}_3) \bullet [(\mathbf{r}_1 - \mathbf{r}_3)\xi + (\mathbf{r}_3 - \mathbf{r})]$,

$C = |(\mathbf{r}_2 - \mathbf{r}_3)|^2$

From (C-4), the integral in (C-2) can be expressed as

$$\iint_{\Omega'_e} \frac{d\xi d\eta}{R} = \int_0^1 d\xi \int_0^{1-\xi} \frac{d\eta}{\sqrt{A + B\eta + C\eta^2}} = \int_0^1 \frac{1}{\sqrt{C}} [sh^{-1} \frac{2C(1-\xi) + B}{\Gamma} - sh^{-1} \frac{B}{\Gamma}] d\xi \tag{C-5}$$

where use has been made of formula (2.261) in [62] for completing the integration about η, and

$$\Gamma = \Gamma(\xi) \equiv \sqrt{4A(\xi)C - B(\xi)^2} = 2|(\mathbf{r}_2 - \mathbf{r}_3) \times [(\mathbf{r}_1 - \mathbf{r}_3)\xi + (\mathbf{r}_3 - \mathbf{r})]| \tag{C-6}$$

To simplify the integral in (C-5), let,

$$\frac{2C(1-\xi) + B(\xi)}{\Gamma(\xi)} \equiv X, \quad \frac{B(\xi)}{\Gamma(\xi)} \equiv X' \tag{C-7}$$

From (C-4), (C-7) can be expressed as

$$X=\frac{a'-c'\xi}{-b'+d'\xi},\quad X'=\frac{a''-c''\xi}{-b''+d''\xi} \tag{C-8a,b}$$

where

$$\begin{aligned}
&a'=2(\mathbf{r}_2-\mathbf{r}_3)\bullet(\mathbf{r}_2-\mathbf{r}),\quad c'=2(\mathbf{r}_2-\mathbf{r}_3)\bullet(\mathbf{r}_2-\mathbf{r}_1),\\
&a''=2(\mathbf{r}_2-\mathbf{r}_3)\bullet(\mathbf{r}_1-\mathbf{r}_3),\quad c''=2(\mathbf{r}_2-\mathbf{r}_3)\bullet(\mathbf{r}-\mathbf{r}_3),\\
&b'=b''=-2\,|(\mathbf{r}_2-\mathbf{r}_3)\times(\mathbf{r}_3-\mathbf{r})|,\\
&d'=d''=2\,|(\mathbf{r}_2-\mathbf{r}_3)\times(\mathbf{r}_1-\mathbf{r})|-2\,|(\mathbf{r}_2-\mathbf{r}_3)\times(\mathbf{r}_3-\mathbf{r})|,
\end{aligned} \tag{C-9}$$

Then, applying (C-8a and b) to the two integrands in (C-5) respectively, the integration reduces to

$$\begin{aligned}
&-\frac{1}{\sqrt{C}}\{\int_s^h\frac{a'+b'X}{c'+d'X}\frac{dX}{\sqrt{1+X^2}}-\int_{s'}^{h'}\frac{a''+b''X'}{c''+d''X'}\frac{dX'}{\sqrt{1+X'^2}}\}\\
&=-\frac{1}{\sqrt{C}}\{\frac{b'}{d'}\ln(\sqrt{1+X^2}+X)|_s^h-\frac{b''}{d''}\ln(\sqrt{1+X'^2}+X')|_{s'}^{h'}\}\\
&-\frac{1}{\sqrt{C}}\{\frac{b'}{d'}(\frac{a'}{b'}-\frac{c'}{d'})\int_s^h\frac{1}{c'/d'+X}\frac{dX}{\sqrt{1+X^2}}-\frac{b''}{d''}(\frac{a''}{b''}-\frac{c''}{d''})\int_{s'}^{h'}\frac{1}{c''/d''+X'}\frac{dX'}{\sqrt{1+X'^2}}\}
\end{aligned} \tag{C-10}$$

where

$$h=\frac{a'-c'}{-b'+d'},\quad s=-\frac{a'}{b'},\quad h'=\frac{a''-c''}{-b''+d''},\quad s'=-\frac{a''}{b''} \tag{C-11}$$

From (2.266) of [62], the last integrals in (C-10) can be completed in closed forms. After some tedious manipulation, we have

$$\begin{aligned}
&2\Delta_e\iint_{\Omega'_e}\frac{d\xi d\eta}{R}=\\
&\frac{2\Delta_e}{\sqrt{C}}\frac{b'}{d'}\{\ln[\sqrt{(\frac{2C+B(0)}{\Gamma(0)})^2+1}+(\frac{2C+B(0)}{\Gamma(0)})]-\ln[\sqrt{(\frac{B(0)}{\Gamma(0)})^2+1}+\frac{B(0)}{\Gamma(0)}]\}\\
&+\frac{2\Delta_e}{\sqrt{C}}\frac{b'}{d'}\{\frac{a'/b'-w'}{\sqrt{1+w'^2}}\ln[2\frac{1-w'X+\sqrt{(1+w'^2)(1+X^2)}}{X+w'}]|_s^h\\
&-\frac{a''/b''-w''}{\sqrt{1+w''^2}}\ln[2\frac{1-w''X'+\sqrt{(1+w''^2)(1+X'^2)}}{X'+w''}]|_{s'}^{h'}\}
\end{aligned}$$

with $w'=c'/d'$, $w''=c''/d''$

REFERENCES

[1] D. Gabor, "A new microscope principle", *Nature*, **161**, 777, 1948.

[2] P. Hariharan, Optical Holograpy --- Principle, Techniques, and Applications, Cambridge University Press, Cambridge, 2nd ed, 1996.

[3] P. F. Checcacci, V. Russo, and A. Scheggi, "Holographic antennas", *IEEE Trans., Antennas Propagat.*, vol. AP-18, no. 6, 811-813, 1970.

[4] P. F. Checcacci, G. Pati, and V. Russo, "A holographic VHF antenna", *IEEE Trans., Antennas Propagat.*, vol. AP-19, 278-279, 1971.

[5] K. Iizuka, M. Mizusawa, S. Urasaki, and H. Ushigome, "Volume-type holographic antenna", *IEEE Trans., Antennas Propagat.*, vol. AP-23, 807-810, 1975.

[6] A. E. Fathy, et al, "Silicon-based reconfigurable antennas, concept, analysis, implementation, and feacibility", *IEEE Trans., Microwave Theory Tech.*, vol. MTT-51, 1650-1661, 2003.

[7] M. ElSherbiny, A. E. Fathy, A. Rosen, G. Ayers, and S. M. Perlow, "Holographic antenna concept, analysis, and parameters", *IEEE Trans., Antennas Propagat.*, vol. AP-52, 830-839, 2004.

[8] K. Iizuka and L. G. Gregoris, "Application of microwave holography in the study of the field from a radiation source ", *Appl. Phys. Lett.*, vol. 17, 509-512, 1970.

[9] N. H. Farhat and W. R. Guard, "Millimeter wave holographic imaging of concealed weapon", *Proc. IEEE*, vol. 59, 1383-1384, 1970.

[10] J. C. Bennett, A. P. Anderson, P. A. Mclnnes, and A. J. T. Whitaker, "Microwave holographic methodology of large reflector antennas", *IEEE Trans., Antennas Propagat.*, vol. AP-24, 295-303, 1976.

[11] W. H. Lee, "Computer-generated holograms: Techniques and applications", in Progress in Optics, E. Wolf, editor, vol. 16, 121-232. North-Holland Publishing Company, Amsterdam, 1978.

[12] J. Shaker, Thick volume hologram for application in microwave frequency band, *Electronics Letters*, vol. 39, 1701-1702, 2003.

[13] A. H. Sihvola, Electromagnetic mixing formulas and applications, *IEE Electromagnetic Wave Series*, vol. 47, London, 1999.

[14] E. Yablonovitch, "Photonic band-gap structures", *J. Opt. Soc. Am., B*, vol. 10, 283-295, 1993.

[15] D. R. Smith, W. J. Padilla, D. C. Vier, S. C. Nemat-nasser, and S. Schulz, "Composite medium with simultaneously negative permeability and permittivity", *Phy. Rew. Lett.*, vol. 84, 4184-4187, 2000.

[16] W. E. Kock, "Metallic delay lens", *Bell System tech. J.*, vol. 27, 58-82, 1948.

[17] M. M. Z. Kharadly and W. Jackson, "The properties of artificial dielectrics comprising arrays of conducting elements", *IEE Proc.*, paper 1472R, 1953.

[18] J. Brown and W. Jackson, "The properties of artificial dielectrics at centimeter wavelengths", *IEE Proc.*, paper 1699R, Jan. 1955.

[19] J. Brown and W. Jackson, "The relative permittivity of tetragonal arrays of perfectly conducting thin disks", *IEE Proc.*, paper 1702R, Jan. 1955.

[20] R.E. Collin, Field theory of guided waves, McGraw-Hill Inc., New York, 1960.

[21] J. W. Goodman, Introduction to Fourier Optics, McGraw-Hill, New York, 1996.

[22] R. J. Mittra, C. H. Chan, and T. Cwik, "Techniques for analyzing frequency selective surface – A review", *Proc. IEEE*, vol. 76, 1593-1615, 1988.

[23] J. C. Vardaxoglou, Frequency Selective Surfaces, analysis and design, Research Studies Press Ltd., Taunton, 1997

[24] B. A. Munk, Frequency selective surfaces, theory and design, John Wiley & Sons, Inc., New York, 2000.

[25] R. E. Munson, H. Haddad, and J. Hanlen, "Microstrip reflectarray antenna for satellite communication and RCS enhancement or reduction ", U.S. patent 4684952, Aug. 1987.

[26] J. Huang, "Microstrip reflectarray", in *IEEE Int. Symp. Antennas Propagat,*. 612-615, Ontario, Canada, June, 1991.

[27] D. M. Pozar, S. D. Targonski, and H. D. Syrigos, "Design of millimeter wave microstrip reflectarrays", *IEEE Trans., Antennas Propagat.*, vol. AP-45, 287-296, 1997.

[28] S. Fan, P. R. Villeneuve, and J. D. Joannopoulos, "Large omnidirectional band gaps in metallodielectric photonic crystals", *Phys. Rev. B.*, vol. 54, 11245-11251, 1996.

[29] H. Y. D. Yang, "Theory of antenna radiation from photonic band-gap materials", *Electromagnetics*, vol. 19, 255-276, 1999.

[30] M.P. Kesler, J.G. Maloney, B.L. Shirley, and G.S. Smith, "Antenna design with the use of photonic band-gap materials as all-dielectric planar reflectors", *Microwave Opt. Tech. Lett.,* vol. 11, 169-174, 1996.

[31] D.F. Sievenpiper, L.J. Chang, R.F.J. Broas, N.G. Alexopolous, and E. Yablonovitch, "High-impedance electromagnetic surfaces with a forbidden frequency band", *IEEE Trans., Microwave Theory Tech.*, vol. MTT-47, 2059-2074, 1999.

[32] R. Coccioli, F.R. Yang, K.P. Ma, and T. Itoh, "Aperture-coupled patch antenna on UC-PBG substrate", *IEEE Trans., Microwave Theory Tech.*, vol. MTT-47, 2123-22130, 1999.

[33] A. A. Oliner, "Periodic structures and photonic-band-gap terminology: historical perspectives", *Proc. 29th European Microwave Conf.*, Munich, 1999.

[34] A. Hessel, "General characteristics of traveling wave antennas", Ch19 in Antenna theory, vol.2, edited by R.E. Collin and F. J. Zucker, McGraw-Hill, New York, 1969.

[35] R. E. Collin and W. H. Eggimann, "Dynamic interaction fields in a two-dimension lattice", *IRE Trans. Microwave Theory Tech.*, vol. MTT-9, pp.110-115, 1961.

[36] A. Papoulis, The Fourier Integral and its Applications, McGraw-Hill, New York, 1962.

[37] W. H. Eggimann, "Higher-order evaluation of electromagnetic diffraction by circular disks", *IRE Trans. Microwave Theory Tech.*, vol. MTT-9, pp.408-418, 1961.

[38] Wenhao Zhu, Derek A. McNamara, and Jafar Shaker, "Beam switching and scattering analysis for a microwave hologram modeled by disk lattices with transversely modulated sizes", *Microwave and Optical Technology Letters*, vol. 43, No.5, 390-394, 2004.

[39] H. Kogelnik, "Coupled wave theory for thick hologram grating", *Bell Syst. Tech. J.*, vol. 48, pp.2909-2947, 1969.

[40] T. K. Gaylord and M. G. Moharam, "Analysis and applications of optical diffraction by gratings", *Proc. IEEE*, vol. 73, pp.894-937, 1985.

[41] M. G. Moharam and T. K. Gaylord, "Rigorous coupled-wave analysis of grating diffraction – E mode polarization and losses", *J. Opt. Soc. Am.*, vol. 73, pp.451-455, 1983.

[42] R. Magnusson and T. K. Gaylord, "Diffraction regimes of transmission gratings", *J. Opt. Soc. Am.*, vol. 68, pp.809-814, 1978.

[43] G. P. Nordin, R. V. Johnson, and A. R. Tanguay, Jr., "Diffraction properties of stratified volume holographic optical elements", *J. Opt. Soc. Am. A*, vol. 9, pp.2206-2217, 1992.

[44] H. A. Bethe, "Theory of diffraction by small holes", *Phys. Rev.*, vol. 66, pp.163-182, 1944.

[45] E. Arvas and R. F. Harrington, "Computation of the magnetic polarizability of conducting disks and the electric polarizability of apertures", *IEEE Trans., Antennas Propagat.*, vol. AP-31, pp.719-724, 1983.

[46] E. E. Okon and R. F. Harrington, "The polarizabilities of electrically small apertures of arbitrary shape", *IEEE Trans., Electromagn. Compat..*, vol. EMC-23, pp.359-366, 1981.

[47] F. DeMeulenaere and J. Van Bladel, "Polarizability of some small apertures", *IEEE Trans., Antennas Propagat.*, vol. AP-25, pp.198-205, 1977.

[48] R. F. Harrington, Field computation by moment methods, Macmillan, New York, 1968.

[49] R. Mittra, *edited*, Computer techniques for electromagnetics, Pergamon Press, New York, 1973.

[50] S. K. Case, "Microwave theory for multiply exposed thick holographic gratings", *J. Opt. Soc. Am.*, vol. 65, pp.724-729, 1975.

[51] R. Alferness and S. K. Case, "Coupling in doubly exposed holographic gratings", *J. Opt. Soc. Am.*, vol. 65, pp.730-739, 1975.

[52] Wenhao Zhu, Derek A. McNamara, and Jafar Shaker, "Analysis of artificial multiplexed microwave holograms for beam splitting", *2005 IEEE International Symposium On Antennas & Propagation*. Washington, D.C., USA, July 3-8, 2005.

[53] R. E. Collin, "Electromagnetic fields", Ch1 in Antenna theory, vol.1, edited by R.E. Collin and F. J. Zucker, McGraw-Hill, New York, 1969.

[54] P.F. Goldsmith, "Quasi-Optical Techniques", Proc. IEEE, vol. 80, pp1729-1747, 1992.

[55] D. K. Ghodgaonkar, V. V. Varadan, and V. K. Varadan, "Free-space measurement of complex permittivity and complex permeability of magnetic materials at microwave frequencies", *IEEE Trans., Instrumen. Meas.*, vol. 39, 387-394, 1990.

[56] J. L. Le Bras, M. Le Goff, B. Deschamps, A. Peden, D. Bourreau, and S. Toutain, "Quasi-optical circuit measurement method in W-band", *Proc. ESA Workshop Millimeter Wave Tech. and applications*, Espoo, Finland, pp453-457, May, 1998.

[57] M. Le Goff, J. L. Le Bras, B. Deschamps, D. Rozuel, D. Bourreau, and , A. Peden, "Ka band Quasi-optical test bench using focusing horns", *Proc. 29th Europ. Microwave Conf. (EuMC)*, Munich, Germany, vol. 2, pp240-243, October, 1999.

[58] N. Cagnon, "Design and study of a free-space quasi-optical test bed", M.S. thesis, University of Ottawa, 2002.

[59] H. F. Contopanagos, C. A. Kyriazidou, W. M. Merrill, and N. G. Alexopoulos, "Effective response functions for photonic bandgap materials", *J. Opt. Soc. Am. A*, vol.16, 1682-1699, 1999.

[60] C. A. Kyriazidou, H. F. Contopanagos, W. M. Merrill, and N. G. Alexopoulos, "Artificial versus natural crystals: effective wave impedance of printed photonic bandgap materials", *IEEE Trans. Antennas and Propagation*, vol. AP-48, 95-106, 2000.

[61] H. F. Contopanagos, L. Zhang, and N. G. Alexopoulos, "Thin frequency-selective lattices integrated in novel compact MIC, MMIC, and PCA architectures", IEEE Trans. Microwave Theory and Tech., vol. MTT-46, 1936-1948, 1998.

[62] I.S. Gradshteyn and I.M. Ryzhik, Table of integrals, series, and products, Academic Press, New York, 1980.